# Using the $\phi$-meson to probe the medium created in Au+Au collisions at RHIC

Sarah-Louise Blyth

Thesis Presented for the Degree of

DOCTOR OF PHILOSOPHY

in the Department of Physics
Faculty of Science
UNIVERSITY OF CAPE TOWN

· February 2007 ·

## Abstract

This thesis presents measurements of $\phi$-meson production and elliptic flow, $v_2$, with the aim of probing the characteristics of the medium created in ultra-relativistic nucleus-nucleus collisions. Using the decay channel $\phi \rightarrow K^+K^-$, high statistics measurements have been made for $\phi$-meson production at mid-rapidity in Au+Au collisions at $\sqrt{s_{NN}} = 200$ GeV using the STAR detector at RHIC. The $\phi$-meson invariant yields both integrated, and as a function of $p_T$, are presented for a wide range of collision centralities. The transverse momentum distributions exhibit an evolution in shape with decreasing collision centrality from exponential-like to power-law-like, indicating a variation in the relative contributions from competing particle production mechanisms to $\phi$ production as a function of collision centrality.

Measurements of the nuclear modification factor, $R_{CP}$, for 0-5% central relative to 40-60% and 60-80% central collisions show that binary-scaled $\phi$-meson production is suppressed in central compared to more peripheral collisions. The baryon-meson scaling of $R_{CP}$ observed for other identified particles is also observed for the $\phi$-meson through its similarity to the $K^0_S$ $R_{CP}$ for 0-5%/40-60% ratio. The scaling appears to break down in the 0-5%/60-80% case.

The centrality dependence of the $N(\Omega)/N(\phi)$ ratios are also presented. The central ratio is consistent up to $p_T \lesssim 4$ GeV/$c$ with expectations from a model in which multistrange hadrons are produced predominantly by recombination of thermal $s$ quarks.

In addition, the $\phi$-meson elliptic flow, $v_2(p_T)$, has been measured in Au+Au collisions at $\sqrt{s_{NN}} = 62.4$ GeV and 200 GeV and is found to be similar for the two collision energies. The significant $v_2$ for the $\phi$-meson, comparable to that of other particles, indicates significant rescattering of the medium constituents. In minimum bias collisions at 200 GeV, for $p_T < 2$ GeV/$c$, the $\phi$-meson $v_2$ is consistent with a mass ordering expected from hydrodynamics while for $p_T > 2$ GeV/$c$ it is consistent with meson-scaling. This is strong evidence for partonic collectivity of the medium created in the collisions. First measurements of the centrality dependence of the $\phi$-meson integrated elliptic flow scaled by the eccentricity of the nuclear overlap region, $\langle v_2 \rangle / \epsilon_{part}$, show an increasing trend with centrality and may indicate greater collectivity of the medium created in central compared to peripheral Au+Au collisions.

Parts of the work presented in this thesis have also been presented in:

## Papers and Proceedings

*Centrality dependence of the $N(\Omega)/N(\phi)$ ratios and $\phi$ $v_2$ - a test of thermalization in Au+Au collisions at RHIC*
Sarah-Louise Blyth for the STAR collaboration,
(Proceedings of Quark Matter 2006 Conference, 13-20 November 2006, Shanghai, China (to be published))

*$\phi$-meson Production in Heavy-Ion Collisions at RHIC.*
Sarah-Louise Blyth for the STAR Collaboration,
J. Phys. G: Nucl. Part. Phys. 32 (2006) S461-S464.
(Proceedings of International Conference on Strangeness in Quark Matter (SQM2006), Los Angeles, California, 26-31 Mar 2006.)

*Partonic flow and $\phi$-meson production in Au+Au collisions at $\sqrt{s_{NN}} = 200$ GeV*
STAR collaboration, (B.I. Abelev *et al.*)
Currently in preparation.

## Talks

*Centrality dependence of the $\Omega/\phi$ ratios and $\phi$ $v_2$ - a test of thermalization in Au+Au collisions at RHIC*
Sarah-Louise Blyth for the STAR Collaboration
Talk presented at Quark Matter 2006 Conference, 13-20 November 2006, Shanghai, China.

*$\phi$-meson production in heavy-ion collisions at RHIC*
Sarah-Louise Blyth for the STAR Collaboration
Talk presented at Strangeness in Quark Matter Conference, March 2006, Los Angeles, California, USA.

*Elliptic flow of the $\phi$-meson in Au+Au collisions at 62.4 GeV*
Sarah-Louise Blyth
Invited talk at the School of Collective Dynamics in High-Energy Collisions, July 2005, Berkeley, California, USA.

*Ellliptic flow of the $\phi$-meson in Au+Au collisions at 62.4 GeV*
Sarah-Louise Blyth for the STAR Collaboration
Talk presented at April APS Meeting (2005), Tampa, Florida, USA.

# Contents

# Chapter 1

# Introduction

The Standard Model of particle physics is our means to describe the fundamental particles of nature, namely the three generations of quarks and leptons, and their interactions: the strong interaction, weak interaction, and the electromagnetic interaction. (Gravity has not been incorporated into the Standard Model.) Each of the interactions couple to different properties of the particles and are mediated by different mediating bosons, for example, the photon mediates the electromagnetic interaction while gluons are the mediators of the strong force. The traditional grouping of the particles of the standard model is presented in Fig. 1.1. (I, II, and III represent the three generations of quarks and leptons.)

## 1.1 The strong force, QCD, and the quark-gluon plasma

On the sub-atomic scale (i.e. inside the nucleus), the strong force by far overwhelms the effects of the other interactions. It couples to the colour charge of the quarks and is the force which keeps the quarks inside the nucleons and binds the nucleons together inside the nuclei of atoms. The strong interaction displays two interesting features: confinement and asymptotic freedom.

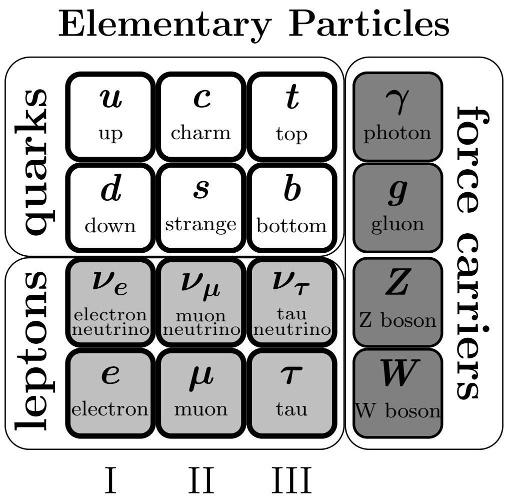


**Figure 1.1**: The fundamental particles of the Standard Model are presented: quarks, gluons and the force mediating bosons. I, II, and III represent the three generations of quarks and leptons.

At large distances or small momentum transfers, $Q^2$, the coupling strength of the strong interaction, $\alpha_s$, is very large and increases as the distance between two quarks is increased. This property is called confinement and is the reason that quarks are never found alone but are instead always bound together in groups of three called baryons (e.g. the proton and neutron) or as quark-antiquark pairs called mesons. Asymptotic freedom describes the feature that the coupling between quarks becomes small when the distances between the quarks are small i.e. when the momentum transfer $Q^2$ is large. In other words, at asymptotically high energies, $\alpha_s$ tends to zero and the quarks behave like free particles.

In the early 1970s, Fritzsch, Gell-Mann and Leutwyler proposed that the strong interaction could be modeled using a Yang-Mills gauge quantum field theory with coloured quarks and an octet of coloured gluons [1]. The theory was non-abelian meaning that the force-mediating gluons also carried colour charge and could undergo self-interactions, unlike in quantum electrodynamics (QED), where the photon carries no electric charge. Shortly afterwards, Gross, Wilczek and Politzer [2–4] discovered that non-abelian gauge theories (like the one proposed by Fritzsch et al.) have the feature of asymptotic freedom. (Gross, Wilczek and Politzer later won the 2004 Nobel prize in Physics for this discovery.) Therefore the theory of Fritzsch et al. called Quantum Chromodynamics (QCD) (*chromo-* referring to the *colour* charges of the gluons and quarks) with its properties of asymptotic freedom and confinement possessed the necessary features to describe the strong force and is accepted today as the theory of the strong force.

One of the important consequences of asymptotic freedom in terms of calculating quantities in QCD, is the fact that $\alpha_s$ becomes small at high energies and $Q^2$, allowing the application of perturbation theory, pQCD, as a means to calculate physical observables. In order to calculate various quantities such as cross-sections, decay rates etc., divergences are avoided by applying the procedure of renormalization whereby parameters in the calculation are fixed at a given scale. $\alpha_s$ is also renormalized and becomes the effective running coupling constant $\alpha_s(Q^2)$. In this way, the calculations are valid above a certain momentum transfer $Q^2$ or energy set by the chosen scale. Perturbative QCD has been very successful in predicting and describing various processes observed in different experiments as is illustrated in Fig. 1.2 from [5] where the value of $\alpha_s(Q)$ is extracted from experimental results and compared to pQCD expectations. The running of $\alpha_s(Q)$ in line with pQCD expectations can clearly be seen.

However, at low $Q^2$ when $\alpha_s(Q^2)$ becomes large, perturbation theory breaks down, and other non-perturbative numerical methods are required to perform calculations in QCD. One of the primary focus areas in nuclear theory is the use of lattice gauge techniques to calculate QCD quantities at equilibrium numerically, in the non-perturbative regime. Lattice QCD (lQCD) calculations involve the discretization of the continuous integral describing the QCD partition function. The discretization is performed on a four dimensional space-time lattice with size $N_\sigma^3 \times N_\tau$ and lattice spacing $a$. As the quark masses and the lattice spacing are reduced, the complexity of the calculations increases, requiring large computing resources.

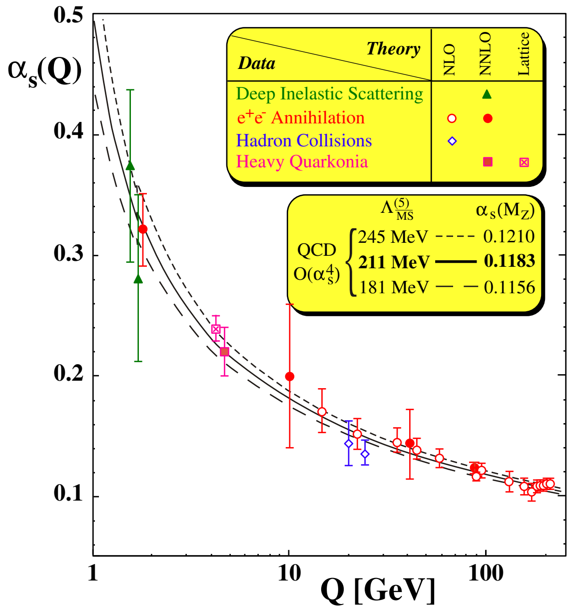


**Figure 1.2**: Summary of meaurements of $\alpha_s(Q)$ extracted from experimental results compared to QCD predictions (curves) from [5].

### 1.1.1 The QCD phase transition

It was conjectured by Collins and Perry in 1975, soon after the discovery of asymptotic freedom in non-abelian gauge theories, that at very high densities, nuclear matter would exist as a "quark soup" instead of a dense hadronic system [6]. QCD predicts a phase transition, above some critical temperature $T_c$, from ordinary hadronic matter to a phase of deconfined quarks and gluons called the quark-gluon plasma (QGP). The system of free quarks and gluons at high temperatures is also expected to have the QCD symmetry of colour, chiral symmetry, restored. With the restoration of chiral symmetry, the (light) quarks are expected to regain their small current quark masses and appear as nearly massless particles compared to their larger constituent quark masses when confined inside hadrons.

Striking evidence for the QCD phase transition at a critical temperature of $T_c$ ~170 MeV and energy density of $\epsilon$ ~1 GeV/fm$^3$ is provided by lattice gauge calculations. Using lQCD techniques, thermodynamic variables such as the energy density ($\epsilon$) and pressure ($p$) have been calculated as a func-

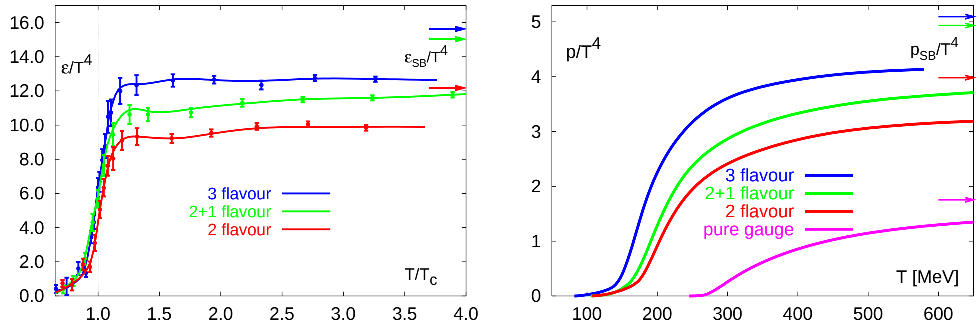


**Figure 1.3**: **Left panel:** Lattice QCD calculations for energy density, $\epsilon$, as a function of temperature. **Right panel:** Lattice QCD calculations for pressure, $p$, with number of quark flavours $n_f = 0$, 2, 3 and 2 light plus 1 heavier (strange) quark. Also shown in both panels are the Stefan-Boltzmann ideal gas limits for each case. Both plots are taken from [7].

tion of temperature as presented in Fig. 1.3 [7]. At a critical temperature of $T_c$ ∼170 MeV (at zero chemical potential $\mu_B$), there is a sharp increase in the energy density ($\epsilon$) and pressure ($p$) of the system, indicating a rather sudden increase in the number of degrees of freedom of the system i.e. the deconfinement transition from hadrons to quarks and gluons. The dependence on the number of quark flavours is also shown in the plots. Also calculated for each case is the Stefan-Boltzmann ideal gas limit which in all cases is above the values calculated on the lattice. At asymptotically high temperatures, it is expected that the energy density and pressure approach the Stefan-Boltzmann values for a weakly interacting ideal gas, however, even at temperatures of more than four times $T_c$, the curves are significantly below the Stefan-Boltzmann limit which implies that the particles present above $T_c$ still interact with each other. The exact order of the phase transition is not known although more recent calculations indicate that at $\mu_B = 0$, it is likely to be a smooth cross-over.

Figure 1.4 shows the QCD schematic phase diagram which aims to map out the phases of QCD matter as a function of temperature, $T$, and baryon chemical potential, $\mu_B$. Currently, the general asymptotic properties of QCD can be mapped and these are shown by the labeled regions in the diagram. For example, at very high $T$ and low $\mu_B$, a state of weakly interacting, deconfined quarks and gluons (QGP) (which are the expected conditions of the early universe) is expected to exist, while at low $T$ and $\mu_B$, the quarks and gluons are known to be confined inside colour-neutral hadrons (which is what we observe in the universe today). QCD calculations at low $T$ and high $\mu_B$ (which are the conditions expected in the centers of neutron stars for example) suggest that the quarks form a colour super-conducting 2SC phase [8].

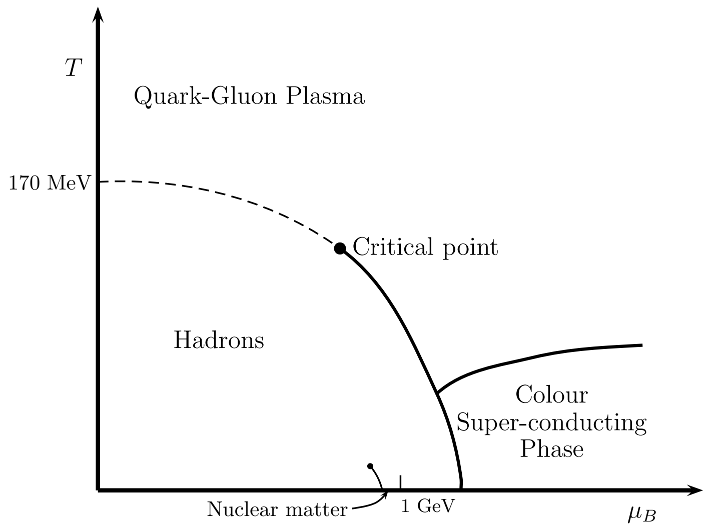


**Figure 1.4**: Phase diagram of nuclear matter in terms of temperature $T$ and baryon chemical potential $\mu_B$.

However, the exact position on the phase diagram of the phase transition line between the different phases in the different regions of $T$ and $\mu_B$, and the exact properties of the matter in each of the phases, are not yet precisely known.

The order of the phase transition at high $\mu_B$ and low $T$ is expected to be of first order, while at the other extreme of zero $\mu_B$ and high $T$, calculations using non-vanishing masses of the $u$ and $d$ quarks predict that the transition is a smooth crossover [8]. Therefore, the line which connects the phase transition at the two axes, must have a discontinuity at some point in between (called the critical endpoint). Lattice QCD calculations predict a temperature for the transition, at $\mu_B = 0$, between 150-200 MeV [7, 9]. Recently lQCD calculations at non-zero chemical potential have attempted to pin down the position of the critical point, and first results infer it to be somewhere in the range $T_E \sim 160$ MeV and $\mu_{BE} \sim 725$ MeV [9]. However these results were based on using unphysically large values for the quark masses and so further refinement of the calculations is still necessary.

In physics, the scientific method requires that theory is tested for consistency with nature. To this end, experiment is necessary in order to gain further insights into the predicted phase transition of QCD.

## 1.2 The Search for the QGP: Heavy-Ion Collisions

Colliding heavy-ions (heavy nuclei) at relativistic energies as a means to create a system of hot and dense nuclear matter in the laboratory, was first suggested in the early 1970s [10]. Relativistic heavy-ion collisions can be used to excite the vacuum since the almost simultaneous collisions of the nucleons in the two nuclei releases a large amount of energy over a very short time interval, within a volume approximately the size of the nucleus, which may create energy densities above that required for a phase transition ($\sim$1 GeV/fm$^3$).

Heavy-ion experiments involving nucleus-nucleus collisions started in the early 1970s at the Bevalac at Lawrence Berkeley National Laboratoy (LBNL) to study the nuclear matter equation of state at densities several times higher than the nuclear ground state density. Various species of nuclei were used at center of mass energies up to $\sqrt{s_{NN}} = 2.32$ GeV at the Bevalac. With the discovery of QCD, and the predicted existence, at high temperatures, of a deconfined state of matter consisting of free quarks and gluons, experimental facilities were built to run at higher center of mass energies. A large number of nucleus-nucleus collision experiments have been run at various facilities. For example, the Alternating Gradient Synchrotron (AGS) at Brookhaven National Laboratory (BNL) and the Super Proton Synchrotron (SPS) at CERN have run fixed target heavy-ion collision experiments at top center of mass energies of $\sqrt{s_{NN}} = 4.86$ GeV and $\sqrt{s_{NN}} = 17.3$ GeV respectively.

So far, the highest energy nucleus-nucleus collisions have been run at the Relativistic Heavy-Ion Collider (RHIC) at BNL which is also the first machine to collide beams of heavy-ions. RHIC has collided Au+Au and Cu+Cu beams at $\sqrt{s_{NN}} = 22.4$, 62.4, 200 GeV and large amounts of data have been analysed by the four RHIC experiments (BRAHMS, PHENIX, PHOBOS and STAR) at these high energies. (Since the results presented in this thesis are based on measurements using the STAR experimental apparatus, further details on RHIC and the four experiments, and STAR in particular, are discussed in Chapter 2).

Future plans for the field include the highest energy nucleus-nucleus collisions yet, which are planned to be run at the Large Hadron Collider (LHC) at CERN with first collisions of Pb+Pb at $\sqrt{s_{NN}} = 5.5$ TeV targeted for 2008.

### 1.2.1 The evolution of a heavy-ion collision

An illustration of the evolution of a heavy-ion collision is shown in Fig. 1.5. The nuclei traveling at relativistic velocities appear Lorentz-contracted in the lab-frame. After the collision of the nuclei at least two possible situations may occur. If the energy density created in the collision does not reach the critical value necessary for quark-gluon plasma formation, then the system will be composed of a gas of hadrons (as indicated in the left-hand side of Fig. 1.5.

However, the other possibility is that the energy density created may be large enough to create a fireball of deconfined quarks and gluons (shown on the right-hand side of the diagram). If the system is long-lived enough to allow thermalization and chemical equilibration through interactions of the quarks and gluons, then the medium may be classified as a phase of matter with an equation of state: the quark-gluon plasma ($\tau = \tau_0$). The subsequent expansion of the system may then be described by relativistic hydrodynamics. As the system expands and cools to the critical temperature $T_c$, hadronization takes place and the quarks and gluons become confined. Due to the finite formation time for hadrons, the system is likely to evolve through a mixed phase where free quarks and gluons exist simultaneously with hadrons. Once all the quarks and gluons are confined inside hadrons, the system can be called a gas of hadrons (the same as the initial system created in the left-hand side of Fig.1.5). As the system of hadrons continues to expand outwards, at some later time inelastic scatterings between the hadrons cease, and *chemical freeze-out* occurs defined by a temperature $T_{ch}$. *Thermal* or *kinetic freeze-out* occurs when the system becomes so dilute that the hadrons are no longer able to interact elastically with each other and become free-streaming (at $T_{fo}$, $\tau = \tau_f$). This is the stage at which particles are measured in experimental detectors (denoted by the arrows in the diagram).

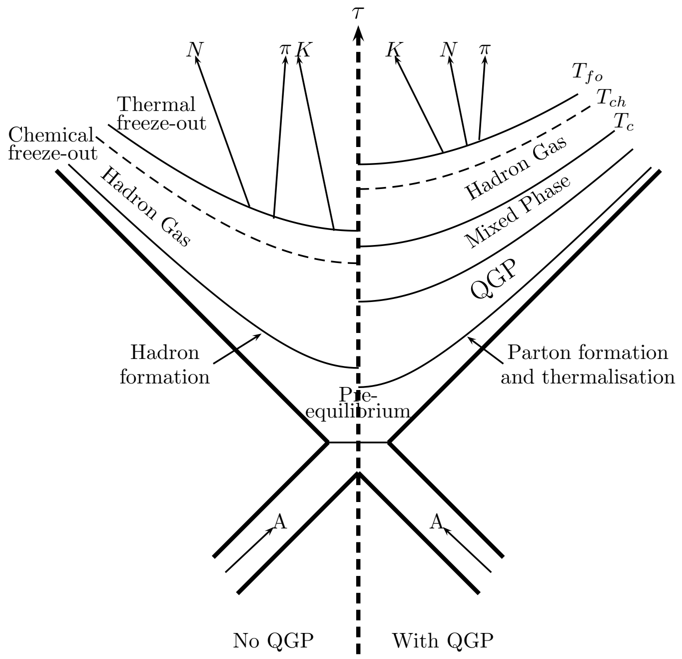


**Figure 1.5**: Two scenarios for the evolution of the system created in a relativistic nucleus-nucleus collision. The left-hand side shows the evolution for the case of no QGP being created, while the right-hand side shows the expected evolution of the system including QGP formation. Lines of constant temperature indicate hadronization ($T_c$), chemical freeze-out ($T_{ch}$) and kinetic freeze-out ($T_{fo}$).

### 1.2.2 Geometry of heavy-ion collisions

In a heavy-ion collision, a probability distribution governs the degree of overlap of the two colliding nuclei from head-on (most central) down to collisions in which the nuclei barely graze each other in passing (ultra-peripheral). The degree of overlap or *centrality* of a collision is determined by the impact parameter $b$ which is defined as the perpendicular distance from the centre of the target nucleus to the line of motion through the centre of the projectile nucleus (illustrated in Fig. 1.6). Therefore $b = 0$ describes the most central of collisions, and $b = 2r$ (where $r$ is the radius of the nucleus in a simple hard shell description) describes very peripheral collisions.

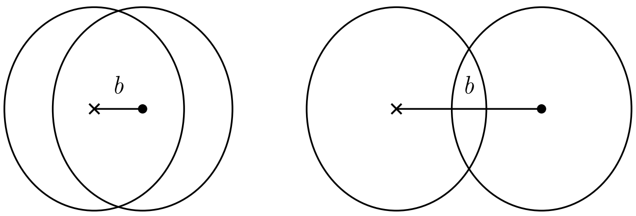


(a) (b)

**Figure 1.6**: Illustration of impact parameter definition for (a) a mid-central and (b) a peripheral collision of two nuclei. The directions of motion of the target and projectile nuclei are into ($\times$) and out of ($\bullet$) the page respectively.

Within the multiple-scattering Glauber model formalism [11–13], the nuclear overlap function for nuclei $A$ and $B$ and impact parameter $b$ is given by

$$T_{AB}(\overrightarrow{b}) = \int d^2\overrightarrow{s}T_A(\overrightarrow{s})T_B(\overrightarrow{b} - \overrightarrow{s}). \qquad (1.1)$$

where $T_A$ and $T_B$ are the nuclear thickness functions for nuclei A and B respectively and are given by:

$$T_{A(B)}(\overrightarrow{s}) = \int dz\rho_{A(B)}(z, \overrightarrow{s}). \qquad (1.2)$$

Here $z$ is the beam direction and $\rho_{A(B)}$ is the nuclear density profile which is usually described by a Woods-Saxon distribution. The inclusive, inelastic cross-section, $\sigma_{AB}$, for the collision of nucleus A with nucleus B can then be related to the overlap function as:

$$\sigma_{AB} = \int d\overrightarrow{b} \left[1 - e^{-\sigma_{NN} T_{AB}(\overrightarrow{b})}\right], \tag{1.3}$$

where $\sigma_{NN}$ is the nucleon-nucleon cross-section (assumed to be given by the p+p cross-section).

The collision centrality in experiments is determined by relating the produced charged particle multiplicity (within an interval of pseudorapidity) to $\sigma_{AB}$. A more central collision (with small impact parameter $b$) will correspond to a large overlap area of the two colliding nuclei and a larger cross-section for interactions. Therefore, events with higher produced particle multiplicities correspond to more central collisions.

In experiment, the total charged particle multiplicity distribution is measured, corrected for trigger inefficiencies, and is then divided into intervals or bins according to the percentage of the total cross-section. For example, Fig. 1.7 shows the raw event charged particle multiplicities for 80% of the total hadronic cross-section, binned into 9 classes from Au+Au collisions at $\sqrt{s_{NN}}$ = 200 GeV measured by STAR. The centrality classes 9-1 refer to 0-5%, 5-10%, 10-20%, 20-30%, 30-40%, 40-50%, 50-60%, 60-70%, 70-80% of the total cross-section respectively.

When investigating experimental observables as a function of the collision centrality, a variety of variables are used to denote the centrality. For example, the variable $dN_{ch}/d\eta$, the number of charged hadrons per unit pseudorapidity, is often used due to its direct correspondence to $T_{AB}$. Another variable which is commonly used and which has a close connection to $T_{AB}$ is the number of participants, $N_{part}$, defined as the number of nucleons (protons and neutrons) contained within the overlap region of the two nuclei. For symmetric nucleus-nucleus collisions (i.e A = B):

$$N_{part}(b) = 2A \int d\overrightarrow{s} T_A(\overrightarrow{s} - \overrightarrow{b}) \left(1 - (1 - \sigma_{NN} T_A(\overrightarrow{b}))^A\right). \tag{1.4}$$

A related quantity, used to describe the scaling of hard, perturbative pro-

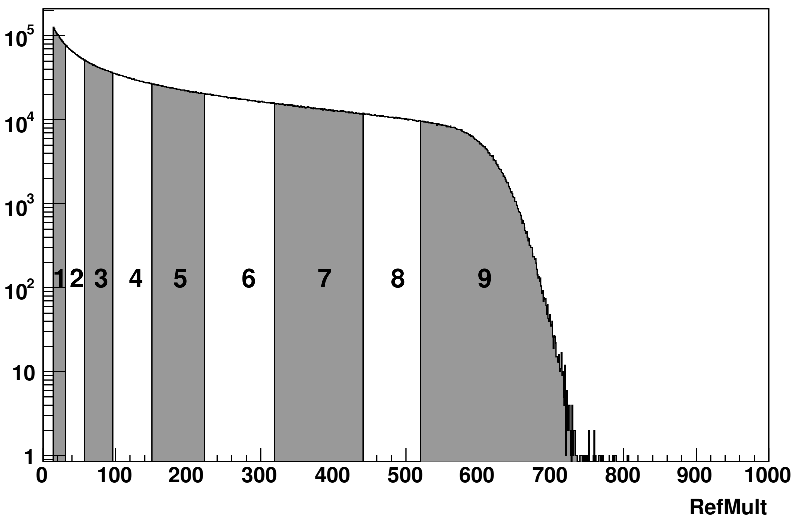


**Figure 1.7**: Raw reference multiplicity (RefMult) of charged particles as measured by the STAR experiment for Au+Au collisions at $\sqrt{s_{NN}} = 200$ GeV. The centrality classes 9-1 refer to 0-5%, 5-10%, 10-20%, 20-30%, 30-40%, 40-50%, 50-60%, 60-70%, 70-80% of the total cross-section respectively.

cesses, is the number of binary collisions, $N_{bin}$. In nucleus-nucleus collisions at relativistic energies where the collision can be thought of as two nuclei passing through each other, the nucleons in each nucleus have a probability of interacting more than once before traversing the full width of the other nucleus. The number of binary nucleon-nucleon interactions for the colliding nuclei A and B can be calculated as:

$$N_{bin}(b) = \sigma_{NN} \int \rho_A(z', \overrightarrow{s})\rho_B(z'', \overrightarrow{b} - \overrightarrow{s})d\overrightarrow{s}dz'dz'' \qquad (1.5)$$

$$= \sigma_{NN} T_{AB}(\overrightarrow{b}). \qquad (1.6)$$

## 1.3 Experimental observables

Since the hot and dense medium created in nucleus-nucleus collisions is extremely short-lived (~5-10 fm/$c$) and only the final-state freely streaming particles are measured in the detectors of experiments, we are forced to use final-state observables and extrapolate backwards to characterize the properties of the system at early times. Many 'signatures' of QGP formation and associated characteristics of the medium have been proposed (see [14, 15] for an overview), for example proposed signatures of deconfinement include suppression of charmonium production [16] and enhanced production of multi-strange particles [17] whereas modifications of meson masses has been predicted to be a signature of chiral symmetry restoration [18].

The nature of the final-state of relativistic nucleus-nucleus collisions with their large particle multiplicities and variety of species of produced particles leads to a large range of experimental observables which can be used to probe and characterize the properties of the produced system. So-called *penetrating probes* such as high-$p_T$ jets or heavy quarks (i.e. charm and bottom) are produced at early times in the initial high-$Q^2$ nucleon-nucleon scatterings (called binary collisions) ($\tau_{hard} \sim 1/Q \leq$0.01 fm/$c$) when the nuclei collide. Most of the secondary matter which constitutes the medium is formed slightly later ($\tau \sim 1/T_0 \sim$0.2 fm/$c$) and the hard/heavy probes become 'embedded' in the dense medium. The properties of these hard/heavy probes may be modified by medium effects, for example, high-$p_T$ partons (jets) lose energy as they traverse the dense medium, and measurements of the jet observables (after the parton fragments) may provide information on the medium density (i.e. gluon density).

*Bulk observables* which examine the bulk of produced particles and their distributions with respect to variables such as centrality, transverse momentum ($p_T$), angle with respect to the reaction plane of the system, etc. can provide information about different aspects of the system and the stages of its evolution:

- Late stage and time-integrated information such as the temperature at which the system undergoes chemical freeze-out ($T_{ch}$) may be extracted by studying particle yields. Hadron $p_T$ spectra can also provide information about thermal freeze-out and the mean radial flow of the system.

- Insight into the medium density, its constituents and how particle production may be affected by its formation may be gained by studying modifications to particle spectral shapes compared to expectations from elementary p+p collisions at intermediate and high $p_T$. Ratios of different particle species may also provide information on the medium constituents and the mechanisms by which particles are produced in heavy-ion collisions.

- Early stage information such as the initial pressure and energy density as well as the degree of thermalization and collectivity of the produced medium can be investigated by studying early stage observables such as the azimuthal anisotropy of particle distributions with respect to the reaction plane of the collision.

A selection of bulk observables and what information they can provide about the properties of the medium created in ultra-relativistic heavy-ion collisions at RHIC will be discussed in the following sections.

### 1.3.1 Particle yields and transverse momentum distributions

#### Chemical freeze-out

For nucleus-nucleus collisions at the highest energies to date (at RHIC), the yields and transverse momentum spectra for various particle species have been measured. Particle yields can provide information about the system from the time of *chemical freeze-out* when the inelastic collisions cease and the chemical abundances become fixed. Statistical Thermal Models (in a number of variations) [19–21], have been very successful in describing the particle ratios observed at RHIC using only a few model parameters (i.e. chemical freeze-out temperature $T_{ch}$, baryon and strangeness chemical potentitals $\mu_B$ and $\mu_S$ and strangeness suppression factor $\gamma_s$) extracted from fitting to particle yield ratio data. Comparison of statistical model results to data from the STAR experiment is presented in Fig. 1.8 [22].

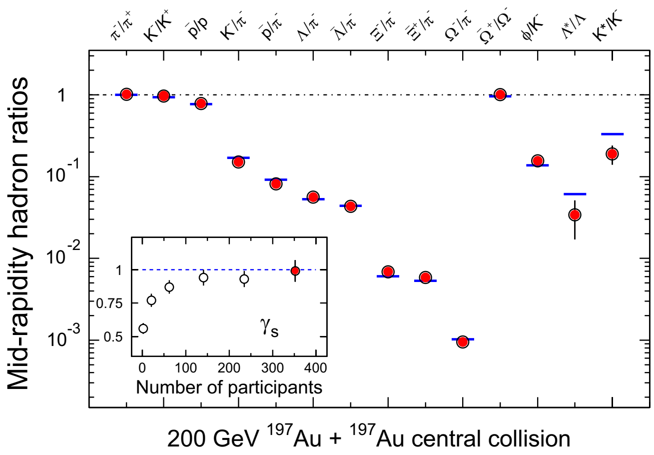


**Figure 1.8**: Ratios of the mid-rapidity $p_T$-integrated yields for different hadron species measured by the STAR experiment for Au+Au collisions at $\sqrt{s_{NN}} = 200$ GeV (circles). The horizontal lines represent statistical model fits to the measured particle yield ratios. The values for the extracted fit parameters are: $T_{ch} = 163 \pm 4$ MeV, $\mu_B = 24 \pm 4$ MeV, $\gamma_s = 0.99 \pm 0.07$ from [23]. The inset shows the extracted variation of $\gamma_s$ as a function of centrality. Plot taken from [22].

The plot shows the integrated $p_T$ particle yield ratios (circle markers) measured by the STAR experiment in Au+Au collisions at $\sqrt{s_{NN}} = 200$ GeV. The horizontal lines show the statistical model fits to the particle ratios [23] using only 3 parameters ($T_{ch} = 163 \pm 4$ MeV, $\mu_B = 24 \pm 4$ MeV, $\gamma_s = 0.99 \pm 0.07$). These values are similar to values obtained using different variations of the statistical model [24, 25] for RHIC data. Shown in the inset in Fig. 1.8 is the evolution of the strangeness suppression factor $\gamma_s$ which is a measure of how far the system is from chemical equilibrium. For the most central collisions, the $\gamma_s$ value obtained from the statistical model fits is $\gamma_s = 0.99 \pm 0.07$ [23] i.e. consistent with unity, providing a strong argument in favour of the system, which is created in central collisions at RHIC, being in chemical equilibrium.

### Thermal freeze-out

Measurements of particle transverse momentum distributions provide information on the properties of the system at *thermal* or *kinetic freeze-out* when all elastic collisions have ceased. Also, 'frozen in' to the spectra is information on the outward expansion of the system integrated over time. The idea of a common collective outward expansion velocity ($\beta_T$) of particles in the system is consistent with the observations that the $\langle p_T \rangle$ of heavier particles is larger than for lighter particles (i.e. for the same outward velocity, more massive particles will have a larger momentum) and that $\langle p_T \rangle$ increases as a function of centrality [22, 26]. Figure 1.9 shows the increase of $\langle p_T \rangle$ for $\pi^{\pm}$, $K^{\pm}$ and $p(\bar{p})$ as a function of centrality as measured by the PHENIX experiment for Au+Au collisions at $\sqrt{s_{NN}} = 200$ GeV [26].

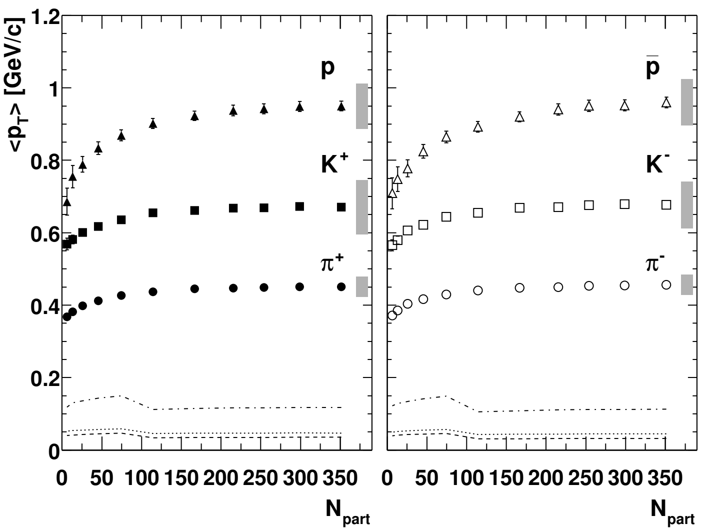


**Figure 1.9**: Mean transverse momentum $\langle p_T \rangle$ as a function of $N_{part}$ for $\pi^{\pm}$, $K^{\pm}$, $p$, and $(\bar{p})$ from Au+Au collisions at $\sqrt{s_{NN}} = 200$ GeV measured by the PHENIX experiment. The shaded bars represent the systematic error and the systematic errors from extrapolation (scaled by a factor of 2 for clarity) are indicated by the dashed-dotted ($p$ and $\bar{p}$), dotted ($K^{\pm}$) and dashed ($\pi^{\pm}$) lines [26].

In order to gain further information and attempt to quantify the transverse expansion of the system, particle spectra, measured by the STAR experiment, have been fitted with a hydrodynamics-inspired parameterization of a thermal expanding source (so-called blast-wave model) [27] with fit parameters including the thermal freeze-out temperature ($T_{fo}$) and the mean collective expansion velocity ($\langle \beta_T \rangle$). Figure 1.10 [22] shows the results from fitting the spectra for $\pi, K, p$ simultaneously, as a function of centrality. The extracted $\langle \beta_T \rangle$ is highest for most central collisions while $T_{fo}$ is lowest. This implies that the system created in central collisions expands faster and cools down to a lower temperature ($T_{fo} \sim 80$ MeV) before thermal freeze-out than systems created in more peripheral collisions ($T_{fo} \sim 140$ MeV).

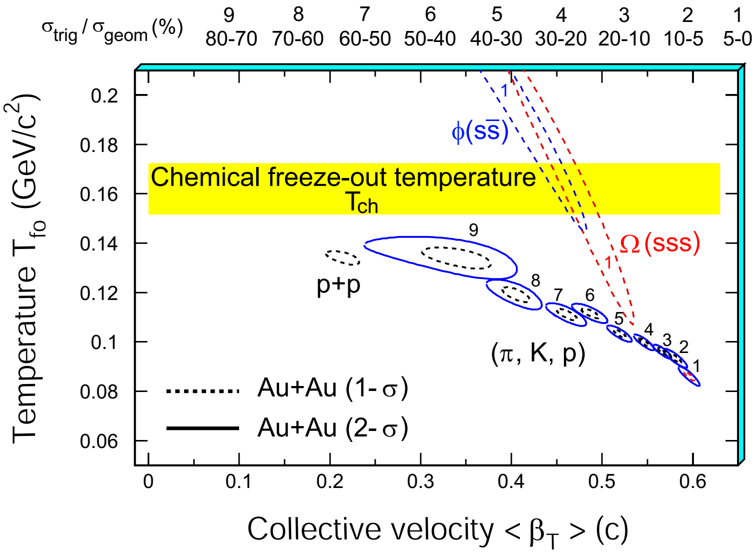


**Figure 1.10**: The $1\sigma$ and $2\sigma$ $\chi^2$ contours for $T_{fo}$ and $\langle\beta_T\rangle$ extracted from thermal and radial flow fits to $\pi, K, p$ data in 9 centrality bins for Au+Au collisions at $\sqrt{s_{NN}} = 200$ GeV and for $\sqrt{s_{NN}} = 200$ GeV p+p collisions. Also shown are fits for the most central data for $\phi$ and $\Omega$. Plot taken from [22].

### 1.3.2 The nuclear modification factor

Studies of hadron spectra in nucleus-nucleus collisions can also shed light on the properties of the dense medium created in the collisions and on particle production mechanisms in different $p_T$ ranges. By comparing particle spectra from central Au+Au collisions to production in p+p collisions, we can study the effects of the medium on particle production. A means to do this comparison is via the nuclear modification factor $R_{AA}$ which, for a given particle, is the ratio of the $p_T$ distribution in Au+Au collisions (for a given centrality) scaled by the number of binary collisions, $N_{bin}$, appropriate for the centrality, divided by the spectrum in p+p collisions:

$$R_{AA}(p_T) = \frac{d^2N^{AA}/dp_T d\eta}{T_{AA} \cdot d^2\sigma^{NN}/dp_T d\eta} \tag{1.7}$$

and $T_{AA} = \langle N_{bin}\rangle/\sigma^{NN}_{inel}$. In addition to comparing to particle production in p+p, comparison can be made of the yields in central nucleus-nucleus collisions to those in peripheral collisions to quantify the differences between the systems created in collisions with different centralities:

$$R_{CP}(p_T) = \frac{d^2N^{AA}/dp_T d\eta|_{central}}{d^2N^{AA}/dp_T d\eta|_{periph}} \times \frac{\langle N_{bin}\rangle|_{periph}}{\langle N_{bin}\rangle|_{central}}. \tag{1.8}$$

**The dense medium**

$R_{AA}(p_T)$ and $R_{CP}(p_T)$ should be equal to unity if particle production in nucleus-nucleus collisions scales with the number of binary collisions. However, for Au+Au collisions at $\sqrt{s_{NN}} = 130$ and 200 GeV, the RHIC experiments report values for the nuclear modification factor below 1 for charged hadrons and identified particles (for an overview of results see [22,26,28,29]), as illustrated using the STAR results shown in Fig. 1.11 [30].

This means that for intermediate to high $p_T$ ($p_T > 2$) GeV/$c$, there is a suppression of particle production in central to mid-central Au+Au collisions compared to p+p collisions and in central Au+Au compared to peripheral Au+Au collisions. This suppression has been attributed to energy loss of high-$p_T$ partons in the dense medium created in central collisions [31,32].

**Particle production**

Another interesting observation has been made regarding the particle-type dependence of $R_{CP}$ in Au+Au collisions: although they both show a suppression, at intermediate $p_T$ between 2-5 GeV/$c$, the mesons and baryons seem to follow different trends from each other as a function of $p_T$ as shown in Fig. 1.12 [33] by the different trends followed by $\Lambda + \bar{\Lambda}$ compared to $K^0_S$

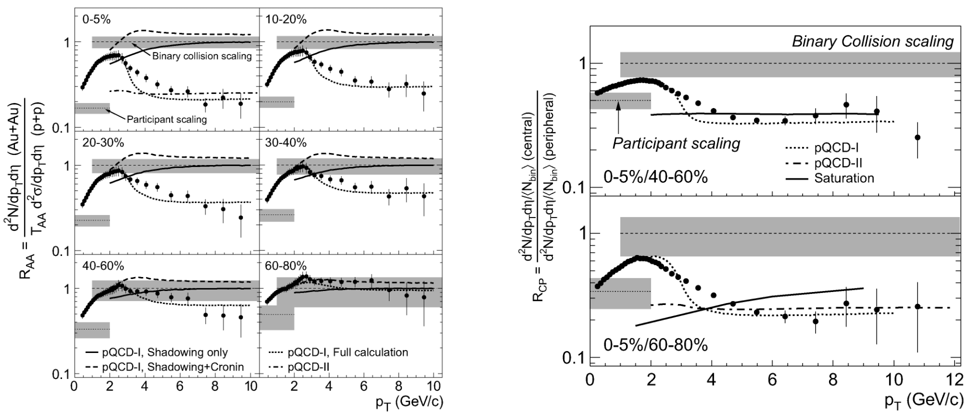


**Figure 1.11**: **Left panel:** $R_{AA}$ and **Right panel:** $R_{CP}$ for charged hadrons for a range of centralities measured by the STAR collaboration for Au+Au collisions at $\sqrt{s_{NN}}$ = 200 GeV. The shaded bands indicate the systematic uncertainty related to the number of participant and number of binary collision scaling calculations [30].

and $K^{\pm}$. A possible explanation for this phenomenon is the production of particles via recombination or coalescence of quarks, which is discussed in more detail in the following section.

### 1.3.3 Baryon/meson ratios

In addition to studying the comparison of central and peripheral $p_T$ spectra for the same particle species by means of the nuclear modification factor, studies of the $p_T$ dependence of the spectra for different particle species may provide further insight into possible particle production mechanisms. A further interesting phenomenon which has been observed at RHIC, is the enhancement in the yields of baryons compared to mesons at intermediate $p_T$, and which is in contrast to pQCD calculations [34]. The large ratios are illustrated for the case of the $\Lambda$ baryon compared to the $K_S^0$ meson in Fig. 1.13 [35] and have also been observed in the $p/\pi$ and $\bar{p}/\pi^-$ ratios at RHIC [36, 37].

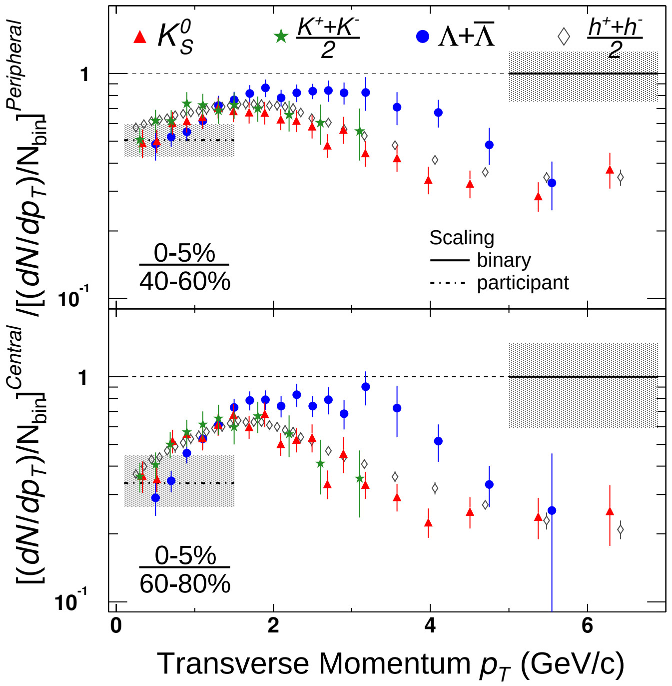


**Figure 1.12**: The upper and lower panels show the nuclear modification factor $R_{CP}$ for the centrality intervals 0-5%/40-60% and 0-5%/60-80% respectively for the $K^0_S$, $K^{\pm}$ and $\Lambda + \bar{\Lambda}$ compared to charged hadrons measured by STAR [33].

### Recombination models

Models of particle production based on quark recombination or coalescence have been used to describe the differences between meson and baryon distributions as a function of $p_T$ [34, 38–40]. In these models, the underlying parton distribution of the created medium is usually assumed to be described by an exponential distribution (i.e. thermally equilibrated) while the shape of the distribution of hard partons, created in initial hard scatterings of the incoming nucleons, should be described by a power-law function (according to pQCD expectations). The two contributions are shown in the left-hand panel of Fig.1.14 from [34]. The right-hand panel of Fig.1.14 [41] is a sketch showing the production of a meson with $p_T \sim 6$ GeV/$c$ from a steeply falling underlying parton spectrum through the competing processes of recombination of two $\sim 3$ GeV/$c$ quarks vs. the fragmentation of a parton with higher

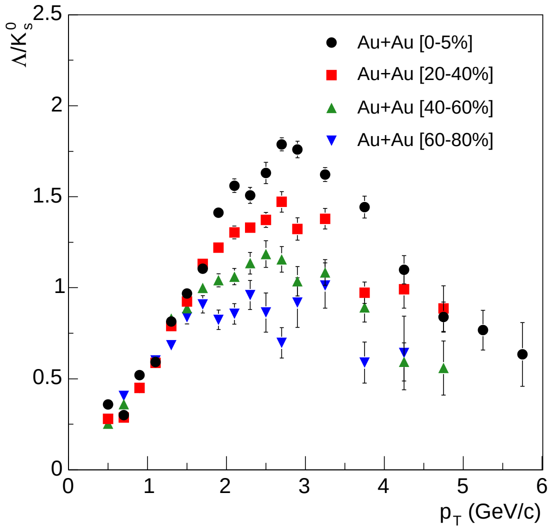


**Figure 1.13**: The $\Lambda/K_S^0$ ratio vs. $p_T$ as a function of centrality for Au+Au collisions at $\sqrt{s_{NN}} = 200$ GeV measured by STAR [35].

$p_T$. The regions of $p_T$ where one or the other mechanism dominates is dependent on the slope and normalization of the underlying parton spectrum; for a steeply falling exponential spectrum, recombination should dominate over fragmentation while the opposite is true if the spectrum has a pQCD power-law shape [34]. The idea that quark recombination may be the dominant particle production mechanism at intermediate $p_T$ at RHIC is one of the proposed explanations for the large baryon/meson ratios observed [34,38–40].

In the coalescence picture, the recombining entities are constituent quarks (i.e. the gluons are not degrees of freedom in the model.) and the shapes of the resulting $p_T$ distributions of mesons and baryons will therefore have a dependence on their quark number content. While these models have been successful in qualitatively describing the data measured at RHIC, it should also be kept in mind that they are phenomenological models containing assumptions and free parameters which need to be fitted to data.

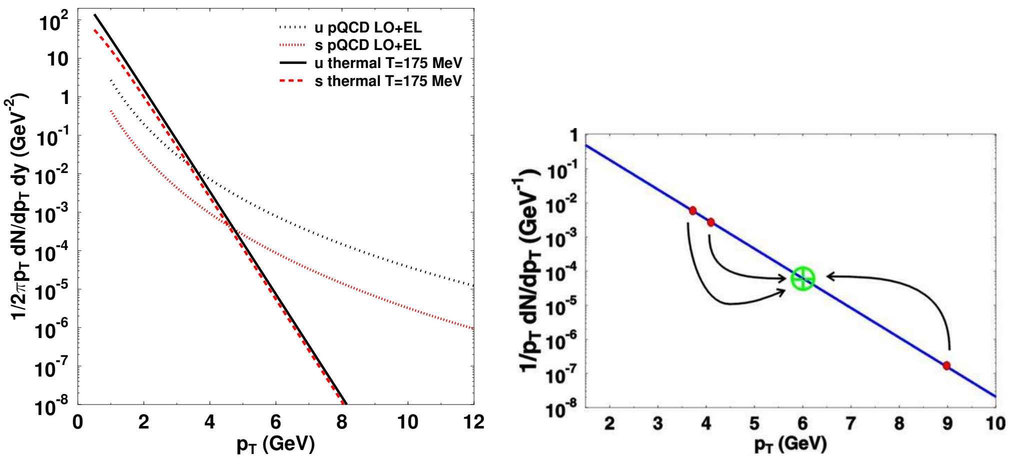


**Figure 1.14**: **Left panel:** The spectrum of $u$ and $s$ quarks at hadronization where the thermal (exponential) and pQCD distributions are indicated by the legend, taken from [34]. **Right panel:** A sketch of recombination and fragmentation for a meson with $p_T \sim 6$ GeV/$c$ from a steep parton $p_T$ spectrum (solid line), taken from [41]. The two arrows to the left of the circle indicate the formation via recombination of 2 quarks of $p_T \sim 3$ GeV/$c$ each, while the arrow on the right indicates that a higher $p_T$ parton is required to fragment to create the lower $p_T$ meson.

### 1.3.4 Elliptic flow, $v_2$

#### Probing the system at early time

Non-central nucleus-nucleus collisions give rise to an elliptic overlap area. The spatial eccentricity, $\epsilon$, of the reaction region is given by:

$$\epsilon = \frac{\langle y^2 \rangle - \langle x^2 \rangle}{\langle y^2 \rangle + \langle x^2 \rangle} \tag{1.9}$$

and can be calculated using Monte Carlo Glauber calculations based on the average $N_{part}$ spatial distributions using an assumed nuclear density profile (usually a Woods-Saxon distribution).

This initial spatial anisotropy which is produced at the initial collision time, can be converted into a momentum-space anisotropy if the produced particles interact with each other sufficiently to produce pressure gradients (i.e in the thermodynamic limit, the system would be in local thermal equilibrium). As a result of these pressure gradients, the system expands more strongly along the short axis of the ellipse, quenching the anisotropy signal with time. Therefore, measuring the anisotropic distribution of particles can provide information on the system dynamics from the earliest stage of the system's evolution. For a nucleus-nucleus collision, the azimuthal distribution of produced particles can be described in terms of a Fourier series [42]:

$$E\frac{d^3N}{d^3p} = \frac{1}{2\pi}\frac{d^2N}{p_T dp_T dy}\left(1 + \sum_{n=1}^{\infty} 2v_n \cos\left(n(\phi - \Psi_r)\right)\right) \tag{1.10}$$

where $p_T$ and $y$ are the transverse momentum and rapidity of a particle, $\phi$ is its azimuthal angle, $v_n$ are the Fourier coefficients (anisotropy parameters) and $\Psi_R$ is the reaction plane azimuthal angle. The reaction plane is defined as the plane described by the vector between the centres of the colliding nuclei and the direction of the beam axis. Together, the first two Fourier coefficients, $v_1$ and $v_2$ are known as the *anisotropic flow* while separately, $v_1$ is called the *directed flow* and $v_2$ is called the *elliptic flow* because in polar coordinates, for small values of $v_2$, the azimuthal distribution with non-zero second harmonic describes an ellipse.

Significant elliptic flow has been observed for a large variety of hadrons by the RHIC experiments [43, 44] and results for identified particles from Au+Au collisions at $\sqrt{s_{NN}} = 200$ GeV measured by the STAR and PHENIX experiments are presented in Fig. 1.15 [22].

At low $p_T$ ($\lesssim 2$ GeV), $v_2(p_T)$ for the different hadrons has been observed to scale with particle mass. This can also be seen in Fig. 1.15. In an ideal hydrodynamical picture, assuming thermal equilibrium of the system, this is an expected observation, since all particles are boosted with a common velocity, giving rise to a higher $p_T$ for heavier particles. In other words, the same $v_2$ value will be observed for more a massive particle at a higher $p_T$ than for a lighter particle.

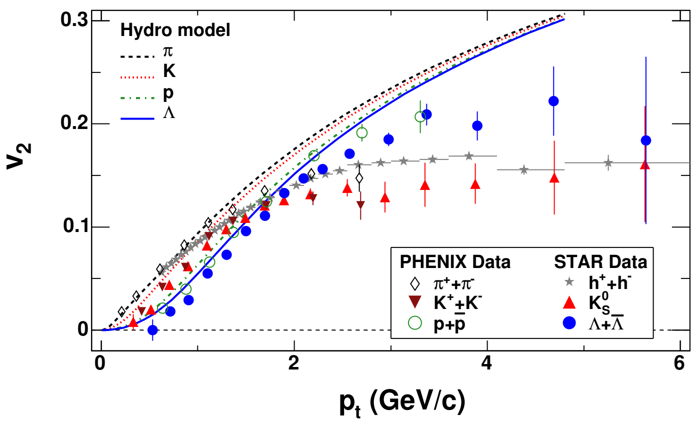


**Figure 1.15**: Measurements of $v_2(p_T)$ for identified particles measured by the STAR and PHENIX experiments compared to hydrodynamical calculations [22].

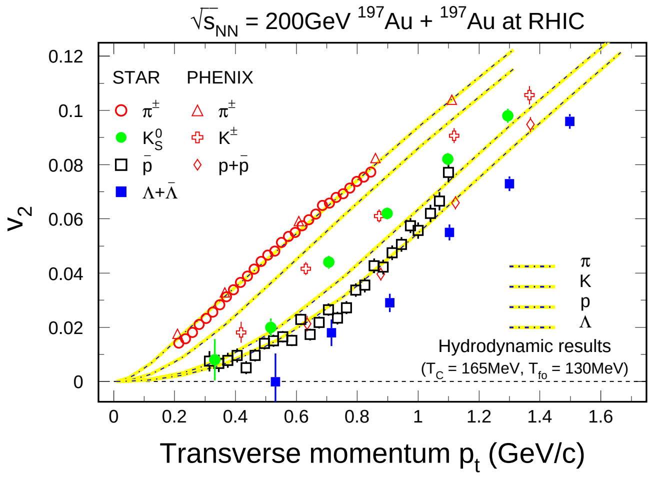


**Figure 1.16**: $v_2(p_T)$ results from the STAR and PHENIX experiments for charged $\pi$, $K_S^0, \bar{p}$ and $\Lambda+\bar{\Lambda}$ taken from [45]. The dot-dashed lines are hydrodynamics calculations (see [45] for details).

Hydrodynamical model expectations with different assumptions for the initial conditions and equation of state (EOS) of the produced system can be compared with the elliptic flow measured in experiment to investigate the properties of the produced medium. Ideal hydrodynamics assumes that matter is in local thermal equilibrium and therefore is most likely to be applicable in the low $p_T$ range since it is assumed that higher $p_T$ particles produced in initial hard scatterings are unlikely to reach thermal equilibrium with the surrounding medium over the lifetime of the system. Hydrodynamical models based on initial conditions including a QGP EOS have been successful in describing the RHIC elliptic flow results at low $p_T$ [45], an example is presented in Fig. 1.16 [45].

However, most of these hydrodynamical models assume longitudinal boost invariance and are not calculated in three dimensions. Measurements of $v_2$ as a function of pseudorapidity by the PHOBOS and STAR experiments [43, 46] show a strong dependence of $v_2$ on pseudorapidity, implying that the boost invariance assumptions may not be valid. In addition, the contributions to the $v_2$ signal from rescatterings of particles in the hadronic stage cannot be modeled by pure hydrodynamics. Therefore, the good agreement with hydrodynamics calculations is not enough to conclude on the system properties alone.

**Quark number scaling**

At intermediate $p_T$ ($2 \lesssim p_T \lesssim 6$ GeV/$c$), the measured $v_2$ values for identified particles appears to saturate as can be seen in Fig. 1.15. Also, the $v_2(p_T)$ for baryons and mesons appears to saturate at different values, i.e. the baryons all seem to follow one trend while the mesons collectively saturate at a lower $v_2$ value. However, if the $v_2(p_T)$ values are divided by the number of quarks per particle (i.e. 2 for mesons and 3 for baryons), a scaling has been observed for $p_T/n_q \gtrsim 1$ GeV/$c$. The top panel of Fig. 1.17 shows the elliptic flow scaled by the number of constituent quarks, $v_2/n_q$ vs. $p_T/n_q$ for identified particles measured by the STAR experiment [45]. The dash-dotted line is a polynomial fit to the data which is used as the denominator in the ratios shown in the bottom panel of Fig. 1.17. The bottom panel shows that for $0.75 \lesssim p_T/n_q \lesssim 2$ GeV/$c$, the $v_2$ for the identified particles scales with the number of consituent quarks since all the ratios (except the pions) fall on a common line. The large resonance decay contribution to pion production has been suggested as a possible explanation for their apparent violation of the scaling [47].

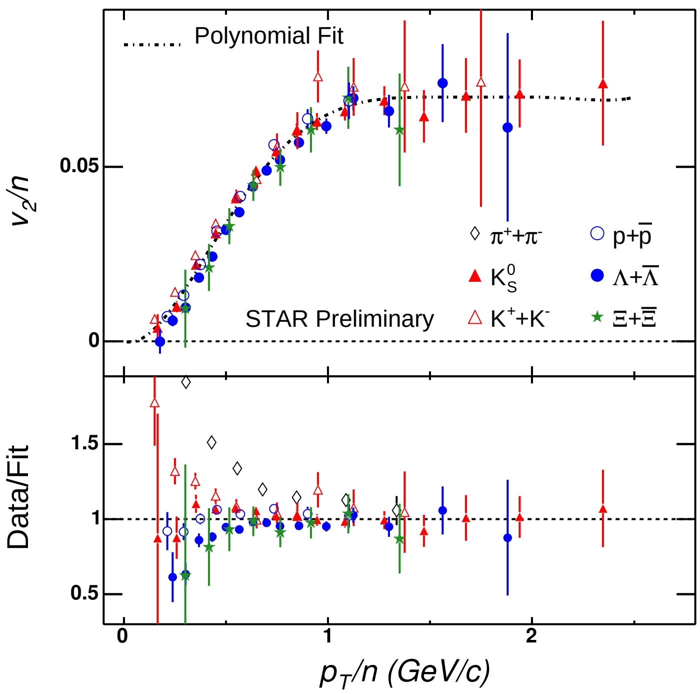


**Figure 1.17**: **Top panel:** $v_2/n$ vs. $p_T/n$ where $n$ is the number of constituent quarks for identified particles measured by the STAR experiment [45]. The dash-dotted line is a polynomial fit to the data. **Bottom panel:** Data from the top panel divided by the polynomial fit as a function of $p_T/n$ [45].

Quark recombination models, which coalesce quarks with similar momenta, have been used to describe the observed scaling [34, 39, 40, 48]. These models assume that the constituent quarks carry a significant $v_2$ signal themselves, before coalescing to form a hadron which then has a combination of the $v_2$ of its constituent quarks. In the context of these models, the implication is that elliptic flow is developed in the pre-hadronic stage which requires collectivity of the degrees of freedom in the pre-hadronic stage.

Hadronic transport models, RQMD[1] [49] and UrQMD[2] [50], can also qualitatively reproduce the observed mass ordering of $v_2(p_T)$ at low $p_T$ [51] and quark-number scaling at higher $p_T$ [52] based on rescattering of hadrons.

[1] Relativistic Quantum Molecular Dynamics

[2] Ultra-relativistic Quantum Molecular Dynamics

The quark number scaling is due to the model calculations' dependence on the additive quark model for hadronic interaction cross-sections. However, although these models can qualitatively reproduce the observed trends, the calculated $v_2(p_T)$ values are only $\sim 60\%$ of the experimentally observed values. This may indicate that significant flow is built up prior to hadronization in the partonic stage, since hadronic scatterings alone cannot reproduce the large experimentally observed values.

Therefore in the context of both recombination models and hadronic transport models, the observed $v_2$ values seem to indicate that elliptic flow is built up prior to hadronization in the partonic phase.

## 1.4 The $\phi$-meson as a probe of the medium created at RHIC

The $\phi$ vector meson is the lightest bound state of hidden strangeness, consisting of a $(s\bar{s})$ quark-antiquark pair. Although it is a meson, it is heavy in comparison with mesons consisting of $u$ and $d$ quarks, having a mass ($m_\phi = 1019.456 \pm 0.020$ MeV/$c^2$) [53] comparable to the proton and $\Lambda$ baryons. Due to the $\phi$ being composed solely of a $s$ and $\bar{s}$ quark, phenomenologically it is expected to have a very small cross-section for interactions with non-strange hadrons [54] and therefore, its observables should remain largely undisturbed by the hadronic rescattering phase of the system's evolution. Recent measurements of $\phi$-photoproduction from various nuclei [55, 56] have reported a range of values for the extracted $\phi$-nucleon cross-section but yet remain to be conclusive. However, experimental evidence for the small interaction cross-section of the $\phi$ is presented in Fig. 1.10 where the values for the freeze-out temperature $T_{fo}$ and mean velocity $\langle\beta\rangle$ extracted from blast-wave fits to the central $\phi$-meson $p_T$ spectrum differ from those extracted for $\pi, K, p$ in that $\phi$ seems to freeze out at a higher temperature and lower $\langle\beta\rangle$ [22]. This is also observed for the multistrange $\Omega$ baryon. The $\phi$ also has a relatively long life-time of $\sim$46 fm/$c$ which means that it will mostly decay outside the fireball and therefore its decay daughters will not have much time to rescatter in the hadronic phase. Previous experimental measurements of the $\phi/K^-$ ratio as a function of centrality have also ruled out the possibility of $\phi$ production via $K^+ + K^-$ coalescence in the hadronic stage [57]. The observed ratios are flat as a function of centrality in contradiction to expectations from hadronic rescattering models which include kaon coalescence as a $\phi$-meson production mechanism and which therefore predict the $\phi/K^-$ ratio to increase as a function of centrality. These properties make the $\phi$-meson an excellent probe of the hot and dense medium created in nucleus-nucleus collisions.

Measurements of the $\phi$-meson in terms of the bulk observables discussed in the previous section can provide important information on the properties of the medium and particle production mechanisms in ultra-relativistic Au+Au collisions. For example, measurements of the $\phi$-meson $p_T$ spectra and their dependence in terms of shape and normalization on centrality may shed light on the constituents of the medium at the time of $\phi$ formation as well as the mechanism through which the $\phi$-mesons are formed. Studies of the $\phi$-meson nuclear modification factor, $R_{CP}$, and how the $\phi$ scales in this observable compared to other identified particles can help to constrain particle production models such as quark recombination since the $\phi$ is a meson but is as heavy as the $\Lambda$ and can therefore be used to distinguish between particle-type vs. mass dependencies. From a previous measurement of the $\phi$-meson $R_{CP}$ by STAR [57] it was not possible to draw a definite conclusion on its possible scaling due to limited statistics and therefore a higher statistics measurement may help to settle this question.

Further insight into mechanisms of particle production for strange particles compared to non-strange particles, can be gained through measurements of the particle ratios of multistrange hadrons. Measurements of the $N(\Omega)/N(\phi)$ ratios compared to the ratios of particles consisting of $u$ and $d$ quarks, for example $N(p)/N(\pi)$ and $N(\Lambda)/N(K^0_S)$, may help to highlight differences in the production mechanisms of strange particles and non-strange particles and help constrain models of particle production. For example, expectations from one quark recombination model [58] which includes the coalescence of thermalized strange quarks from the medium as the dominant production mechanism for $\Omega$ baryons and $\phi$-mesons, are that the $N(\Omega)/N(\phi)$ ratio increases monotonically as a function of $p_T$ up to $p_T \sim 5.5$ GeV/$c$. Comparison of data with the model expectations may allow us to learn how close the medium at RHIC is to being thermalized.

The degree of collectivity of the medium produced at RHIC can be further probed by measuring the elliptic flow of the $\phi$-meson. Since multistrange hadrons and particles with hidden-strangeness are assumed to freeze out early and undergo fewer interactions in the hadronic stage, their $v_2$ signals should provide a clean signal from the early stage of the system's evolution. First measurements of the $\Xi$ ($ssd$) and $\Omega$ ($sss$) elliptic flow have indicated that these particles flow at least as much as particles consisting of the lighter $u$ and $d$ quarks alone [59] which implies that collectivity of the system is built up in the partonic stage. Measurements of the $\phi$-meson $v_2$ and whether it also scales according to its number of constituent quarks as other identified particles are seen to do, will provide important information on the collectivity and possible deconfinement of the system in the early stage and serve to constrain different dynamical models of elliptic flow (e.g. hydrodynamical and hadron transport models) and particle production.

The $\phi$-meson with its mass comparable to $\Lambda$ and $p$, and low interaction cross-section, can be exploited as an ideal tool to probe the bulk properties of the medium produced in nucleus-nucleus collisions at RHIC. In addition to the wealth of data on other identified particles, $\phi$-meson observables may help to distinguish further between different physical models of the dense medium and help to open the way towards further understanding of the system created in ultra-relativistic heavy-ion collisions.

## 1.5 Thesis scope

The aim of the work in this thesis is to probe the properties of the medium created in Au+Au collisions at RHIC using the $\phi$-meson reconstructed through its decay channel, $\phi \to K^+K^-$. To this end, the analysis presented in the following chapters has used the highest statistics, to date, Au+Au collisions dataset recorded by the STAR experiment (RHIC run IV (2004)), to measure a range of observables for the $\phi$-meson.

Studies of $\phi$-meson production in Au+Au collisions have been performed using the STAR detector in previous years [57, 60]. One of the goals of the analysis presented in this thesis is to extend the previous STAR measurements using the higher statistics dataset to study $\phi$-meson production in more differential detail, and probe more precisely variations in various observables as a function of collision centrality. The $\phi$-meson $p_T$ spectra presented in this work have been measured in narrow centrality intervals allowing a detailed study of their shape evolution as a function of centrality. These high statistics spectra results have also allowed the measurement of the $\phi$ nuclear modification factor, $R_{CP}$, for two different centrality combinations allowing detailed comparison with measurements of other identified particles and for the discrimination of scaling behaviour for the $\phi$-meson.

Using the extracted $\phi$-meson $p_T$ spectra, the centrality dependence of the baryon/meson yield ratio, $N(\Omega)/N(\phi)$, has been measured for the first time and is compared to the ratios of other identified particles as well as expectations from particle production models based on quark recombination.

The other main goal of this work is to probe the collectivity of the medium produced at RHIC. This is done by measuring, for the first time in Au+Au collisions, the centrality dependence of the $\phi$-meson elliptic flow, both in the differential form, $v_2(p_T)$, and $p_T$-integrated form, $\langle v_2 \rangle$. As part of the analysis, a new method of extracting the $v_2(p_T)$ for identified particles is shown to be applicable using data from the 62.4 GeV Au+Au dataset, and is then used to obtain the results presented for Au+Au collisions at both 62.4 and 200 GeV. The measurement of $\phi$-meson $v_2(p_T)$ in minimum bias (0-80%) Au+Au collisions at 200 GeV is of sufficient precision to allow conclusions to be drawn concerning quark number scaling for the $\phi$-meson $v_2$.

The outline for this thesis continues as follows: Chapter 2 presents the RHIC complex and STAR detector in more detail. The analysis techniques and methods used to measure the $\phi$-meson observables are dicussed in Chapter 3, followed by the presentation and discussion of the results in Chapter 4. In Chapter 5 we conclude and present an outlook for future measurements.

# Chapter 2

# Experimental Facilities

## 2.1 The Relativistic Heavy Ion Collider (RHIC)

The Relativistic Heavy Ion Collider (RHIC) at Brookhaven National Laboratory is the first machine which can collide heavy ion beams at relativistic energies. Previous heavy ion experiments were performed using accelerated heavy ion beams impinging on fixed-targets of heavy ions (e.g. SPS at CERN and AGS at BNL).

RHIC was designed to be able to collide particles with mass number from $A = 1$ (i.e. protons) up to at least $A \sim 200$ (i.e Au has $A = 196$) over a wide range of energies with a top energy for protons of $\sqrt{s} = 500$ GeV and a top energy for Au of $\sqrt{s_{NN}} = 200$ GeV. Therefore RHIC provides the highest energy heavy ion collisions ever produced (so far!) as well as the possibility of low energy running in energy regimes overlapping with those of previous heavy ion experiments. In addition to the heavy ion physics programme at RHIC, there is also an active spin physics programme with the aim of studying the spin structure of the nucleon. Therefore, RHIC was designed to also run polarized proton-proton collisions (with the addition of spin rotator magnets called Siberian Snakes) as part of the spin physics programme. The design luminosity for Au+Au is $2 \times 10^{26}$ cm$^{-2}$s$^{-1}$ and for p+p it is $1.4 \times 10^{31}$ cm$^{-2}$s$^{-1}$ [61].

With RHIC it is also possible to collide two different species of particles with each other since the collider rings are independent and have their own magnet setups. This allows independent tuning of the magnetic fields in each ring which is required to achieve equal rotation frequencies of the different particle species in each ring. Two Tandem Van de Graaff accelerators allow for independent initial acceleration of the different particle species to be collided. In the case of proton + X collisions, the proton linac provides the initial acceleration of protons.

RHIC construction was completed at BNL in 1999 and the first commissioning runs with Au+Au collisions took place in 2000. This was also the first year of physics running with Au+Au at $\sqrt{s_{NN}} = 130$ GeV. Since 2000, RHIC has been used to collide various particle species at a number of collision energies as summarised in the table below:

| **Year** | **Particle Species** | **Particle Energy (GeV/n)** |
|---|---|---|
| 2000 | Au+Au | 65.2 |
| 2001/02 | Au+Au | 100.0 |
| | p+p | 100.0 |
| 2002/03 | d+Au | 100.0 |
| | p+p | 100.0 |
| 2003/04 | Au+Au | 100.0 |
| | Au+Au | 31.2 |
| | p+p | 100.0 |
| 2004/05 | Cu+Cu | 100.0 |
| | Cu+Cu | 31.2 |
| | Cu+Cu | 11.2 |
| | p+p | 100.0 |
| 2006 | p+p | 100.0 |
| | p+p | 31.2 |

**Table 2.1**: Summary of RHIC physics running by year, particle species and collision energy. Data summarised from [62].

The various facilities required to produce collisions of heavy ions at the top RHIC energy of $\sqrt{s_{NN}} = 200$ GeV are described below and outlined schematically in Figure 2.1:

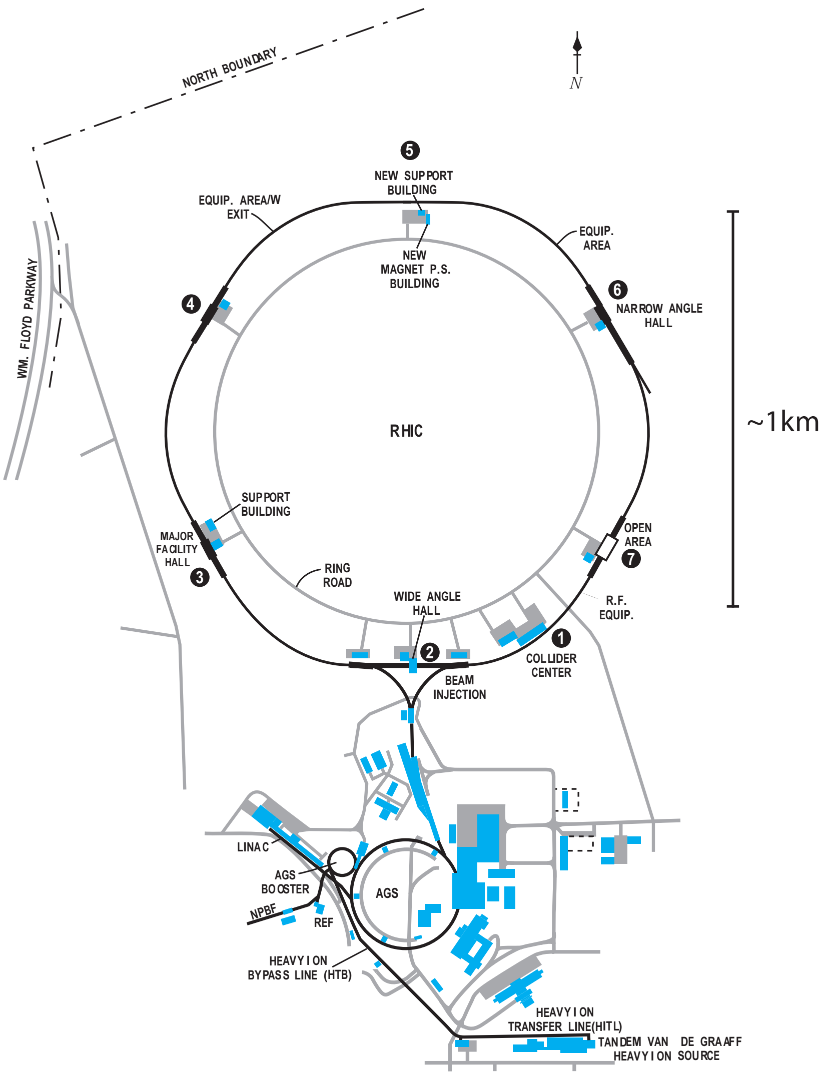


**Figure 2.1**: Overview of the RHIC accelerator complex [63].

- **Tandem Van de Graaff Accelerator:**
  The Tandem Van de Graaff accelerator produces the initial acceleration of Au ions after their extraction from the pulsed sputter ion source. When the Au ions enter the Tandem, they are negatively charged. The ions are accelerated in a two stage process involving the partial stripping of electrons, and exit the Tandem with an energy of 1 MeV/$u$.

- **Tandem-to-Booster Line (TTB):**
  At the exit of the Tandem, the ions are further stripped of electrons and enter the 850 m long TTB transfer line in a charge state of $^{+32}$Au.

- **Booster Synchrotron:**
  The Booster synchrotron further accelerates the ions to 95 MeV/$u$ and upon exiting the Booster, a foil strips more electrons off the ions so that they enter the AGS with a charge state of $^{+77}$Au. The electron stripping causes the number of ions to be halved from $\sim 4.3 \times 10^9$ (on leaving the Tandem) to $\sim 2 \times 10^9$ upon injection into the AGS [63].

- **Alternating Gradient Synchrotron (AGS):**
  The AGS is filled with 24 ion bunches in 4 Booster cycles. The bunches are then debunched and rebunched into 4 bunches each corresponding to one Booster filling. The AGS accelerates the Au ions to 8.86 GeV/$u$. The remaining 2 electrons are stripped off the ions at the exit of the AGS.

- **AGS-to-RHIC transfer line (ATR):**
  The Au ion bunches, containing $\sim 1 \times 10^9$ ions each, travel down the ATR before being injected into the RHIC rings.

- **RHIC Rings:**
  The Relativistic Heavy Ion Collider consists of two independent rings of superconducting magnets which bend and focus the ion beams. The rings are approximately circular in shape (3.8 km circumference), are positioned in the same horizontal plane and intersect at six points which allows six interaction points for particle collisions. Each of the rings consists of six arc sections and six straight insertion sections. The particle beam pipe runs through the centre of the magnets which are kept cooled at T<4.6 K. The rings operate as accelerator rings and then as storage rings once the beams have reached full colliding energy.

  From the AGS, the ions are filled into RHIC one bunch at a time and the nominal configuration of 56 bunches in the 360 RF buckets per ring (plus 4 unfilled buckets) is achieved through 14 AGS cycles. The ions are accelerated to the top energy of 100 GeV/$u$ in a period of $\sim$2 minutes by the acceleration RF-system. Once top energy has been attained, the storage RF-system (which has a higher frequency than the acceleration RF-system for limiting the bunch length growth from intra-beam scattering) maintains cycles at the top energy.

- **Proton Linac:**

> The Proton Linac is used in the polarized p+p programme to accelerate polarized protons before injection to the Booster, AGS and finally RHIC.

The four RHIC experiments are each located at an intersection point of RHIC. In increasing order of collaboration size, the experiments are: BRAHMS (Broad Range Hadron Magnetic Spectrometers Experiment at RHIC), PHOBOS[1], PHENIX (Pioneering High Energy Nuclear Interaction Experiment) and STAR (Solenoidal Tracker at RHIC), and are positioned at 2 o'clock, 10 o'clock, 8 o'clock and 6 o'clock on the RHIC rings respectively. PHOBOS and BRAHMS were recently decommissioned, leaving only STAR and PHENIX to run currently at RHIC.

## 2.2 The Solenoidal Tracker at RHIC (STAR)

All the data analysed in this thesis were recorded using the STAR detector. STAR consists of a suite of integrated detectors designed to measure different observables. Figure 2.2 shows a three dimensional view of the experimental layout.

A cross-section view of STAR is presented in Figure 2.3.

Working outwards from the interaction region, the inner-most detector subsystem is the silicon vertex tracker (SVT) [64] consisting of three layers of silicon drift detectors positioned at 7, 11 and 15 cm from the beam axis. The SVT provides three-dimensional hit point measurements with high resolution (design resolution is 20 $\mu$m) to enable high precision particle tracking. Surrounding the SVT is another layer of silicon, the Silicon Strip Detector (SSD) [65], which provides further tracking information. The four layers of silicon detectors cover the full range in azimuthal angle ($\Delta\phi = 2\pi$) and one unit of pseudorapidity ($|\eta| \leq 1$).

[1]PHOBOS is a name, not an acronym

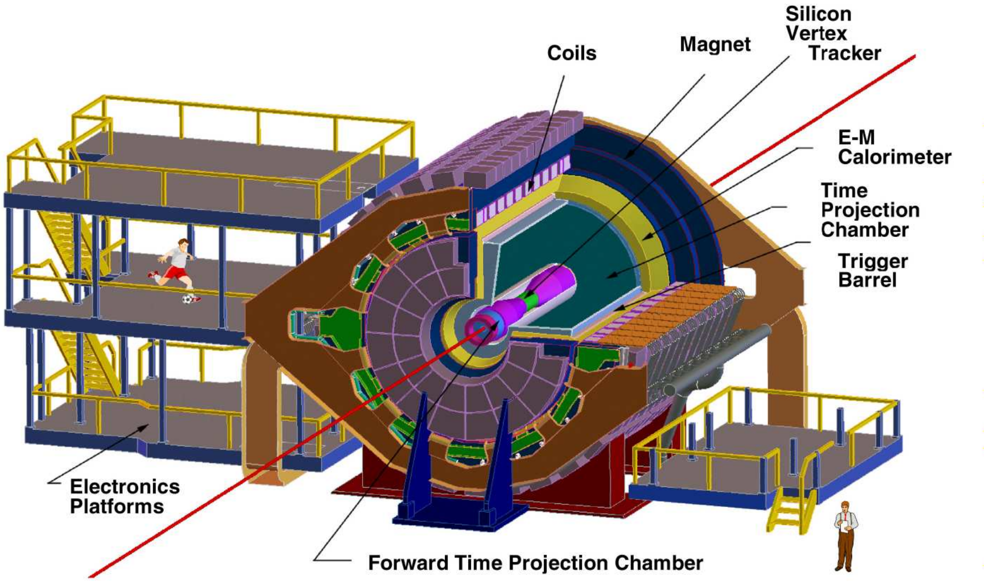


**Figure 2.2**: Three dimensional view of STAR with cut-away to show inner detector subsystems.

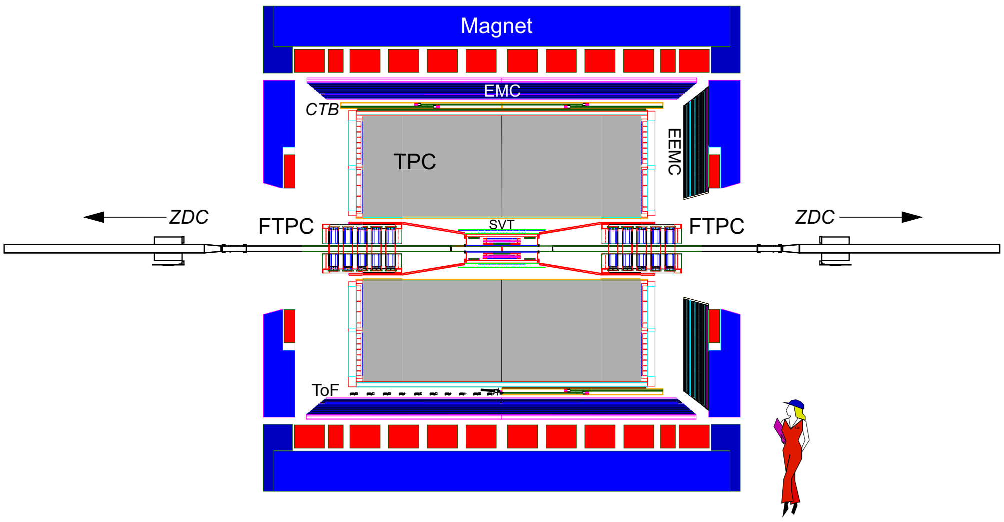


**Figure 2.3**: Cross-section view of STAR from the side, showing the layout of the detector subsystems.

The largest detector subsystem (by volume) in STAR is the Time Projection Chamber (TPC) [66] which allows charged particle tracking and identification. The TPC is a large cylinder with an inner radius of 50 cm and extending to 200 cm from the beam axis. It has an azimuthal acceptance of

$\Delta\phi = 2\pi$ and is 4.2 m long covering $|\eta| \leq 1.8$.

The two Forward Time Projection Chambers (FTPCs) [67] are radial drift TPCs and are located on each side of the TPC (east and west), each covering the full range of azimuthal angle ($\Delta\phi = 2\pi$) and $2.5 < |\eta| < 4.0$. The FTPCs extend STAR's tracking capabilities in the forward and backward $\eta$ directions.

Currently STAR has two Time Of Flight (TOF) detectors designed to enhance the STAR particle identification capabilities: the $\mathrm{TOF_p}$ covers a small acceptance of $\Delta\phi = 0.04\pi$ and $-1 < \eta < 0$ while the newer $\mathrm{TOF_r}$ tray (based on multi-gap resistive plate chamber technology) has a coverage of $-1 < \eta < 0$ and $\Delta\phi = \pi/30$. The STAR upgrade plan involves installing further $\mathrm{TOF_r}$ trays to cover the full $2\pi$ in azimuth. The pseudo-Vertex Position Detector (pVPD) located 5.4 m from the center of the TPC acts as the start timing detector for the TOF [68].

The Barrel Electromagnetic Calorimeter (BEMC) [69] surrounds the TPC ($|\eta| \leq 1$, $\Delta\phi = 2\pi$) and is designed to measure electromagnetic energy i.e. mainly photons and electrons. Since the BEMC is a fast detector it is used as part of the trigger set-up for the identification of certain events containing rare observables of interest (e.g. jet events, $J/\psi$ etc.). The Endcap Electromagnetic Calorimeter (EEMC) [70] extends the calorimeter pseudorapidity coverage to $-1 \leq \eta \leq 2$. Each of the calorimeters has a higher granularity shower-maximum detector layer to help distinguish between energy deposited by single photons or from the photon pairs arising from neutral pion or eta-meson decays.

The STAR magnet [71], which is approximately cylindrical in shape, surrounds the STAR detectors and acts as a support structure for them. The magnet was designed to provide a range of magnetic field strengths from $0.25 < |B_z| < 0.5$ T with a high degree of uniformity in order to optimise the tracking accuracy for high energy electrons (which leave almost straight tracks in the TPC) and the space-point reconstruction accuracy (which is needed to determine particle trajectories and momenta). The uniformity of the field is estimated as $|\Im_r| \equiv \left|\int_{z'=210cm}^{z} (B_r/B_{z'})dz'\right| \leq 2.3$ mm and

$|\Im_{\phi}| \equiv \left|\int_{z'=210cm}^{z}(B_{\phi}/B_{z'})dz'\right| \leq 1.0$ mm over the volume of the TPC [71]. A mean operating temperature of 29$^{o}$ C for the magnet is maintained by a closed loop water cooling system which has a flow rate of 1200 GPM through heat exchangers in order to dissipate the ∼3.5 MW of power from the magnet.

The main detectors used to gather the data analysed in this thesis were the set of trigger detectors (Zero Degree Calorimeters (ZDCs) and the Central Trigger Barrel (CTB)) and the TPC. These detectors are discussed in more detail in the following sections.

### 2.2.1 The Trigger Detectors

Since the various detector subsystems in STAR have different readout speeds, (which are slower than the heavy-ion interaction rate), not all events can be recorded by the data acquisition system (DAQ). Therefore, the STAR trigger system, which is based on input from the fast detectors, controls the selection of events. In addition, the trigger is used to select events with rare or specific signals of interest to increase the recorded statistics of these events. The trigger system for Run IV (2004) was composed of four different levels (0-3) with level 0 being the fastest and levels 1 and 2 slower since their algorithms were more complex. The fast detectors used for triggering (levels 0-2) in heavy-ion collisions are the two Zero Degree Calorimeters (ZDCs) (east and west) and the Central Trigger Barrel (CTB).

All four RHIC experiments include a pair of ZDCs to provide a standardized measure of the interactions at each interaction region. The STAR ZDCs are located ∼18 m upstream and downstream from the interaction region and subtend an angle of $\theta$ <2 mrad. The ZDCs are hadronic calorimeters designed to measure the energy from the remaining neutrons (called evaporation neutrons) from the colliding nuclei after collision [72]. Since they are positioned on the other side of the DX magnets to the interaction region, the remaining charged particles are bent away from the zero degree region and are not measured in the ZDCs. The energy deposited by the neutrons can be related to the multiplicity. The requirement for a minimum bias trigger is a coincidence between the ZDCs for summed signals greater than 40% of a single neutron signal [73]. The ZDCs are also used to locate the interaction vertex by using the time delay between the coincidences.

The CTB surrounds the TPC and measures the flux of charged particles at midrapidity. It is composed of 240 scintillator slats spanning $\Delta\phi = 2\pi$ and $|\eta| < 1$. The flux of charged particles at midrapidity is proportional to the impact parameter of an event and therefore the addition of the CTB allows more precise determination of the centrality of collisions. The correlation between the ZDC and CTB signals is shown in Figure 2.4 and provides a trigger for the different collision centralities.

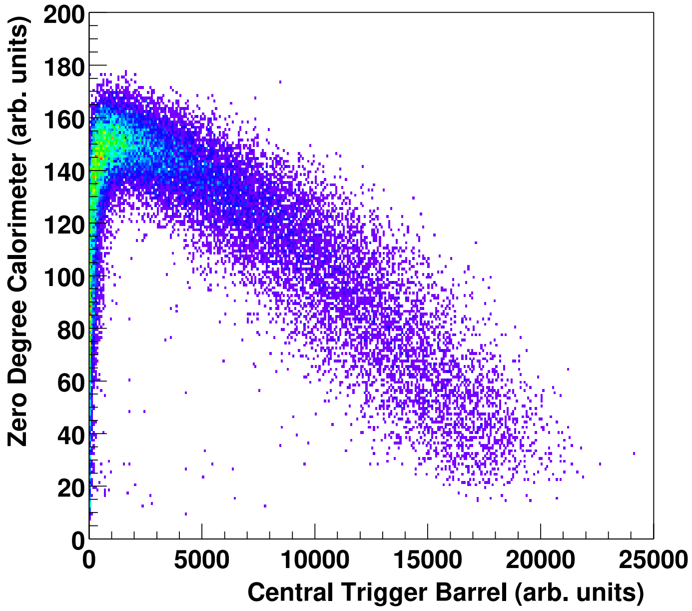


**Figure 2.4**: Correlation between the summed pulse heights from the ZDC and CTB for events with a primary collision vertex successfully reconstructed from tracks in the TPC [74].

The level 3 trigger was a software trigger and used information from the slower detectors namely the TPC, SVT and FTPC to do full event reconstruction online at a rate of 50 Hz for Au+Au collisions [75]. It also provided an online display for real time visual quality assurance.

### 2.2.2 The Time Projection Chamber

The STAR TPC is the largest currently operating TPC in the world and is the main tracking detector of the STAR experiment. It records the tracks of charged particles passing through its gas volume from which the particle momenta can be measured. It is also used to identify charged particles through measurements of their ionization energy loss ($dE/dx$) as they traverse the gas volume of the TPC.

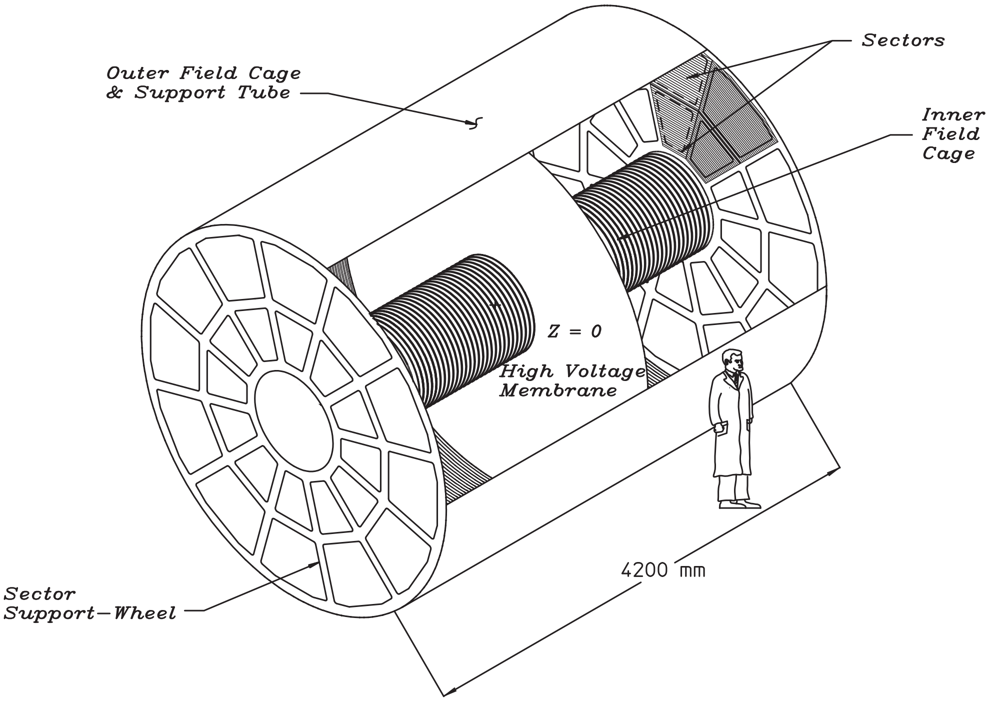


**Figure 2.5**: Three dimensional schematic diagram indicating the main structural elements of the STAR TPC. [66]

As shown in the schematic diagram in Figure 2.5 [66], the TPC mainly consists of a large barrel which contains P10 gas (10% methane and 90% argon) maintained at 2 mbar above atmospheric pressure. It is divided in half by a thin central membrane which provides the high voltage (28 kV) to maintain a uniform electric field of ~135 V/cm between it and the read-out endcaps which are maintained at ground. Concentric field-cage cylinders also help to maintain the uniformity of the electric field. Secondary electrons, released in ionization reactions between primary ionizing particles and the

TPC gas, drift in the electric field to the readout endcaps at each end of the TPC. It is critical to maintain a uniform electric field since track reconstruction requires precision at the submillimetre level while the maximum drift length for an electron is half the entire TPC length i.e. 2.1 m.

P10 gas is used in the TPC due to its fast drift velocity which has a maximum value at low electric field strengths. Lower field strengths require lower voltages which simplify the design of the detector. In addition, operating at the peak drift velocity allows more stability since small changes in temperature and gas pressure have negligible effects on the drift velocity.

The central membrane cathode consists of 70 $\mu$m thick carbon-loaded Kapton film pulled taught and secured to the outer field-cage by a support hoop to maintain a flat surface. It also has 36 aluminium stripes attached to each side which are used as targets for the TPC laser calibration system.

The TPC readout endcap planes are multi-wire proportional counter (MWPC) chambers with pad readout and are positioned on the support wheels. The MWPC chambers consist of three wire planes and a pad plane each. For each endcap there are 12 readout modules (sectors) which are positioned radially with respect to the hole defined by the inner field-cage with 3 mm gaps between each sector. One full sector of the anode pad plane is shown in Figure 2.6.

The outer subsectors have continuous pad coverage (32 padrows) with no spaces between the padrows to optimise $dE/dx$ resolution by maximising the measurement of the ionization electrons. The inner subsectors are in the region where the track density is higher and so they were optimised for two hit resolution by reducing the size of the pads. The space available for front end electronics limited the number of possible padrows on the inner subsectors (13 padrows). Therefore a track in the TPC can be sampled a maximum of 45 times if it crosses all 45 padrows.

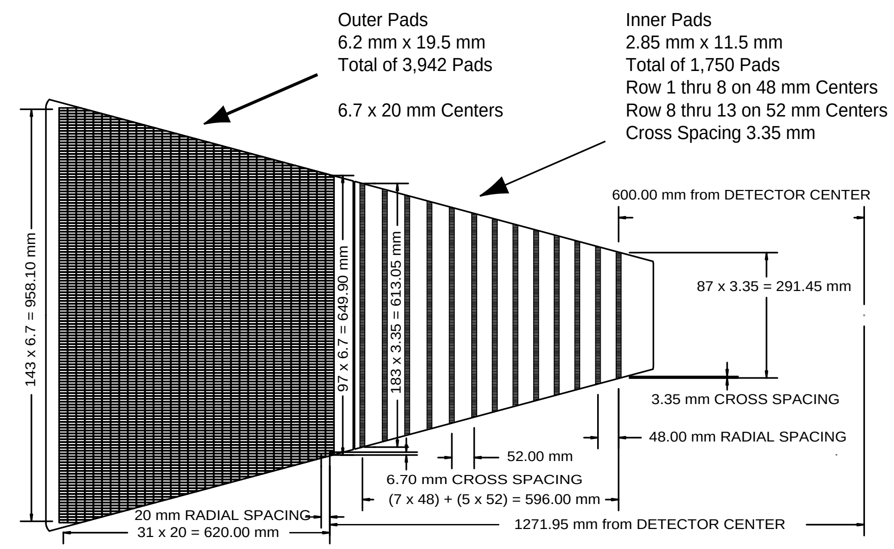


**Figure 2.6**: A sector of the TPC anode plane indicating the inner and outer subsectors and their respective padrows. [66]

### Track Reconstruction and Particle Identification in the TPC

A particle track is identified in the TPC through the ionization clusters the particle causes as it traverses the gas in the TPC. The $x$-$y$ and $z$-coordinates (where in this case the local $x$-direction is along the direction of a padrow, the $y$-direction points from the beamline outwards perpendicular to the $x$-direction, and the $z$-direction is the same as the beam axis) of these clusters are determined separately. The $x$-$y$ position of a cluster is found by measuring the signal (charge) in adjacent pads (along a single padrow) and fitting to find the most likely position, assuming a gaussian pad response function. The $z$-coordinate of a cluster is found by measuring the drift time from the point of origin of the cluster to the endcap and dividing by the average drift velocity. Therefore, in order to reconstruct the $z$ position precisely, the drift velocity must be known with a high degree of accuracy. This is ensured by setting the cathode voltage to produce an electric field in the TPC which corresponds to the peak in the drift velocity curve which leads to less sensitivity of the drift velocity with respect to changes in gas pressure, and also by regularly measuring the drift velocity, for calibration use later, by using lasers to make artificial tracks whose exact trajectories are known.

Once the positions of clusters have been found, the STAR tracking software is used to associate these space points to form tracks. The track model is a helix to first order, but also includes second order effects such as energy loss in the TPC gas and multiple Coulomb scattering which lead to a deviation in the track shape from a helix. The algorithm used to find tracks is iterative and makes use of a Kalman filter [76]. In the first stage of the algorithm, partial tracks, or track segments are identified by associating space points, starting with hits in the outer TPC padrows. The segments then undergo an initial segment fitting procedure taking into account energy loss in the TPC gas and multiple Coulomb scattering. At this stage, outlier space points are removed. A further track extrapolation step is then executed to take care of segment-joining. To take into account additional tracking information from the inner detectors (SSD and SVT), the global tracking algorithm associates the additional hit points with tracks from the TPC and refits to find a global track.

The tracking efficiency of the TPC depends on its fiducial acceptance, the electronic detection efficiency and two-hit resolution and was determined through simulations to be of the order of 80% for pions with $p_T > 2$ GeV/$c$ for central collisions.

By including the primary vertex as a space point on a track, (if the track indeed originates from the primary vertex), the momentum resolution of a track can be improved. The primary vertex position is determined as the global average position after extrapolating all the tracks reconstructed in the TPC back to the origin. The vertex position resolution improves with increasing centrality of collisions since more tracks are available for the calculation. In events containing more than 1000 tracks, the resolution is 350 $\mu$m [66]. If a global track has a distance of closest approach of less than 3 cm from the vertex, this track is refitted to include the vertex as an additional space point, yielding what is known as a primary track. Therefore, all primary tracks have an associated global track which has slightly different track parameters, since the vertex was not included in the global track fit.

As detailed in [66], the transverse momentum ($p_T$) of primary tracks is calculated by fitting a circle through the track space points (in $x, y$) and including the vertex $(x, y)$-position in the fit. The total momentum $p$ is then calculated using the radius of curvature extracted from this fit and the angle of the track with respect to the $z$-axis. The vertex position is excluded from the fit for tracks which are not primary tracks.

In addition to measuring their momenta, particles are also able to be identified in the TPC through their energy loss ($dE/dx$) due to interactions with atoms in the P10 gas. The $dE/dx$ is found from the energy loss measured on the endcap pads. Since the ionization fluctuations are too large to be compensated for by the distance over which the particle energy loss is measured, it is not possible to measure the average $dE/dx$ and the most probable $dE/dx$ is measured instead. This is done by calculating the truncated mean of 70% of the clusters (removing the 30% largest ionization clusters). The TPC $dE/dx$ resolution of 7-8% allows the separation of protons and pions up to 1.0 GeV/$c$ [66]. Figure 2.7 shows the $dE/dx$ vs. momentum $p$ for tracks in the TPC. The different particle bands can be clearly seen (note the color scale is a log scale).

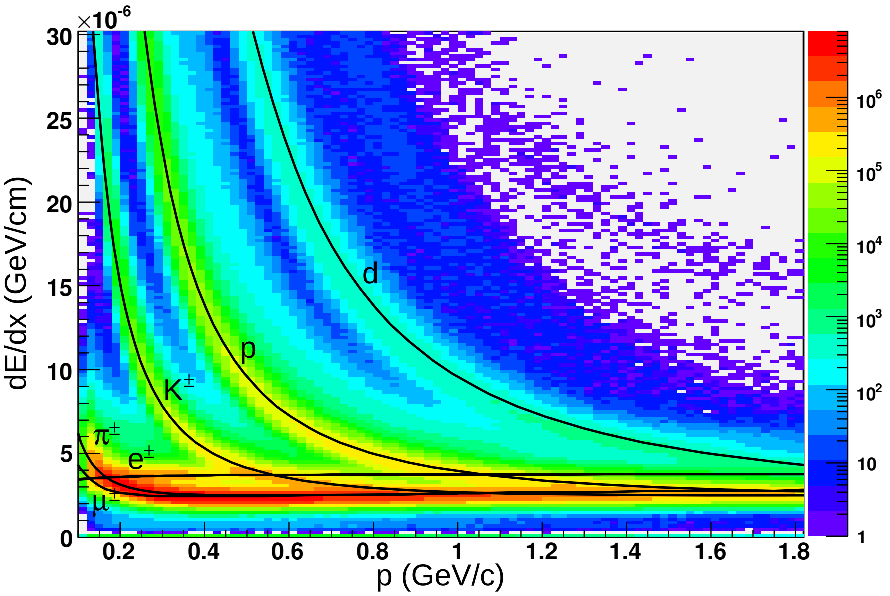


**Figure 2.7**: $dE/dx$ vs. $p$ from the STAR 62.4 GeV dataset. The lines represent the truncated mean values for the different particles [77]. The different particle bands for $e, \mu, \pi, K, p$ and $d$ are clearly visible. Note that the color scale is a log scale.

## 2.3 Computing Facilities

Computing facilities are an integral part of heavy ion experiments. The huge data volumes (of the order of many TB) recorded by experiments result in processing times for data reconstruction (i.e. processing of the data into a usable format for analysis) being longer than the time taken to actually record the raw data. The need for fast access to these large data volumes for data analysis has helped to drive the high performance computing industry in terms of more robust storage and disk access technology in hardware and software. Without robust storage and the computing capacity for parallel data processing, analysis of data from heavy ion experiments in any reasonable time-frame would be impossible.

During a run, the data captured by each of the RHIC experiments is transferred from the experimental sites directly to the RHIC Computing Facility (RCF) at BNL for storage, processing and analysis. In terms of hardware, the RCF is primarily composed of a large processing farm (14 TFLOPS and more than 4000 processors), a distributed and centralised storage farm with a 1 PB capacity and robotic tape storage silos with a capacity of 7 PB.

The other main computing facility involved in data reconstruction, storage and processing for STAR is the National Energy Research Scientific Computing Center (NERSC) at Lawrence Berkeley National Laboratory (LBNL) in California. The linux farm at NERSC which is used for STAR data processing and analysis is the Parallel Distributed Systems Facility (PDSF) which consists of 700 processors with 100 TB of disk storage. (STAR is only one of the many high-energy and nuclear science physics experiments supported by PDSF.) STAR data are also stored on tape on the NERSC HPSS storage system which has a total capacity of 22 PB.

# 2.4 The Future

## 2.4.1 RHIC Upgrades

Over the next few years it is planned that RHIC will undergo major upgrades. In the near term ($\sim$2008) it is planned to increase the luminosity for both heavy-ion running ($8 \times 10^{26}$ cm$^{-2}$s$^{-1}$ for Au+Au at $\sqrt{s_{NN}} = 200$ GeV which is 4 times the original design luminosity) and p+p ($6\times10^{31}$ cm$^{-2}$s$^{-1}$ for $\sqrt{s_{NN}} = 200$ GeV and $1.5\times10^{32}$ cm$^{-2}$s$^{-1}$ for $\sqrt{s_{NN}} = 500$ GeV) by upgrading the RHIC vacuum system [78]. This near-term improvement in the luminosity for Au+Au is necessary to allow low energy running to gather reasonable statistics within realistic time-spans. Also planned is the replacement of the Tandem accelerators with a new Electron-Beam Ion Source (EBIS) which is due to be commissioned by 2009. The EBIS will be able to provide Uranium beams and polarized $^{3}$He ions. The longer term luminosity upgrade to RHIC II will involve the implementation of electron cooling technology to enable a further factor of 10 increase in the available Au+Au luminosity ($8 \times 10^{27}$ cm$^{-2}$s$^{-1}$) and a factor of 2-3 for polarized protons.

## 2.4.2 STAR Upgrades

In line with the RHIC upgrades, there are a number of upgrades planned for STAR as well. In order to make full use of the increased luminosity, the STAR Data Acquisition system is planned to be upgraded to work at 1000 Hz. In addition, the TOF will be upscaled to have full $2\pi$ azimuthal coverage and a pseudorapidity coverage of $-1 < \eta < 1$. A new silicon inner tracking device, the Heavy Flavor Tracker (HFT), which will enable the measurement of displaced vertices from charm decays is also planned to be installed.

### 2.4.3 The Large Hadron Collider (LHC)

In parallel to the RHIC upgrades, the new Large Hadron Collider (LHC) at CERN in Geneva, Switzerland, is due to begin running in 2007 and will collide $p$+$p$ at $\sqrt{s}$ = 14 TeV, and Pb+Pb at $\sqrt{s_{NN}}$ = 5.5 TeV. The LHC is the largest engineering project of modern times and has a circumference of 27 km. The LHC is planned to run heavy-ions for $\sim$one month per year. The dedicated heavy-ion experiment at the LHC is ALICE (A Large Ion Collider Experiment) while the other large detectors, CMS (Compact Muon Spectrometer) and ATLAS (A Toroidal LHC Apparatus) also have plans for heavy-ion programmes although they are primarily designed for p+p physics. The LHC will open a new domain in high-energy physics by colliding nuclei at higher energies than ever before.

# Chapter 3

# Data Analysis

## 3.1 Data Samples and Event Cuts

Data from Au+Au runs at $\sqrt{s_{NN}} = 62.4$ GeV and $\sqrt{s_{NN}} = 200$ GeV were used in the presented analysis. The 200 GeV data were from the 2004 Au+Au Run IV at RHIC.

The same event cuts were applied to both datasets. Analysed events were required to have a primary vertex $z$ position (where $z$ is in the direction of the beam axis) within 30 cm of the centre of the TPC (i.e. the nominal interaction point). The 62.4 GeV dataset consisted of minimum bias events only while the 200 GeV data analysed here consisted of two parts: a minimum bias dataset and a central-triggered dataset. In both cases, the minimum bias events were chosen according to the raw charged track multiplicity within a pseudorapidity window of $|\eta| < 0.5$ corresponding to 0-80% of the total measured cross-section. For the 200 GeV case, the central-triggered dataset was used to extract the 0-5% and 0-12% central data.

The approximate numbers of events analysed after imposing these cuts for each dataset and type of analysis are presented in Table 3.1. The reason that there were fewer events used for the $v_2$ analysis was that data from days where the recorded statistics were insufficient for the calculation of $\phi$-angle weighting information (see section 3.4) were excluded.

| $\sqrt{s_{NN}}$ **(GeV)** | **Dataset** | | **Events after cuts** $-$ $v_2$ | **Events after cuts** $-$ **spectra** |
|---|---|---|---|---|
| 62.4 | Minimum bias | (0-80%) | 6.9 M | – |
| 200 | Minimum bias | (0-80%) | 13.4 M | 16.7 M |
| 200 | Central | (0-5%) | 5.5 M | 8.4 M |
| 200 | Central | (0-12%) | – | 19.6 M |

**Table 3.1**: Data samples and number of events analysed per analysis type, after applied cuts.

## 3.2 Track quality cuts

The tracks used in all the presented analysis were primary tracks, meaning that the vertex is included as one of the tracks' fit points. To ensure optimal particle identification and momentum resolution, it is necessary to apply quality cuts to each track measured in the TPC. The cuts are presented in Table 3.2. As described in Chapter 2.2.2, each track has a number of fit points associated with it by the STAR tracking software. In order to ensure accurate track momentum reconstruction, short tracks were eliminated from the analysis by requiring all tracks to have a minimum number of 15 fit points. The effect of track-splitting by the tracking algorithm is minimised by further requiring that the number of fit points is more than half the number of total possible hit points for a track. All tracks were also required to be within a central rapidity range of $|\eta| < 1.0$.

In this analysis, $\phi$-mesons are measured through the decay channel $\phi \to K^+K^-$ (branching ratio = $49.2 \pm 0.6$ %) [53]. The kaon daughter particles are identified through their ionisation energy loss ($dE/dx$) in the STAR TPC. In this analysis, a track in the TPC is accepted as a kaon candidate if its $dE/dx$ value falls within 2 standard deviations of a parameterisation of $dE/dx$ vs. $p_T$ for kaons in P10 gas [77].

| **Cut description** | **Value** |
|---|---|
| | Single tracks |
| Number of fit points | $\geq 15$ |
| Ratio of fit points to possible points | $\geq 0.52$ and $\leq 1.02$ |
| n$\sigma$ cut on kaon $dE/dx$ | $\leq 1.99\|\sigma\|$ |
| $p_T$ cuts on kaons | $0.1 \leq p_T \leq 12.0$ GeV/$c$ |
| | Track pairs |
| dip-angle cut | $\geq 0.04$ rad |

**Table 3.2**: Description of track quality and kinematic cuts and values.

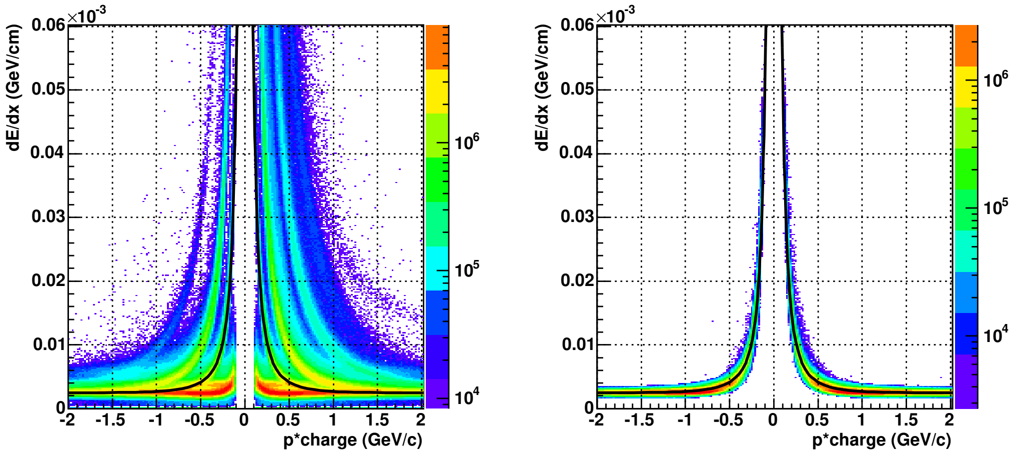


**Figure 3.1**: **Left:** $dE/dx$ vs. rigidity ($p\times$charge) for all charged particles as measured in the TPC (for Au+Au collisions at $\sqrt{s_{NN}} =$ 62.4 GeV). **Right:** $dE/dx$ vs. rigidity for all particles within $2\sigma$ of the energy loss parameterization for charged kaons. In both panels, the solid black curve indicates the truncated mean value of $dE/dx$ for positively and negatively charged kaons.

## 3.3 Spectral Analysis Method

$\phi$-mesons were reconstructed on a statistical basis through their decays to two charged kaons. For each event, the invariant mass, $m_{inv}$, distribution of the $\phi$ was constructed using all combinations of positively charged kaon candidates with negatively charged kaon candidates (called the *same-event* or signal distribution). Since not all charged kaons in each event orginate from $\phi$-meson decays, the $\phi$-meson signal extracted this way sits above a large combinatorial background of uncorrelated pairs. In order to exclude conversion electron pairs which may be misidentified as kaons in the $p_T$ range where the $dE/dx$ bands for kaons and electrons overlap, and which will cluster near the low $m_{inv}$ limit of the 2-kaon $m_{inv}$ distribution, kaon-candidate pairs with a dip-angle[1] $< 0.04$ rad [79] were excluded as $\phi$-meson candidates. The value for this cut was based on studies of the $\phi$-meson in Au+Au collisions at $\sqrt{s_{NN}} = 130$ GeV [60, 79].

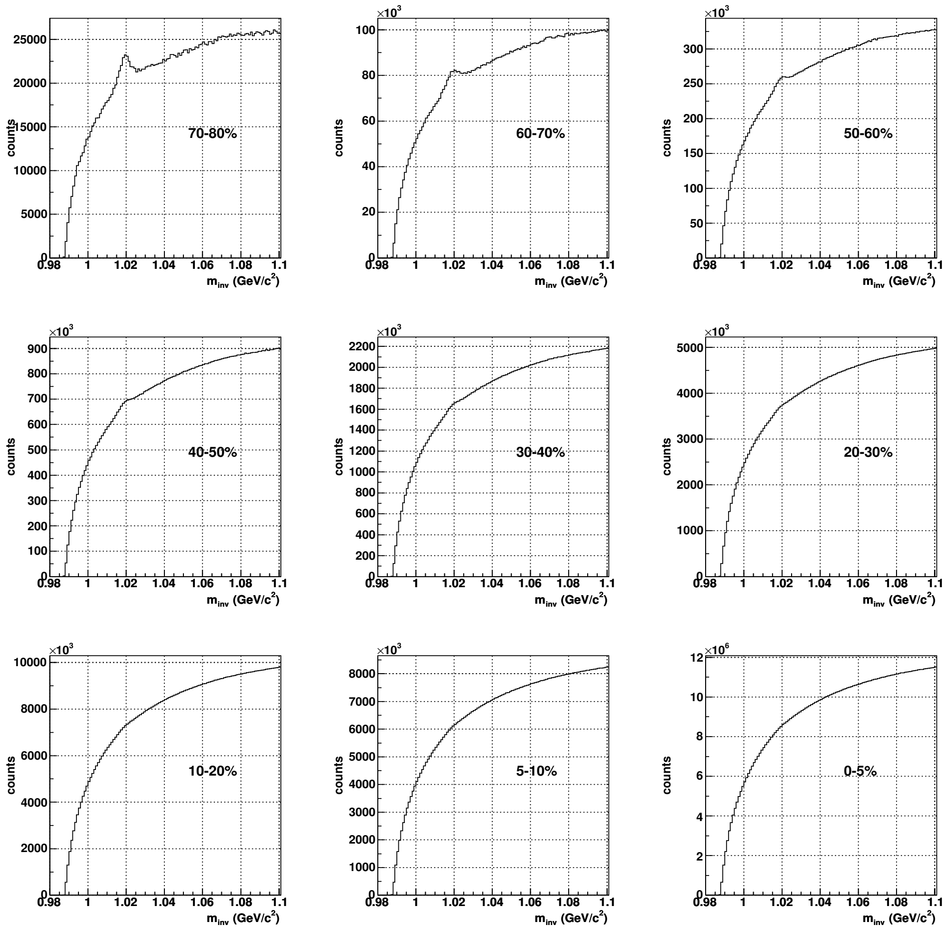


**Figure 3.2**: Same-event invariant mass distribution as a function of centrality from most peripheral (top left) to most central collisions (bottom right). (Au+Au collisions at $\sqrt{s_{NN}} = 200$ GeV.)

[1]The dip-angle $\theta$ is defined here using the momenta of particles $a$ and $b$ such that: $\cos\theta = (p_{Ta}p_{Tb} + p_{za}p_{zb})/(|p_a||p_b|)$

Figure 3.2 shows the evolution of the shape of the signal distribution as a function of centrality. The $\phi$ mass peak is much more prominent in the more peripheral events as a result of the smaller combinatorial background from uncorrelated kaon pairs.

### 3.3.1 Background estimation

The combinatorial background from the uncorrelated $K^+K^-$ pairs was estimated using the mixed-event technique [80]: an invariant mass distribution is constructed using all positively charged kaon candidates from one event mixed with all negatively charged kaon candidates from $n$ other events where $n$ can be set arbitrarily high to minimize effects from statistical fluctuations. For this analysis, $n = 20$, to comply with the constraints of computing resources i.e. length of processing time and distribution of data files on disk.

Effects from multiplicity fluctuations were minimized by dividing events to be mixed into nine raw multiplicity classes (corresponding to the nine centrality classes 0-5%, 5-10%, 10-20%, 20-30%, 30-40%, 40-50%, 50-60%, 60-70%, 70-80%) and only mixing events within the same class.

In order to minimize distortions due to acceptance effects, within each centrality class, the events were further sub-divided into 10(6) bins according to $z$-vertex position and mixed within those bins for the spectral($v_2$) analysis. The final *mixed-event* distribution for each centrality class was found by adding up all the $m_{inv}$ distributions from each $z$-vertex bin.

### 3.3.2 Extracting the raw yields

Since the mixed-event background distributions are constructed by mixing a large number of events, they need to be scaled first before being subtracted from the signal distributions. The scaling was performed in two different ways to study the sensitivity of the scaling on the final extracted yields:

1. **Scaling by the integral ratio:**
   The background distribution was scaled by the ratio of the integrals of the signal and the background distributions in a fixed mass region away from the $\phi$ mass peak ($1.04 < m_{inv} < 1.06$ GeV/$c^2$).

2. **Scaling interatively:**
   The background distribution was scaled by the ratio of the integral of the signal to the integral of the background distribution in a fixed invariant mass region including the $\phi$ mass peak ($0.99 < m_{inv} < 1.05$ GeV/$c^2$). The background distribution was then subtracted from the signal distribution and the remaining signal was fitted with a Breit-Wigner function plus a straight line. The signal integral was then set to be the integral in the mass range minus the integral of the Breit-Wigner function, the ratio was recalculated and the background rescaled. Four iterations were needed to stabilise the final scaling factor.

The raw $\phi$-meson yields are extracted as a function of centrality by subtracting the scaled mixed-event background distributions from the signal distributions. After subtraction, the remaining distribution consists of the $\phi$ mass peak signal plus some residual background. This distribution is fitted with a Breit-Wigner function ($BW(m_{inv})$):

$$BW(m_{inv}) = \frac{1}{2\pi}\frac{A\Gamma}{(m - m_{\phi})^2 + (\Gamma/2)^2} \tag{3.1}$$

(where $A$ is the area of the distribution and $\Gamma$ is the width) to describe the shape of the $\phi$ mass peak plus a polynomial function (usually a straight line), to describe the residual background. The minimum bias raw background-subtracted $m_{inv}$ distributions in various $p_T$ bins are presented in Fig. 3.3. To see the $m_{inv}$ distributions before and after background subtraction for other centrality bins, refer to Appendix C. The experimentally measured values of the $\phi$ mass and width are consistent, within the experimental resolution, with the particle data group (PDG) values [53].

Although the mixed event background gives a good estimation of the combinatorial background due to uncorrelated kaon pairs, there are also con-

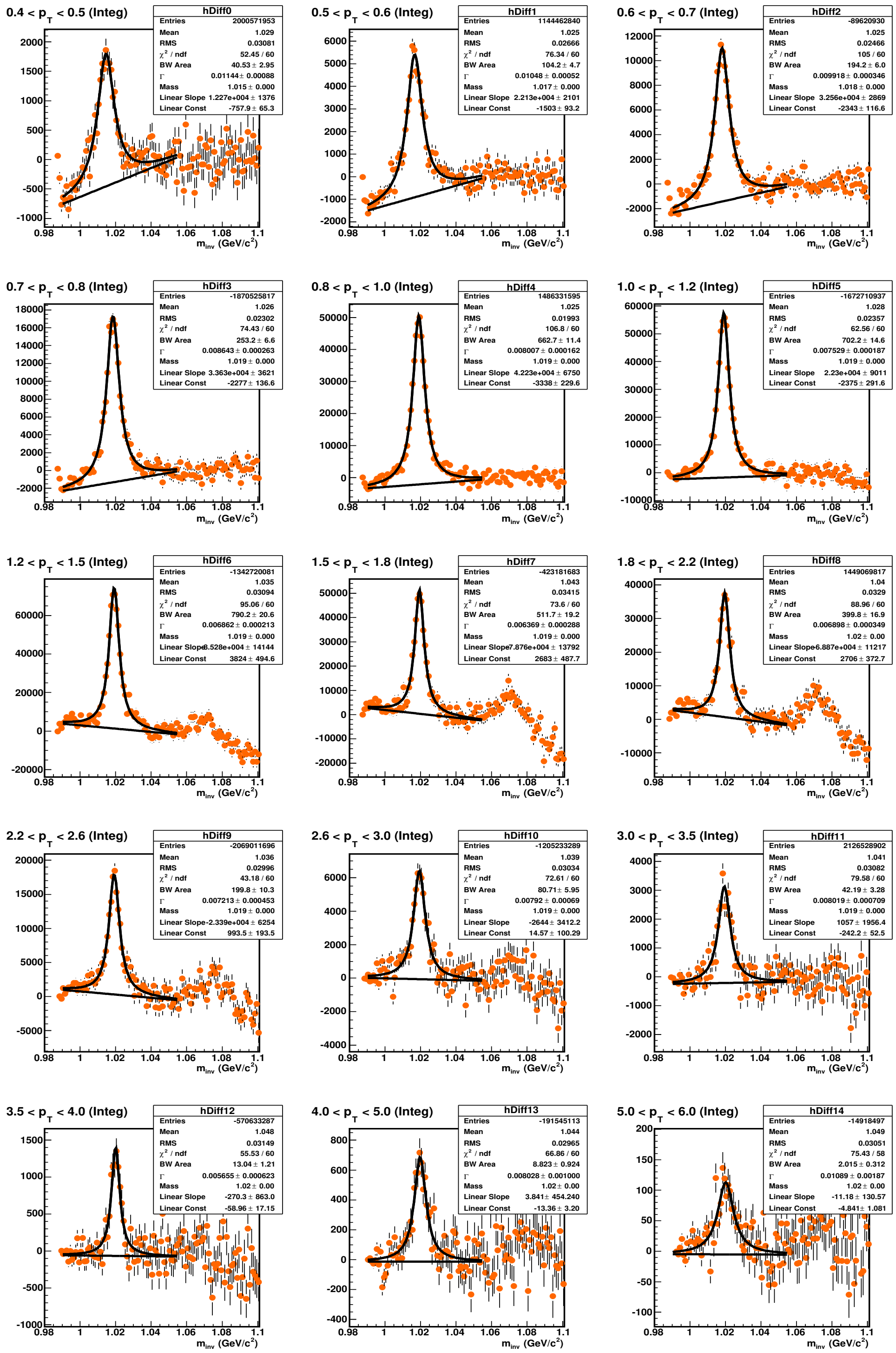

**Figure 3.3**: Details of the fits to the $m_{inv}$ distributions after subtraction of the mixed-event background, as a function of $p_T$ for 0-80% data.

tributions to the background from real resonance decays where the daughter particles are misidentified as kaons in the TPC. This contributes to the residual background remaining after the subtraction of mixed events. Figure 3.1 shows that at low momentum, the $dE/dx$ bands for charged particles are clearly separated and particles can be cleanly identified. However, as the momentum increases, the bands start to overlap and therefore the $2\sigma$ cut imposed for kaon identification also allows a fraction of electrons, pions and protons to be included as kaon candidates in the signal distribution. Therefore, for example, if both pions from a $K^0_S$ decay are misidentified as kaons, they will contribute to a true $K^0_S$ mass peak which will be shifted from its proper position in $m_{inv}$ due to the incorrect mass being attributed to the pions.

To study where in the $m_{inv}$ continuum these shifted peaks would appear, a simple simulation was performed. Various particles were decayed in their rest frames

$$\begin{array}{rcll} \rho & \rightarrow & \pi\pi & \text{(B.R.} \sim 100\%) \\ K^0_S & \rightarrow & \pi^+\pi^- & \text{(B.R.} = 69.20\%) \\ K^* & \rightarrow & K\pi & \text{(B.R.} \sim 100\%) \end{array}$$

and then boosted according to randomly sampled $p_T$ distributions with an $m_T$ exponential shape and an inverse slope parameter $T = 350$ MeV. The daughter particles were then all assumed to have the mass of a charged kaon and the $m_{inv}$ distributions of the parent particles were recalculated based on this assumption. To check the effects on the reconstructed $m_{inv}$ distributions due to imperfect momentum resolution in the TPC, a 5% gaussian smearing was applied to the daughter particles' $p_T$. The positions of the shifted mass peaks (with and without momentum smearing) for the $K^0_S$ and the $K^*$ are presented in Fig. 3.4. (The position of the 'fake' $\rho$ peak is shifted well above ( 1.2 GeV/$c^2$) the $\phi$ mass peak position and is not shown.) The simulation was not used to quantify the yield in these 'fake' mass peaks, but rather to identify their origin in the case that they were seen in the real data analysis.

Therefore, the "bump" observed to the right of the $\phi$ mass peak in the higher $p_T$ bins in Fig. 3.3 is likely due to contributions from the $K^0_S$ and

$K^*$ decay daughters being incorrectly identified. From the positions of these 'fake' mass peaks, (even including momentum smearing) with respect to the position of the $\phi$ mass peak (indicated by the dashed line and grey shading), any contribution from them to the extracted raw phi yield is expected to be negligible.

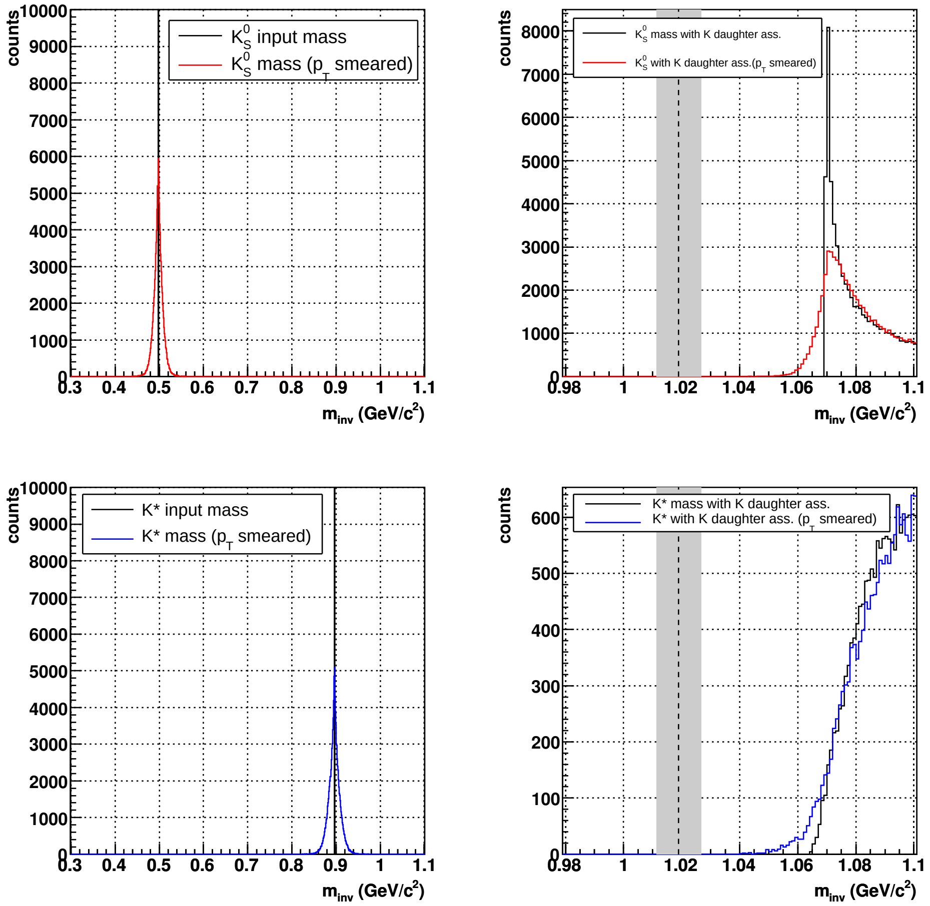


**Figure 3.4**: **Left column:** Input mass peak position for the $K_S^0$ (upper panel) and $K^*$ (lower panel), with (coloured histogram) and without (black line) momentum smearing applied. **Right column:** Positions of mass peaks for $K_S^0$ (upper panel) and $K^*$ (lower panel), with charged $K$ mass assumption for both decay daughters with (coloured histogram) and without (black histogram) momentum smearing. The dashed line and shaded area indicate the PDG mass peak position and the mean experimentally reconstructed width, $\Gamma$, of the $\phi$ (integrated over the full measured $p_T$ range for minimum bias collisions).

The contribution from all other resonances to this residual background cannot be calculated and therefore the effect is estimated by fitting the residual background shape after mixed-event background subtraction with various polynomial functions to estimate the effect on the extracted raw yields.

### 3.3.3 Efficiency and Acceptance Corrections

After the raw $\phi$ yields have been extracted, they need to be corrected for detector acceptance and tracking inefficiencies. Although the STAR TPC has a full $2\pi$ azimuthal acceptance, there are gaps between the TPC sectors for example, which cause some loss of particle identification and measurement. In addition, the TPC tracking efficiency declines as a function of increased charged track multiplicity i.e. for more central collisions. The tracking efficiency is also an inverse function of momentum since high momentum particles have almost straight trajectories in the 0.5 T magnetic field and it is therefore more difficult to reconstruct the momenta of these particles than for the low momentum tracks which have significant curvature.

These effects are corrected for by comparing to simulations. Monte Carlo (MC) simulated $\phi$-mesons are embedded in real data events and all are decayed to charged kaons. These embedding events are then processed through the same full STAR reconstruction process as real events. The MC $\phi$ decay daughter kaons are subjected to the same cuts that are applied in the real data analysis. A $\phi$ is counted as being reconstructed if both its decay daughters are reconstructed by the tracking software, and in addition, pass all analysis and acceptance cuts. The ratio of the reconstructed $\phi$-mesons to the input $\phi$-mesons is therefore the efficiency$\times$acceptance factor by which the raw data results need to be divided to obtain the true yields.

As the first step in reconstructing the input $\phi$-mesons, we need to identify the reconstructed primary tracks (i.e. tracks originating from the collision vertex) which are *associated* with or *matched* to the input Monte Carlo kaons in the embedding events. As a first level filter to eradicate associations which are very unlikely, a cut is imposed on the number of common hit points in the TPC between reconstructed tracks and the input track. For this analysis the standard cut of 10 common hit points was applied. Usually this cut results in a single reconstructed track being associated with an input MC track. However, sometimes ($\sim$2% of the time in central events) more than one reconstructed track fulfills the 10 common hits criterion and in that case more than one reconstructed track is associated with a single MC track. This effect is centrality dependent since it is more difficult to reconstruct tracks in higher multiplicity (i.e. more central) events than in events with low track multiplicities due to the larger combinatorics. However, in the case of more than one reconstructed track being associated with an input MC track, it is very important to identify the track that is most likely to be the true associated track since misidentification can lead to incorrect reconstructed $\phi$ $p_T$ distributions and therefore incorrect efficiency$\times$acceptance calculations. This effect is illustrated in Fig. 3.5 for 0-10% most central events. In both panels of Fig. 3.5, the $p_T$ of the input MC $\phi$ is plotted vs. the reconstructed $\phi$-meson $p_T$. The left panel shows the distribution where, if there is more than one associated reconstructed track for a single MC kaon, one of them is chosen at random to calculate the $p_T$ of the reconstructed parent $\phi$-meson. This leads to a large smearing of the reconstructed $\phi$ $p_T$ to lower values than were input which will in turn lead to a change in the shape of the calculated efficiency$\times$acceptance as a function of $p_T$.

Identification of the most likely associated track candidate is performed by choosing the associated primary track with the highest number of common hits. The resulting $p_T$ correlation graph is shown in the right hand panel of Fig. 3.5. Compared to the left hand panel, the right hand plot shows a much clearer correlation between the input $\phi$ $p_T$ and the reconstructed $p_T$ indicating that the true reconstructed kaon candidate was used to reconstruct the parent $\phi$ momentum. The broadening of the correlation at higher $p_T$ is due to real tracking momentum resolution effects.

Using the flat input $\phi$ $p_T$ distribution and choosing the most likely reconstructed candidates for the daughter kaons, results in the reconstructed $\phi$-meson $p_T$ distribution and efficiency$\times$acceptance distribution for 0-80% minimum bias events presented in Fig. 3.6.

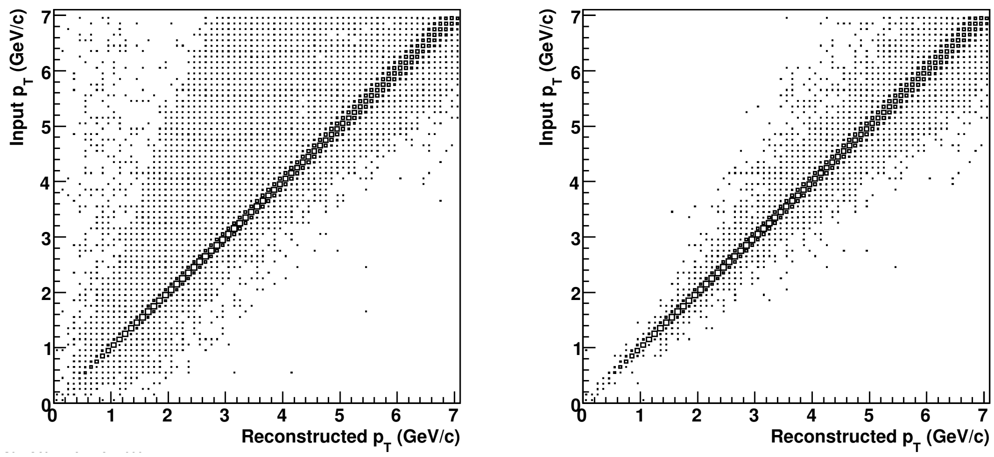


**Figure 3.5**: Input MC $\phi$-meson $p_T$ vs. reconstructed $\phi$-meson $p_T$ for (left plot) no distinction made between multiple associated candidate tracks, one is simply chosen at random, compared to the case (right plot) where the most likely associated track candidate is chosen on the basis of most common hits. Both panels are for 0-10% central events at $\sqrt{s_{NN}} = 200$ GeV.

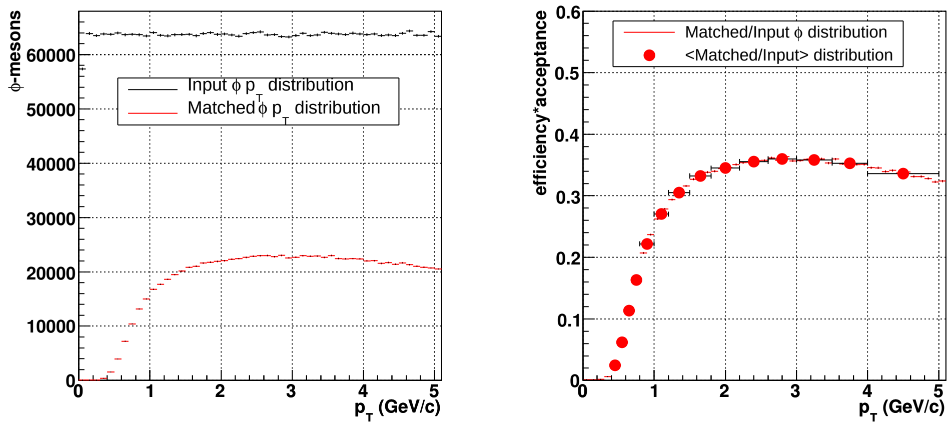


**Figure 3.6**: **Left:** Flat input $p_T$ distribution of $\phi$-mesons (in black) compared to the distribution of $\phi$-mesons which passed all analysis cuts (in red). **Right:** Efficiency$\times$acceptance as a function of $p_T$ calculated as the ratio of the number of reconstructed over input $\phi$-mesons. (Embedding events for minimum bias (0-80%) Au+Au at $\sqrt{s_{NN}} = 200$ GeV.)

### 3.3.4 Momentum smearing effects

The simulated $\phi$-meson $p_T$ distributions for embedding were thrown flat as a function of $p_T$, see Figure 3.6. In this case, all $p_T$ bins have an approximately equal number of entries and equal weighting. The advantage of this procedure is that the statistics in all $p_T$ bins are approximately the same and therefore the statistical errors introduced by the efficiency$\times$acceptance correction will be constant as a function of $p_T$. However, effects from momentum smearing (i.e. the momentum of an input track being reconstructed higher or lower than its true value) will not be evident using this input shape. The $\phi$-meson $p_T$ distributions (after correction using the flat efficiency correction factors) can be described by exponential functions in transverse mass, $m_T$, and an inverse slope parameter, $T$. To study the additional effect of momentum smearing on the reconstructed $p_T$ distributions, the input $p_T$ distributions were weighted to be similar in shape to real events as:

$$\frac{dN}{dp_T} = \frac{p_T}{T(m_0 + T)} e^{-\frac{m_T - m_0}{T}} \tag{3.2}$$

where $m_T = \sqrt{m_0^2 + p_T^2}$ and the slope parameter $T = 350$ MeV (shown by the black histogram in the left-hand panel of Fig. 3.7). The reconstructed $\phi$-meson $p_T$ values were then filled into a histogram in $p_T$, weighted according to their input $p_T$ values (shown by the green histogram in the left panel of Fig. 3.7). The resulting efficiency$\times$acceptance as a function of $p_T$ using the weighting method is shown in the right-hand panel of Figure 3.7. Another way to calculate the efficiency using a realistic input $p_T$ distribution shape, is to sample the flat input $p_T$ distribution and eliminate particles according to the same exponential function. The disadvantage with this method is that the embedding statistics are reduced in the higher $p_T$ bins resulting in larger statistical errors in the efficiency$\times$acceptance calculation compared to the result from using the weighting method. Therefore, for this analysis, the weighting method was used and the resulting efficiency$\times$acceptance result for 0-80% minimum bias events is presented in Fig. 3.7.

Figure 3.8 compares the efficiency$\times$acceptance results for the flat input $p_T$ distribution and the weighted input $p_T$ distribution. The effect of momentum

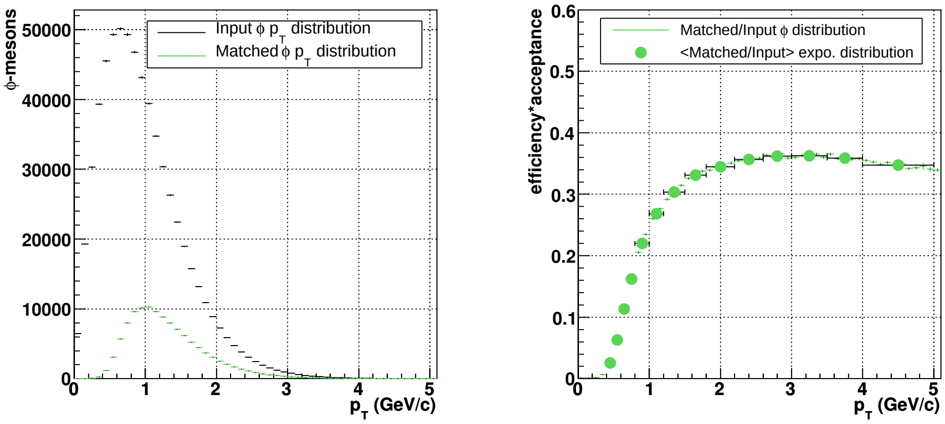


**Figure 3.7**: **Left:** Weighted input $\phi$-meson $p_T$ distribution (in black) compared to weighted distribution of $\phi$-mesons which passed all analysis cuts (in green). **Right:** Efficiency$\times$acceptance as a function of $p_T$ calculated as the ratio of the number of reconstructed over input $\phi$-mesons. (Embedding events for minimum bias (0-80%) Au+Au at $\sqrt{s_{NN}}$ = 200 GeV.)

smearing is seen to shift the efficiency$\times$acceptance lower at low $p_T$, with an increase at the lowest $p_T$, and higher at high $p_T$ for the weighted case than the values obtained using the flat input $p_T$ distribution.

The weighted efficiency$\times$acceptance values vs. $p_T$ are presented as a function of centrality in Fig. 3.9. The efficiency is lowest for most central collisions ($\sim$0.3 at $p_T$ = 2 GeV/$c$ for 0-5% central collisions) and improves with decreasing centrality ($\sim$0.37 at $p_T$ = 2 GeV/$c$ for 70-80% central collisions).

### 3.3.5 Systematic error analysis

The main sources of systematic error in extracting the raw $\phi$-meson yields are listed below:

- **Uncertainty in background shape:**
  The uncertainty in the raw $\phi$ yield from uncertainty in the shape of

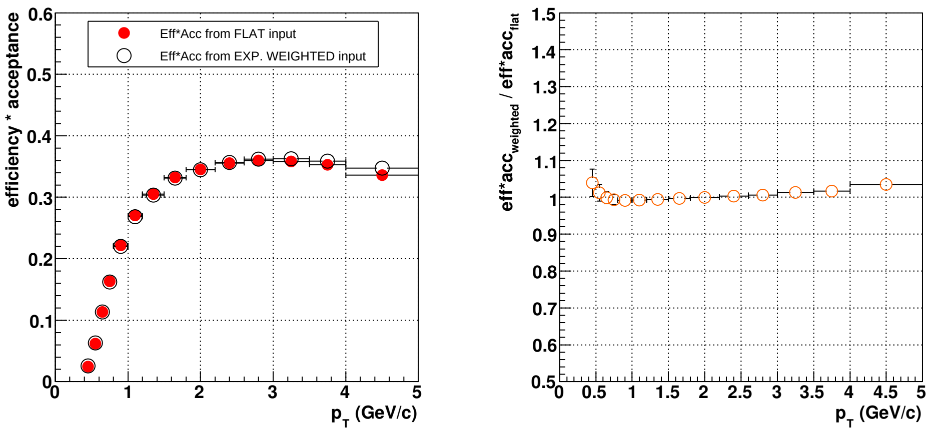


**Figure 3.8**: **Left:** Comparison of efficiency×acceptance results when using the flat input $p_T$ distribution (solid symbols) and when using a weighted input $p_T$ distribution (open symbols). **Right:** Ratio of the $p_T$-weighted efficiency×acceptance result to the flat result as a function of $p_T$. (Embedding events for minimum bias (0-80%) Au+Au at $\sqrt{s_{NN}}$ = 200 GeV.)

the combinatorial background was estimated by using each of the background normalization techniques described in section 3.3.2 and studying the difference in the final extracted raw yields.

- **Uncertainty in residual background shape:**
  The shape of the residual background remaining after the mixed-event subtraction varies as a function of $p_T$. This is mainly due to the $p_T$ dependence of the contamination of the kaon sample from misidentification of $\pi$ and $p$ due to the overlap of the $dE/dx$ bands as a function of $p_T$. The effect was estimated using two steps:

  – Varying the fit function to describe the residual background by using a straight line vs. second order polynomial function

  – Varying the fitting range in $m_{inv}$ for the $\phi$ mass peak.

- **Uncertainty from particle identification using $dE/dx$ measurements:**
  This uncertainty was estimated by using different $n\sigma$ cuts for the kaon candidates, and comparing the resulting yields after adjustment for the corresponding $1\sigma$, $2\sigma$ and $3\sigma$ particle identification efficiencies.

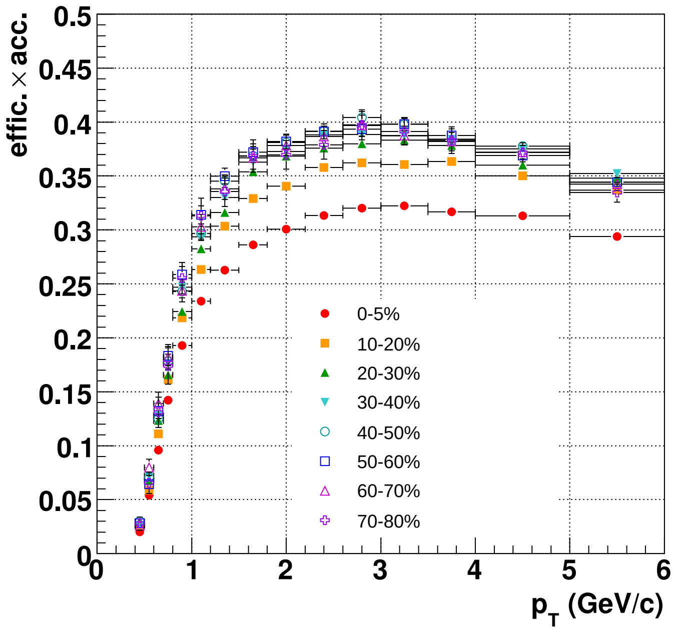


**Figure 3.9**: Efficiency×acceptance vs. $p_T$ for the $\phi$-meson as a function of centrality for Au+Au collisions at $\sqrt{s_{NN}} = 200$ GeV.

## 3.4 Elliptic flow

In relativistic heavy-ion collisions, the azimuthal distributions of particles can be described using a Fourier expansion in terms of the particle emission azimuthal angle measured with respect to the reaction plane in the collision [42] as:

$$E\frac{d^3N}{d^3p} = \frac{1}{2\pi}\frac{d^2N}{p_T dp_T dy}(1 + \sum_{n=1}^{\infty} 2v_n \cos(n(\phi - \Psi_r))). \tag{3.3}$$

The first two Fourier coefficients together are called anisotropic flow where the coefficient $v_1$ is called *directed flow* and $v_2$ is known as *elliptic flow* because in polar coordinates, for small values of $v_2$, the azimuthal distribution with non-zero second harmonic describes an ellipse. (When $v_2$ is large, the distribution appears dumbbell-shaped.) The Fourier coefficients can also be written as $v_n = \langle(\cos(n(\phi - \Psi_r))\rangle$ where the average is taken over all particles in all events [42].

In order to measure the elliptic flow as described, the reaction plane angle, $\Psi_r$, (which is unknown) has to be estimated on an event-by-event basis. The estimated reaction plane is usually called the event plane. We follow the method and equations derived in [42] which uses the anisotropic flow itself to determine the event plane. The event plane angle can be calculated in terms of the event flow vector $Q_n$ defined as:

$$Q_n \cos(n\Psi_n) = \sum_i w_i \cos(n\phi_i), \tag{3.4}$$

$$Q_n \sin(n\Psi_n) = \sum_i w_i \sin(n\phi_i), \tag{3.5}$$

where $w_i$ are weights and $i$ is the number of particles used in the determination of the event plane. The event plane angle can then be calculated for each harmonic as:

$$\Psi_n = \left(\tan^{-1} \frac{\sum_i w_i \sin(n\phi_i)}{\sum_i w_i \cos n\phi_i}\right)/n. \tag{3.6}$$

For this analysis, the weighting was done such that $w_i = p_{Ti} \times w_\phi$. The $\phi$-weight factor, $w_\phi$, was necessary to correct for detector acceptance effects which can lead to anisotropic particle distributions in the lab frame which are not due to anisotropic flow. Therefore it is necessary to ensure that the event plane angle distribution over all events is isotropic (i.e. flat with respect to azimuthal angle $\phi$). This was achieved by finding the azimuthal distribution of all particles to be used in the event plane determination over many events and taking the inverse (per $\phi$ bin) as the correction factor $w_\phi$. The raw distributions for an arbitrary centrality bin are shown in Fig. 3.10. It was important to perform the correction for the positive and negative $\eta$ regions separately since the acceptance in the STAR TPC was different in the two acceptance regions for Run IV. This is illustrated by the larger dip in the weighting distribution between $-1 < \phi < 0$ in the negative $\eta$ region (left panel of Fig. 3.10) due to a bad TPC sector.

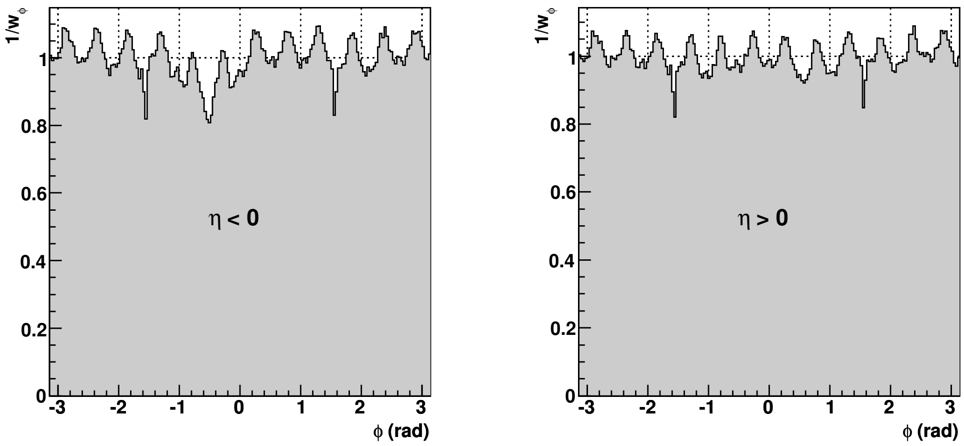


**Figure 3.10**: Distributions of charged particles used in determining the event plane, for negative (left panel) and positive (right panel) pseudorapidity $\eta$ in the STAR TPC.

In order to minimize the contribution to the event plane determination from effects and phenomena which are not necessarily correlated with the event plane, called non-flow effects, for example jets, only particles with $p_T \leq 2$ GeV/$c$ were used in the calculation. In addition, to eliminate self-correlations between kaons which are both used in the event plane calculation and to reconstruct $\phi$-mesons (and therefore the angle between the reconstructed $\phi$-meson and the event plane), all charged kaons, identified according to the criteria in Table 3.2, were excluded from the event plane calculation.

Figure 3.11 shows the resulting flat event plane angle distribution after all weighting and corrections for the 200 GeV minimum bias dataset.

### 3.4.1 Event plane resolution correction

The finite number of particles in an event, which are available for calculating the event plane, leads to a limited resolution in the measured event plane

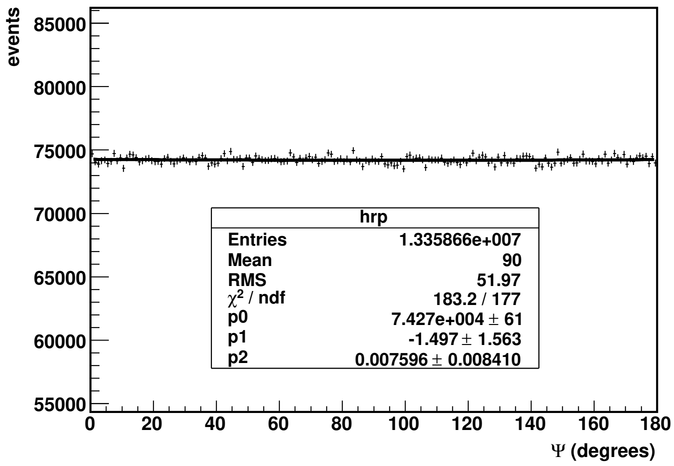


**Figure 3.11**: Distribution of event plane angles for the 200 GeV dataset calculated as described in the text. The solid line indicates a second order polynomial fit to the data where the first and second order parameters are consistent with zero i.e. the distribution is flat.

angle. Therefore, to find the actual $v_n$ with respect to the real reaction plane, the measured $v_n$ is divided by a resolution correction factor. From [42], the event plane resolution for $v_2$, using the second harmonic event plane $\Psi_2$, can be expressed as:

$$\langle\cos(2(\Psi_2 - \Psi_r))\rangle = \frac{\sqrt{\pi}}{2\sqrt{2}}\chi_2 \exp(-\chi_2^2/4)\left[I_0(\chi_2^2/4) + I_1(\chi_2^2/4)\right], \tag{3.7}$$

where $I_{0(1)}$ is the modified Bessel function of order 0(1) and

$$\chi_2 \equiv \frac{v_2}{\sigma} \quad \text{and} \quad \sigma^2 = \frac{1}{2N}\frac{\langle w^2\rangle}{\langle w\rangle^2}, \tag{3.8}$$

where $N$ is the number of particles used to calculate the event plane angle and $w$ are the weights discussed previously.

The resolution can be estimated using the correlation of the event planes calculated using independent sub-events. For this analysis, the sub-events were constructed by randomly dividing particles (which satisfy the conditions to be used in the event plane calculation) into two groups. Since the multiplicity of each sub-event $a$ and $b$ should be approximately the same and their respective resolutions should be equal, the resolution of each is given by:

$$\langle \cos(2(\Psi_2^a - \Psi_r)) \rangle = \sqrt{\langle \cos(2(\Psi_2^a - \Psi_2^b)) \rangle}. \tag{3.9}$$

Equations 3.9 and 3.7 can then be used to calculate the full event plane resolution, taking into account that the full event has twice as many particles as the sub-events (i.e. in equation 3.7, $\chi_2$ needs to be multiplied by a factor of $\sqrt{2}$).

Since the event plane resolution is dependent on the number of particles used in the calculation, it varies as a function of centrality and degrades with more peripheral collisions. Also, since the event plane is calculated using the anisotropic flow of the event itself, for more central collisions the resolution also becomes poorer since the shape of the distribution becomes less elliptical. In this analysis, the event plane resolution was calculated for each centrality bin within the minimum bias dataset (0-5%, 5-10%, 10-20%, 20-30%, 30-40%, 40-50%, 50-60%, 60-70%, 70-80%) individually. In the case of combined centrality bins, for example minimum bias (0-80%), the combined resolution was calculated as the raw-yield-weighted average of the resolutions. Figure 3.12 shows the variation with centrality of the event plane resolution calculated as described for the 200 GeV minimum bias dataset.

A summary of the averaged resolution correction factors for the different centrality bins and datasets studied is shown in Table 3.3. (Note that the resolution correction factor presented in Table 3.3 for 0-5% centrality is calculated using the central-triggered dataset, not the minimum bias dataset, to correspond with the 0-5% $v_2$ results which were extracted from the central-triggered dataset.)

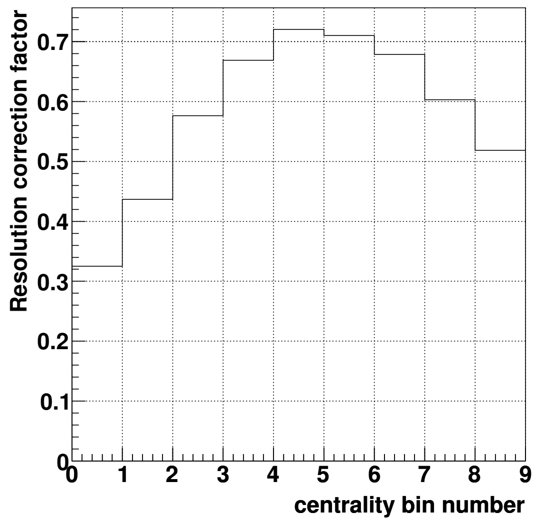


**Figure 3.12**: Event plane resolution correction factors vs. centrality bin for Au+Au collisions at $\sqrt{s_{NN}}$ = 200 GeV. The numbers 1-9 correspond to 70-80% - 0-5% central respectively.

| Centrality range | Resolution |
|---|---|
| **200 GeV** | |
| 0-5 % | 0.493 |
| 10-40 % | 0.697 |
| 40-80 % | 0.588 |
| 0-80 % | 0.629 |
| **62.4 GeV** | |
| 0-80 % | 0.601 |

**Table 3.3**: Summary of the averaged event plane resolution correction factors for each centrality bin and dataset studied. Note that the 0-5% resolution correction factor was calculated from the central-triggered 200 GeV dataset. All other factors were calculated from the minimum bias datasets for the respective energies.

### 3.4.2 Extracting the $\phi$-meson elliptic flow

Two variations of the event plane method (here called the *$\phi$-binning method* [42] and the *$v_2$ vs. $m_{inv}$ method* [81]) were used to extract the $\phi$-

meson elliptic flow, $v_2(p_T)$. The $v_2$ vs. $m_{inv}$ method is the newer of the two methods and the results using this method are presented in Chapter 4. Since this analysis was among the first to use the $v_2$ vs. $m_{inv}$ method, cross-checks of results were performed using the $\phi$-binning method in order to test the applicability of the new method. The details of each method are outlined in the following sections.

### The $\phi$-binning method

The $\phi$-binning method for extracting the $v_2$ of identified particles consists of measuring the raw yield of the chosen particle in bins of the angle ($\phi$-$\Psi$) where $\phi$ is the azimuthal angle of the particle in the lab-frame and $\Psi$ is the event plane angle. The distribution can then be fitted with the functional form:

$$\frac{dN}{d(\phi - \Psi)} = P_0 \left(1 + 2v_2 \cos(2(\phi - \Psi))\right) \tag{3.10}$$

where $v_2$ is one of the fit parameters. The $p_T$ dependence of the elliptic flow can be measured by repeating the procedure for fixed ranges in $p_T$. The measured $v_2$ values must be divided by the appropriate event plane resolution correction factor to obtain the final $v_2$ values. Figure. 3.13 illustrates the method for the 62.4 GeV dataset.

For the case of resonances, where the signal typically consists of a small particle mass peak sitting above a large combinatorial background (i.e. the signal to background ratio is less than unity), it is already a difficult task to extract raw yields accurately. This method of extracting $v_2$ requires that, for each bin in $p_T$, the already small signal is further divided into bins as a function of ($\phi$-$\Psi$) angle which can lead to large systematic errors in extracting the raw yields since the fits to the invariant mass peak are difficult to constrain. The result is that large systematic errors, due to uncertainties in the raw yields, are propagated into the final $v_2$ result. For this reason, the method described in the following section was used to extract the presented

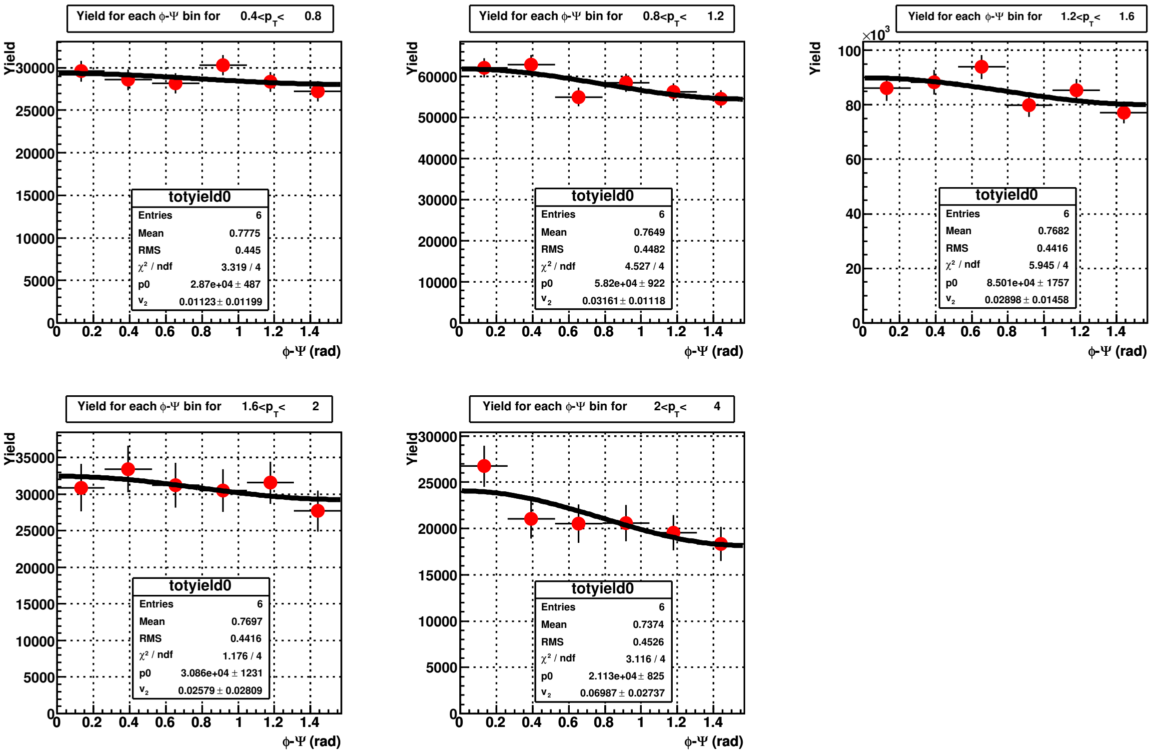


**Figure 3.13**: Fits using equation 3.10 to the raw $\phi$-meson yields as a function of $(\phi - \Psi)$ angle for 5 bins in $p_T$ for 0-80% central Au+Au collisions at $\sqrt{s_{NN}} = 62.4$ GeV.

$\phi$-meson $v_2$ results.

### The $v_2$ vs. $m_{inv}$ method

The $v_2$ vs. $m_{inv}$ method was inspired by [81] and a brief description of the phenomenology is outlined below. For single particles, in the laboratory frame, the probability distribution in terms of the azimuthal angle $\phi$ can be written as:

$$p(\phi - \Psi_r) = \frac{1}{2\pi} \sum_{n=-\infty}^{+\infty} v_n e^{in(\phi - \Psi_r)} \tag{3.11}$$

where $\phi$ is the angle of the particle measured in the laboratory frame and $\Psi_r$ is the reaction plane angle. In the case of a symmetric system with real $v_n$, equation 3.11 reduces to:

$$p(\phi - \Psi_r) = \frac{1}{2\pi}\left[1 + 2\sum_{n=1}^{\infty} v_n \cos n(\phi - \Psi_r)\right] \tag{3.12}$$

which is just the probability analogue of equation 3.3. Following [81], equation 3.11 can be extended for pairs of particles as:

$$p(\phi_{\text{pair}} - \Psi_r) = \frac{1}{2\pi}\sum_{n=-\infty}^{+\infty} v_n^{\text{pair}} e^{in(\phi_{\text{pair}} - \Psi_r)} \tag{3.13}$$

where $\phi$ has been replaced with $\phi_{\text{pair}}$. In the case of a resonance particle (e.g. the $\phi$-meson) which decays to two daughter particles (e.g. $\phi \to K^+K^-$), $\phi_{\text{pair}}$ is the azimuthal angle of the parent resonance particle.

In equation 3.13, $v_n^{\text{pair}}$ are called the "pair-flow" coefficients, but unlike in the previous case of single particles, $v_n^{\text{pair}}$ are not necessarily real numbers with the result that the sine terms become part of the Fourier expansion such that:

$$p(\phi - \Psi_r) = \frac{1}{2\pi}\left[1 + 2\sum_{n=1}^{\infty}\left(v_{c,n}^{\text{pair}} \cos n(\phi_{\text{pair}} - \Psi_r) + v_{s,n}^{\text{pair}} \sin n(\phi_{\text{pair}} - \Psi_r)\right)\right] \tag{3.14}$$

where $v_{c,n}^{\text{pair}} = \langle \cos n(\phi_{\text{pair}} - \Psi_r)\rangle$ and $v_{s,n}^{\text{pair}} = \langle \sin n(\phi_{\text{pair}} - \Psi_r)\rangle$.

For a resonance particle which is identified through its mass peak in an invariant mass distribution consisting of all combinations of candidate decay daughter particle pairs, the invariant mass distribution can be separated into:

$$N_{\text{pairs}}(m_{inv}) = N_b(m_{inv}) + N_s(m_{inv}) \tag{3.15}$$

where $N_b$ is the number of combinatorial background pairs and $N_s$ is the number of signal pairs (i.e. the number of real particles). In a similar way, for the $\phi$-meson, we can write the contributions to the pair-flow coefficients as:

$$N_{\text{pairs}}(m_{inv})v_{c,n}(m_{inv}) = N_b(m_{inv})v^b_{c,n}(m_{inv}) + N_{\phi,n}(m_{inv})v^{\phi}_{c,n} \tag{3.16}$$
$$N_{\text{pairs}}(m_{inv})v_{s,n}(m_{inv}) = N_b(m_{inv})v^b_{s,n}(m_{inv}) + N_{\phi,n}(m_{inv})v^{\phi}_{s,n}. \tag{3.17}$$

Symmetry of $\phi$-mesons with respect to the reaction plane implies that $v^{\phi}_{s,n} = 0$ and if the background is composed of uncorrelated particles, then $v^b_{s,n} = 0$ [81].

Experimentally, the $v_2$ vs. $m_{inv}$ method as it is applied here, involves estimating the event plane angle the same way as before and then measuring the $v_2 = \langle \cos 2(\phi - \Psi) \rangle$ of all same-event combinations of positive and negative kaon pairs as a function of invariant mass. To correct for the finite event plane resolution, the distribution is scaled by the appropriate factor (as presented in Table 3.3). Based on equation 3.16, the $v_2$ distribution as a function of $m_{inv}$ can then be fitted using:

$$v_{2Tot}(m_{inv}) = v_{2S}\alpha(m_{inv}) + v_{2B}(m_{inv})[1 - \alpha(m_{inv})] \tag{3.18}$$

where $v_{2Tot}$ is the total $v_2$, $v_{2S}$ is the $v_2$ of the signal (i.e. the $\phi$-meson), and $v_{2B}$ is the background $v_2$. $\alpha(m_{inv}) = S/(S + B)$ which is ratio of the signal over the sum of the signal plus background $m_{inv}$ distributions.

The ratios are functions of invariant mass and are extracted (once only per $p_T$ bin) by fitting the signal distribution, after mixed-event background subtraction, using a Breit-Wigner function (to describe the $\phi$-meson mass peak shape) plus a polynomial (to parameterize the background shape). (Examples of the ratios for a particular bin in $p_T$ for the 62.4 GeV minbias data are

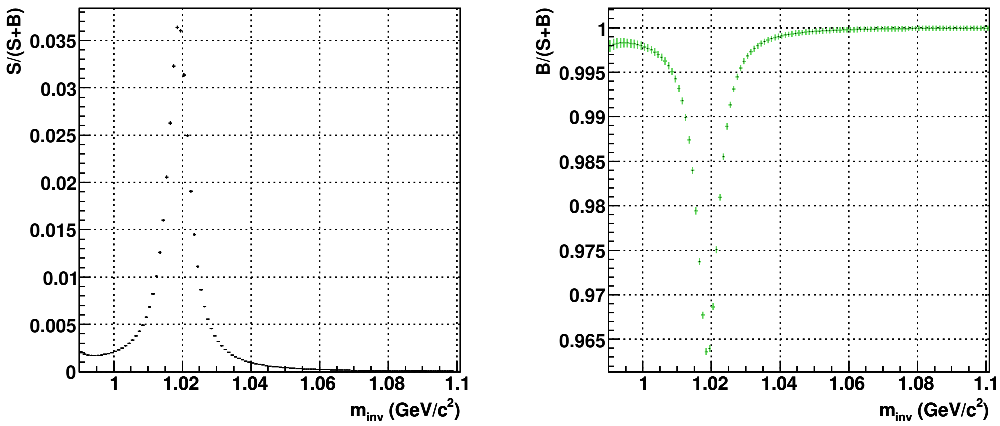


**Figure 3.14**: $S/(S{+}B)$ (left panel) and $B/(S{+}B)$ (right panel) ratios calculated from the result of the fitting function (described in the text) for $0.8 < p_T < 1.2$ GeV/$c$ for minimum bias Au+Au collisions at $\sqrt{s_{NN}} = 62.4$ GeV.

presented in Fig. 3.14). Therefore, in this method, the raw yield of $\phi$-mesons needs to be extracted once per $p_T$ bin. $v_{2S}$ is a parameter in the fit and $v_{2B}$ is parameterised using a polynomial in $m_{inv}$. The order of the polynomial was allowed to change as a function of $p_T$ in order to optimize the $\chi^2$/ndf of the fit.

In order to check the validity of the $v_2$ results obtained using this method, the $v_{s,2} = \langle \sin 2(\phi - \Psi) \rangle$ distributions can be measured and fitted in a similar manner to ensure that the expected identities, $v^b_{s,2} = 0$ and $v^\phi_{s,2} = 0$, hold. Figure 3.15 illustrates the method by presenting the fits to the $v_2 = \langle \cos 2(\phi - \Psi) \rangle$ (left panel) and $v_{s,2} = \langle \sin 2(\phi - \Psi) \rangle$ (right panel) distributions for a bin in $p_T$ for minimum bias Au+Au collisions at $\sqrt{s_{NN}} = 62.4$ GeV. The right panel illustrates the identity, $v^\phi_{s,2} = 0$.

### $v_2$ Method comparison

The 62.4 GeV dataset was used as proof of principle for the $v_2$ vs. $m_{inv}$ method. The raw $v_2(p_T)$ results for the 62.4 GeV minimum bias dataset are

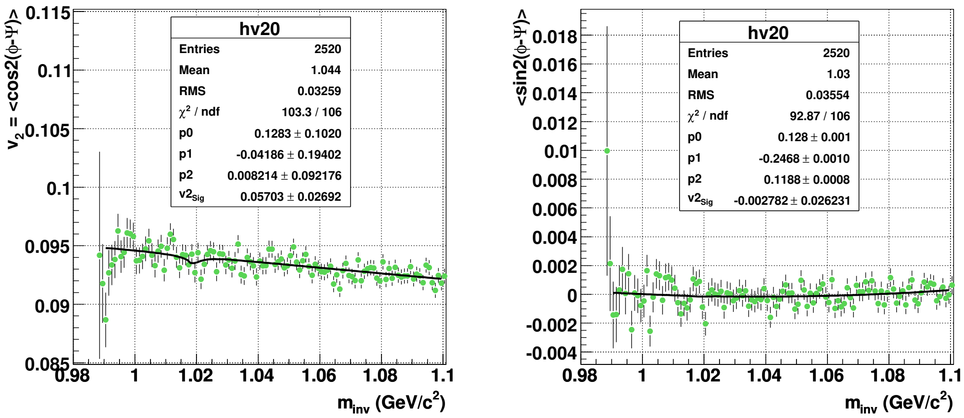


**Figure 3.15**: Fits to the $v_2 = \langle \cos 2(\phi - \Psi) \rangle$ (left panel) and $v_{s,2} = \langle \sin 2(\phi - \Psi) \rangle$ (right panel) distributions for $2.0 < p_T < 4.0$ GeV/$c$ for minimum bias Au+Au collisions at $\sqrt{s_{NN}} = 62.4$ GeV.

presented in Table. 3.4. (Figure B.1 in Appendix B.1 presents the comparison graphically.) The results from the $\phi$-binning method and $v_2$ vs. $m_{inv}$ method are consistent within the statistical uncertainties. The systematic errors on each method are not estimated here. All results presented in the following sections have been extracted using the $v_2$ vs. $m_{inv}$ method.

| $p_T$ **bin** (GeV/$c$) | $v_2$ ± **(stat. err.)** ($\phi$-binning method) | $v_2$ ± **stat. err.** (vs. $m_{inv}$ method) |
|---|---|---|
| 0.4< $p_T$ <0.8 | 0.011 ± 0.012 | 0.010 ± 0.011 |
| 0.8< $p_T$ <1.2 | 0.032 ± 0.011 | 0.055 ± 0.010 |
| 1.2< $p_T$ <1.6 | 0.029 ± 0.015 | 0.046 ± 0.014 |
| 1.6< $p_T$ <2.0 | 0.026 ± 0.028 | 0.043 ± 0.027 |
| 2.0< $p_T$ <4.0 | 0.070 ± 0.027 | 0.057 ± 0.027 |

**Table 3.4**: Comparison of $v_2$ results extracted using the standard method and the $v_2$ vs. $m_{inv}$ method. Results have not been corrected for the event plane resolution.

### 3.4.3 Systematic error analysis

The main sources of systematic uncertainty in extracting $v_2$ using the $v_2$ vs. mass method and the approach to estimating them are listed below:

- **Uncertainty in the S/(S+B) and B/(S+B) ratios due to different extraction methods:**
  The S/(S+B) and B/(S+B) ratios could be extracted either by using the raw signal histogram directly or by using the Breit-Wigner function which was fitted to the $\phi$-meson mass peak. The uncertainty in the final $v_2$ result was estimated by using the ratios extracted both ways and comparing the resulting $v_2$ values. Further details are provided in Appendix B.2.

- **Uncertainty in the S/(S+B) and B/(S+B) ratios due to uncertainties in extracting the $\phi$-meson raw yield:**
  This uncertainty was estimated by over- and under-estimating by 20% the raw $\phi$-meson yield compared to the best fit result for each $p_T$ bin, and using the resulting signal values to recalculate the S/(S+B) and B/(S+B) ratios. The over- and under-estimation was done by using a second order polynomial function to describe the residual background under the $\phi$ mass peak and fixing the area parameter in the fit to 120% and 80% of the best fit result respectively. The effect of this variation in raw yield was estimated by comparing to the base case. Further details are provided in Appendix B.2.

- **Uncertainty in the shape of the background $v_2(m_{inv})$:**
  The $v_2(m_{inv})$ of the background is assumed to be a smooth function, however, there is no prescription for the expected shape. Therefore the shape of the background $v_2(m_{inv})$ was parameterised with a polynomial whose order was varied to study the effect on the final extracted $v_2$.

- **Uncertainty from event plane resolution estimation:**
  For combined centrality bins (e.g. 0-80% minbias) the event plane resolution correction factor could be calculated as a raw-yield-weighted average and applied to the final extracted $v_2$ values. Alternatively, the particular event plane correction factor corresponding to a specific

centrality bin could be applied to the $v_2$ vs. $m_{inv}$ distribution, the distributions added together and the final $v_2$ result fitted. Both methods were used and the difference in the results was included in the systematic errors.

Due to the limited statistics available for extracting the $\phi$-meson $v_2$, the contribution from non-flow effects [43,82] was not estimated here. From other identified particle studies, these effects may be up to the order of a relative 10% and may reduce the final $v_2$ results by this amount.

### 3.4.4 Extracting $\langle v_2 \rangle$

The integrated elliptic flow $\langle v_2 \rangle$ is also an observable of interest which can be found by convoluting the differential $v_2(p_T)$ with the transverse momentum spectra according to:

$$\langle v_2 \rangle = \frac{\int v_2(pT) dN/dp_T dp_T}{\int dN/dp_T dp_T}. \tag{3.19}$$

To extract the $\langle v_2 \rangle$ for the $\phi$-meson and other identified particles, each $v_2(p_T)$ distribution was fitted with two functions: a polynomial function, the order depending on the $v_2$ distribution under study, and a function of the form

$$f_{v_2}(n) = \frac{an}{1 + \exp\left(-(p_T/n - b)/c\right)} - dn. \tag{3.20}$$

The function in equation 3.20 was inspired by parameterizations of quark number scaling in [47]. Since the $v_2(p_T)$ measurements are restricted to a limited $p_T$ range due to the available statistics, extrapolations down to $p_T = 0$ GeV/$c$ (where by definition $v_2(p_T) = 0$) and up to higher $p_T$ were made.

For each centrality bin and particle under study, the corresponding fully corrected $p_T$ spectrum was fitted with an appropriate distribution and normalized so that its integral was unity.

The $v_2(p_T)$ parameterizations were then convoluted with the normalized particle spectra and integrated to find the $\langle v_2 \rangle$. The statistical errors from the $v_2(p_T)$ measurements, were fitted as a function of $p_T$ and extrapolated to lower and higher $p_T$. The final $\langle v_2 \rangle$ was taken as the mean of the two results obtained when using a polynomial function to fit $v_2(p_T)$ or the function in equation 3.20. The systematic errors were estimated from the difference in the two results. Further details on the method can be found in Appendix B.3.

# Chapter 4

# Results and Discussion

## 4.1 Transverse momentum spectra

The transverse momentum distributions of the $\phi$-meson from Au+Au collisions at $\sqrt{s_{NN}} = 200$ GeV, after correction for detector inefficiencies, acceptance, and the branching ratio of the $\phi$ to charged kaons (49.2%), are presented in Fig. 4.1 as a function of centrality. The statistical errors are indicated by the error bars (mostly smaller than the size of the markers) and the systematic errors, calculated as described in Chapter 3.3.5, are represented by the shaded bands. For reference, tables containing the data and statistical and systematic errors for each centrality bin are presented in Appendix A.

The dashed lines in Fig. 4.1 are exponential fits of the form:

$$\frac{1}{2\pi p_T}\frac{d^2N}{dydp_T} = \frac{dN/dy}{2\pi T(m_0+T)}e^{-\frac{\sqrt{(m_0^2+p_T^2)}-m_0}{T}} \tag{4.1}$$

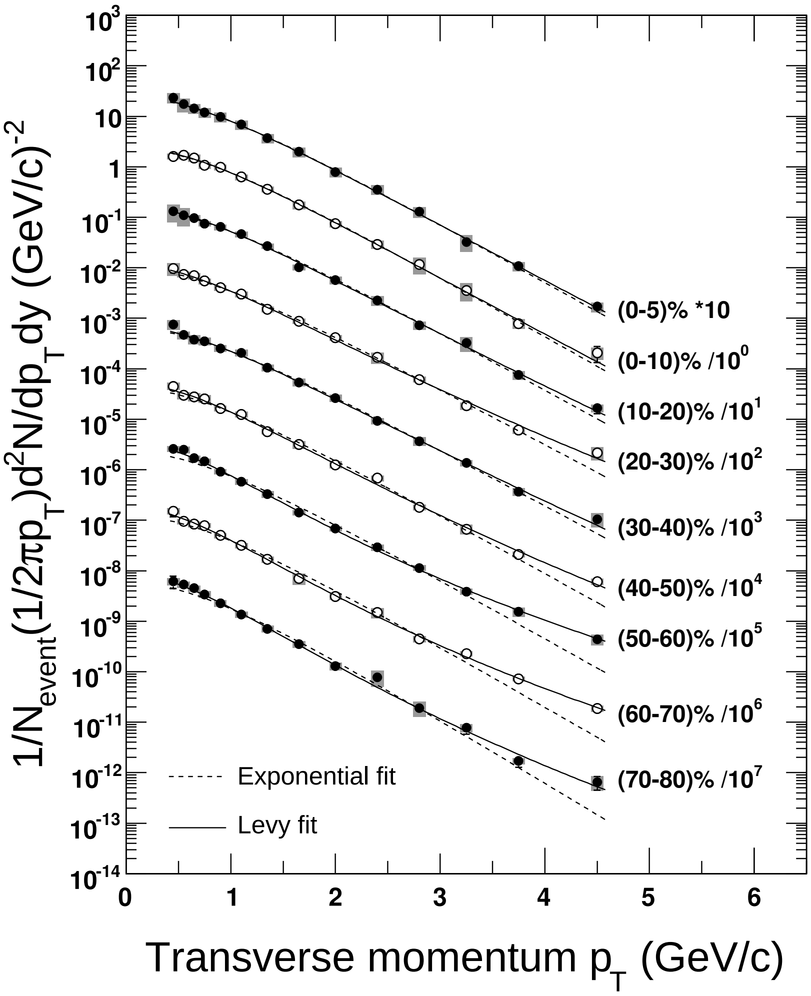


**Figure 4.1**: $\phi$-meson transverse momentum spectra for a range of centrality bins. The 0-5% spectrum is from the central-triggered dataset, the remainder are from the minbias dataset. The shaded bands represent the systematic errors, while the statistical errors, represented by error bars, are in almost all cases, smaller than the size of the markers. The dashed(solid) line represents an exponential(Levy) function fit to the data.

while the solid lines are Levy function fits [83] of the form:

$$\frac{1}{2\pi p_T}\frac{d^2N}{dydp_T} = \frac{dN}{dy}\frac{(n-1)(n-2)}{2\pi nT(nT+m_0(n-2))}\left(1+\frac{\sqrt{p_T^2+m_0^2}-m_0}{nT}\right)^{-n}. \tag{4.2}$$

$T$ is known as the inverse slope parameter, $dN/dy$ is the $\phi$-meson yield per unit rapidity, and $n$ is the additional Levy function parameter. While particle production at low $p_T$ is expected to be due to non-pertubative soft processes and may therefore exhibit exponential-like scaling, it is expected that pQCD hard processes (scaling with the number of binary collisions) should eventually dominate at some higher $p_T$ producing particles with a power-law distribution. This motivates the comparison of the Levy function to the data since the Levy function is similar in shape to an exponential at low $p_T$ and has a power-law-like shape at higher $p_T$.

The values of the fit parameters $T$, $dN/dy$ and $n$, as well as the $\chi^2$/ndf of the exponential and Levy function fits, are presented in Table 4.1 and Table 4.2 respectively. From both the figure and the $\chi^2$ values presented in the tables, it can be seen that the exponential and Levy functions fit the central data equally well. However, with decreasing centrality, the exponential fits diverge from the data and the Levy function fits the data better. This evolution in the shape of the spectra from exponential-like in central collisions to more power-law-like in peripheral collisions reflects the increasing contribution from pQCD (hard) processes to $\phi$-meson production in more peripheral collisions.

| **Centrality (%)** | **Exponential fit parameters** | | |
|---|---|---|---|
| | $T$ (GeV) | $dN/dy$ | $\chi^2$/ndf |
| 0–5 | 0.367 ± 0.003 | 7.751 ± 0.099 | 24.8/12 |
| 0–10 | 0.361 ± 0.006 | 7.387 ± 0.159 | 10.1/12 |
| 10–20 | 0.373 ± 0.005 | 5.090 ± 0.104 | 24.9/12 |
| 20–30 | 0.386 ± 0.006 | 3.370 ± 0.067 | 30.9/12 |
| 30–40 | 0.383 ± 0.005 | 2.166 ± 0.043 | 22.2/12 |
| 40–50 | 0.367 ± 0.006 | 1.341 ± 0.029 | 46.8/12 |
| 50–60 | 0.364 ± 0.007 | 0.727 ± 0.018 | 70.9/12 |
| 60–70 | 0.356 ± 0.008 | 0.380 ± 0.012 | 54.4/12 |
| 70–80 | 0.339 ± 0.009 | 0.170 ± 0.007 | 31.7/12 |

**Table 4.1**: Results from exponential fits to the $\phi$-meson $p_T$ spectra presented in Fig. 4.1.

Table 4.3 presents the $\phi$ yields vs. centrality. The mean values and statistical errors are taken from the Levy function fit results. The systematic

| Centrality (%) | Levy function fit parameters | | | |
|---|---|---|---|---|
| | $T$ (GeV) | $n$ | $dN/dy$ | $\chi^2$/ndf |
| 0–5 | 0.355 ± 0.008 | 102.9 ± 116.8 | 7.798 ± 0.105 | 22.5/11 |
| 0–10 | 0.349 ± 0.015 | 93.2 ± 101.8 | 7.422 ± 0.164 | 9.3/11 |
| 10–20 | 0.346 ± 0.013 | 45.5 ± 25.6 | 5.148 ± 0.108 | 20.2/11 |
| 20–30 | 0.329 ± 0.015 | 21.6 ± 5.6 | 3.448 ± 0.071 | 15.8/11 |
| 30–40 | 0.352 ± 0.014 | 38.9 ± 20.0 | 2.189 ± 0.045 | 16.9/11 |
| 40–50 | 0.301 ± 0.013 | 18.2 ± 3.6 | 1.396 ± 0.033 | 22.9/11 |
| 50–60 | 0.250 ± 0.014 | 10.1 ± 1.2 | 0.806 ± 0.023 | 9.6/11 |
| 60–70 | 0.250 ± 0.015 | 10.8 ± 1.4 | 0.419 ± 0.014 | 6.5/11 |
| 70–80 | 0.252 ± 0.019 | 13.3 ± 2.8 | 0.190 ± 0.009 | 11.6/11 |

**Table 4.2**: Results from Levy function fits to the $\phi$-meson $p_T$ spectra presented in Fig. 4.1.

errors were calculated as the square-root of the quadrature sum of contributions from three main sources:

- difference in results between the Levy and exponential fits. This contribution is only in the negative direction since the Levy results were systematically higher than the exponential results for all centralities.
- contribution from particle identification uncertainty. The spectra were obtained systematically using a kaon identification cut of $1\sigma$, $2\sigma$ (standard cut) and $3\sigma$ on the $dE/dx$ values. The resulting $dN/dy$ values, after correction for the respective confidence intervals, were compared and the contribution was estimated to be an approximately 8% relative effect.
- contribution due to varying the fitting criteria (e.g. fit range, function to describe the residual background) applied to the $m_{inv}$ distributions when extracting the raw yields.

Table 4.4 presents the slope parameter $T$, with its errors. The mean $T$ values and statistical errors were calculated from the Levy function fits. The systematic errors were calculated as the square-root of the quadrature sum of the contribution from the difference in exponential and Levy function results

| **Centrality** (%) | $dN/dy$ ± **stat. err** | **sys. err** | | **Measured fraction** |
|---|---|---|---|---|
| 0–5 | 7.798 ± 0.105 | +0.645 | –0.646 | 0.56 |
| 0–10 | 7.422 ± 0.164 | +0.598 | –0.599 | 0.56 |
| 10–20 | 5.148 ± 0.108 | +0.435 | –0.439 | 0.56 |
| 20–30 | 3.448 ± 0.071 | +0.289 | –0.299 | 0.55 |
| 30–40 | 2.189 ± 0.045 | +0.175 | –0.177 | 0.56 |
| 40–50 | 1.396 ± 0.033 | +0.112 | –0.124 | 0.53 |
| 50–60 | 0.806 ± 0.023 | +0.065 | –0.102 | 0.50 |
| 60–70 | 0.419 ± 0.014 | +0.034 | –0.052 | 0.50 |
| 70–80 | 0.190 ± 0.009 | +0.015 | –0.025 | 0.49 |

**Table 4.3**: $dN/dy$ values vs. centrality using the Levy function fit results as the base case and including systematic errors calculated as described in the text. The rightmost column shows the measured fraction of the total yields.

(point-to-point) and the effect of varying the fitting criteria when extracting the raw yields.

| **Centrality** (%) | $T$ ± **stat. err** (GeV) | **sys. err** (GeV) | |
|---|---|---|---|
| 0–5 | 0.355 ± 0.008 | +0.013 | –0.004 |
| 0–10 | 0.345 ± 0.015 | +0.014 | –0.005 |
| 10–20 | 0.346 ± 0.013 | +0.031 | –0.015 |
| 20–30 | 0.329 ± 0.015 | +0.059 | –0.018 |
| 30–40 | 0.352 ± 0.014 | +0.033 | –0.008 |
| 40–50 | 0.301 ± 0.013 | +0.066 | –0.006 |
| 50–60 | 0.250 ± 0.014 | +0.115 | –0.007 |
| 60–70 | 0.250 ± 0.014 | +0.105 | –0.004 |
| 70–80 | 0.252 ± 0.019 | +0.087 | –0.008 |

**Table 4.4**: Slope parameter, $T$, values vs. centrality from the Levy function fit results and including systematic errors calculated as described in the text.

### 4.1.1 $\phi$-meson $\langle p_T \rangle$

The $\langle p_T \rangle$ for the $\phi$ (presented in Table 4.5) was calculated using the Levy function fits as a function of centrality. The statistical errors were extracted by independently varying each of the Levy function parameters ($T$, $dN/dy$, $n$) by the range of their respective errors and recalculating the resulting $\langle p_T \rangle$. The systematic errors included contributions from the results obtained when using an exponential fit function instead of the Levy function, differences in the results when applying a $1\sigma$, $2\sigma$ or $3\sigma$ particle identification cut for the daughter kaons, and contributions from varying the fitting criteria when extracting the raw yields.

| **Centrality** (%) | $\boldsymbol{\langle p_T \rangle}$ **± stat. err** (GeV) | **sys. err** (GeV) | |
|---|---|---|---|
| 0–5 | 0.990 ± 0.023 | +0.008 | –0.028 |
| 0–10 | 0.979 ± 0.038 | +0.013 | –0.023 |
| 10–20 | 0.991 ± 0.037 | +0.025 | –0.008 |
| 20–30 | 0.999 ± 0.042 | +0.060 | –0.046 |
| 30–40 | 1.010 ± 0.039 | +0.022 | –0.002 |
| 40–50 | 0.951 ± 0.041 | +0.049 | –0.006 |
| 50–60 | 0.905 ± 0.048 | +0.088 | –0.014 |
| 60–70 | 0.894 ± 0.052 | +0.082 | –0.017 |
| 70–80 | 0.870 ± 0.064 | +0.074 | –0.019 |

**Table 4.5**: $\langle p_T \rangle$ vs. centrality (corresponding to Fig. 4.2)

In Figure 4.2, we compare the $\langle p_T \rangle$ vs. $dN_{ch}/d\eta$ (proportional to the collision centrality) of the $\phi$-meson to $\pi$, $K^-$, $\bar{p}$ (from STAR [84]). The shape of the $\langle p_T \rangle$ distributions of $\pi$, $K^-$ and $\bar{p}$ display an increasing trend from $p+p$ and the most peripheral Au+Au to more central collisions and seem to saturate only in the most central bins. The increase with centrality may be understood in terms of the contribution from rescattering in the hadronic stage which is larger in central than peripheral collisions. The $\phi$-meson $\langle p_T \rangle$ distribution also shows an initial increase from most peripheral collisions but seems to saturate earlier than the other particles. Also, the increase is not as large as for the $\bar{p}$ since the $\phi$ $\langle p_T \rangle$ is systematically higher than $\bar{p}$ in peripheral collisions and the same or lower than $\bar{p}$ in more central collisions. This may be an indication that the $\phi$ suffers fewer interactions in the hadronic stage than these other particles i.e it freezes out earlier.

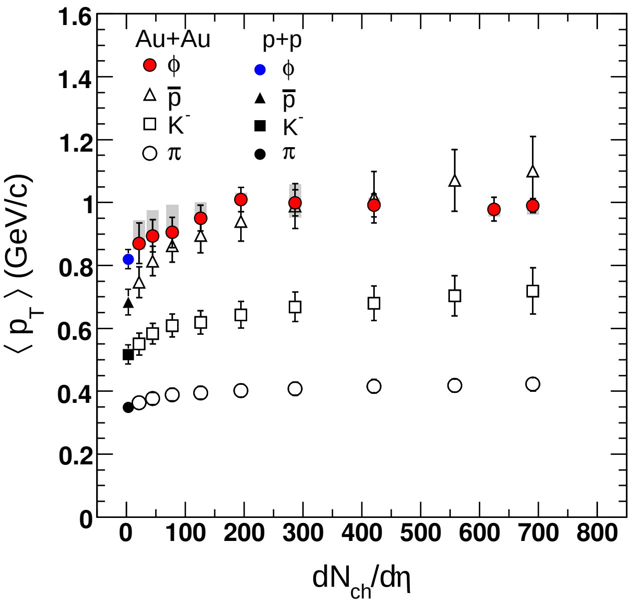


**Figure 4.2**: $\phi$-meson $\langle p_T \rangle$ (solid red circles) vs. centrality ($dN_{ch}/d\eta$) compared to $\pi$ (open circles), $K^-$ (squares) and $\bar{p}$ (triangles) [84] from Au+Au collisions. The p+p collision $\langle p_T \rangle$ results are shown for $\pi$, $K^-$, $\bar{p}$ (solid black symbols) [84] and $\phi$ (blue solid circle) [57]. Statistical errors are indicated by the solid lines and systematics are shown by the shaded bands.

The evidence for early freeze-out of the $\phi$-meson is strengthened by comparing the values for $T_{fo}$ and $\langle \beta \rangle$ extracted previously from hydrodynamically-inspired Blastwave model fits to the most central $\phi$-meson $p_T$ spectra to that of $\pi$, $K$ and $p$, see Fig. 1.10 [22] in Chapter 1. Although the previous results for the $\phi$-meson presented in Fig. 1.10 were obtained using the smaller statistics 2002 dataset, consistent updated results have been obtained upon fitting to the latest high statistics dataset. Therefore, one can conclude that in central collisions, the higher $T_{fo}$ and lower $\langle \beta \rangle$ results for the $\phi$-meson compared to $\pi$, $K$ and $p$ imply that the $\phi$ freezes out earlier, when the system was hotter.

## 4.2 The nuclear modification factor: $R_{CP}$

The nuclear modification factor $R_{CP}$ measures the difference in the $p_T$ spectra (i.e. the difference in particle production) for central compared to more peripheral Au+Au collisions (see equation 1.8). Figure 4.3 shows the $R_{CP}$ results for the $\phi$-meson (red filled circles) from Au+Au collisions at $\sqrt{s_{NN}} = 200$ GeV for two different choices of peripheral centrality: the upper panel shows 0-5%/40-60% and the lower panel shows 0-5%/60-80%. The vertical error bars represent the statistical errors and the shaded grey bands show the systematic errors. The systematic errors are propagated from the input $p_T$ spectra and vary from point-to-point. The main contributions are from uncertainties in extracting the raw $\phi$-meson yields estimated by varying the yield fitting criteria and parameters (see section 3.3.5 for details) and corrections for the kaon identification efficiency. The short and long horizontal dashed lines indicate the expectation for $R_{CP}$ scaling with $N_{part}$ and $N_{bin}$ respectively. The yellow shaded bands indicate the uncertainty on these values from the Glauber model calculation [85]. The values for $N_{part}$ and $N_{bin}$ used here are the standard STAR values from [85]. Also shown in the plot are the $R_{CP}$ results for $K^0_S$ and $\Lambda$ [33] and $\pi^+$ and p [36] measured by STAR.

For both choices of peripheral centrality bin, the $\phi$ $R_{CP}$ is below the line at unity indicating $N_{bin}$-scaling i.e. the binary-scaled yield of $\phi$-mesons is suppressed in central compared to more peripheral collisions.

For the mid-central 40-60% denominator (upper panel of Fig. 4.3), one can see that the $\phi$-meson $R_{CP}$ is consistent with the $R_{CP}$ values of the other mesons ($K^0_S$, $\pi^+$) rather than the baryons, despite its mass being much larger than the other mesons and very similar to the $\Lambda$ and p masses. This observation is consistent with the idea that the scaling seen in $R_{CP}$ is a particle-type effect (i.e. baryons vs. mesons) rather than a mass-type effect. As outlined in section 1.3.3, this baryon-meson splitting in the tranverse momentum range $2 < p_T < 5$ GeV/$c$ may be understood in terms of particle production via quark recombination [34, 40].

In the lower panel of Fig. 4.3 one can see that the $\phi$-meson $R_{CP}$ seems

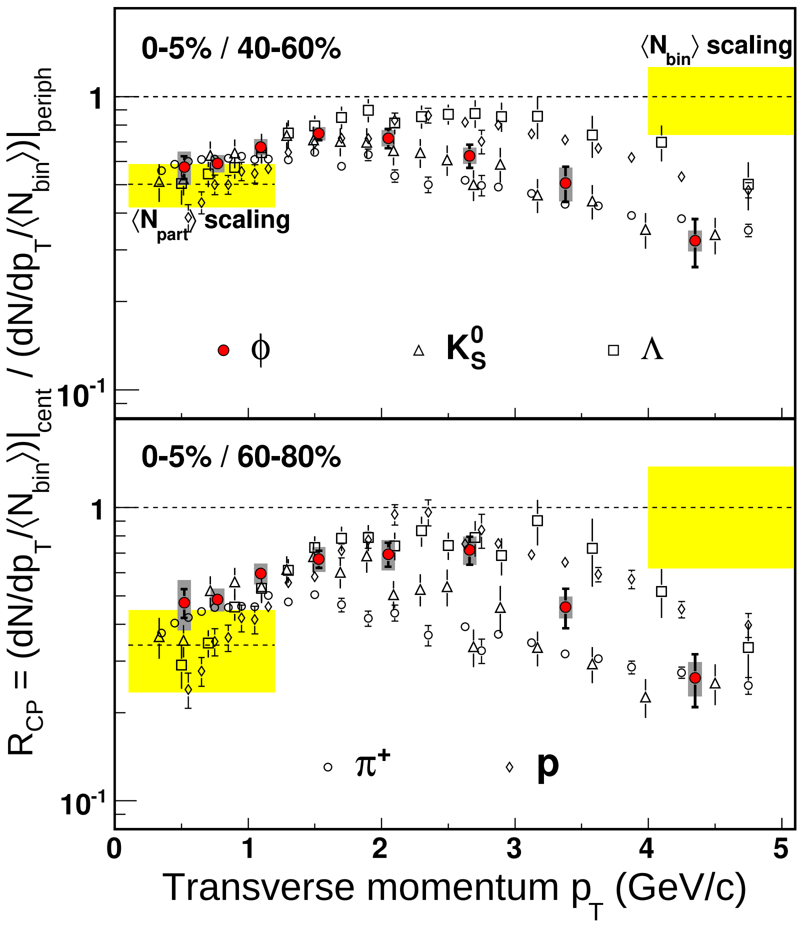


**Figure 4.3**: Nuclear modification factor $R_{CP}$ for $\phi$ (red filled circles) for two peripheral bin choices: 40-60% (top panel) and 60-80% (lower panel). Also shown are $R_{CP}$ results for $\Lambda$ (squares) and $K^0_S$ (triangles) from [33] and $\pi^+$ (open circles) and p (diamonds) from [36].

to fall inbetween the values of the $K^0_S$ and $\Lambda$ and that the division of mesons and baryons into separate bands may not be as clear as in the upper panel. Within the error bars, for baryons and mesons respectively, one may observe an ordering in terms of strangeness content, where the $R_{CP}$ increases with increasing strangeness content of the baryons or mesons respectively. A similar ordering has been observed (although the absolute values differ) in measurements of $R_{AA}$, the nuclear modification factor for Au+Au collisions with respect to p+p collisions [86]. In the case of $R_{AA}$, one possible explanation for the scaling can be understood in the context of a statistical model [87] as follows: the canonical suppression of strange particle production in p+p collisions increases with increasing strangeness content which leads to an increasing relative enhancement of particle production in A+A compared to p+p collisions as the strangeness content of the particles increases [86, 87].

Upon further comparison, the $R_{CP}$ values for the $\phi$-meson for both choices of peripheral centrality bin are very similar to each other, while there is a more noticeable change in the $K^0_S$ and $\Lambda$ values between the two bins. The reason for the apparent breaking of the baryon-meson scaling in the most peripheral $R_{CP}$ bin is still an open question. However, part of the explanation might rely on a difference in the relative contributions from competing particle production mechanisms to the different particle types from mid-central (40-60%) to peripheral (60-80%) collisions over the studied $p_T$ range.

## 4.3 Elliptic flow: $v_2(p_T)$ and $\langle v_2 \rangle$

Elliptic flow, $v_2$, measurements probe the early stages of the system created in Au+Au collisions at RHIC as discussed in section 1.3.4. The results for measurements of the $\phi$-meson $v_2(p_T)$ are presented in the following section.

### 4.3.1 Centrality dependence of $v_2$

Figure 4.4 presents the $\phi$-meson differential elliptic flow, $v_2(p_T)$, measured in Au+Au collisions at $\sqrt{s_{NN}} = 200$ GeV for four different centrality bins: minimum bias (0-80%), central (0-5%), mid-central (10-40%) and peripheral (40-80%) collisions. The error bars represent the statistical errors and the shaded bands (yellow for minimum bias and grey for all other centralities) indicate the systematic uncertainties. The systematic errors vary from point-to-point and were estimated as discussed in section 3.4.3. Due to the limited statistics available to measure the $\phi$-meson $v_2(p_T)$, non-flow effects [43, 82] have not been estimated in the systematics for the $\phi$-meson. However, recent studies for protons and pions, using the four-particle cumulant technique, indicate that the effects may be of the order of a relative 15-20% [88] in the negative direction. i.e. will reduce the $v_2$ values.

From Fig. 4.4 one can see that the $\phi$-meson has a finite $v_2(p_T)$ for all centralities and that the $v_2$ values increase with decreasing centrality, or increasing eccentricity of the inital nuclear overlap area, as expected and observed in $v_2$ measurements of other identified particles [43]. Since dividing the data into the various centrality bins limits the statistics for the $v_2$ measurements, the following $v_2(p_T)$ results and comparisons focus mainly on the results obtained in minimum bias (0-80%) collisions.

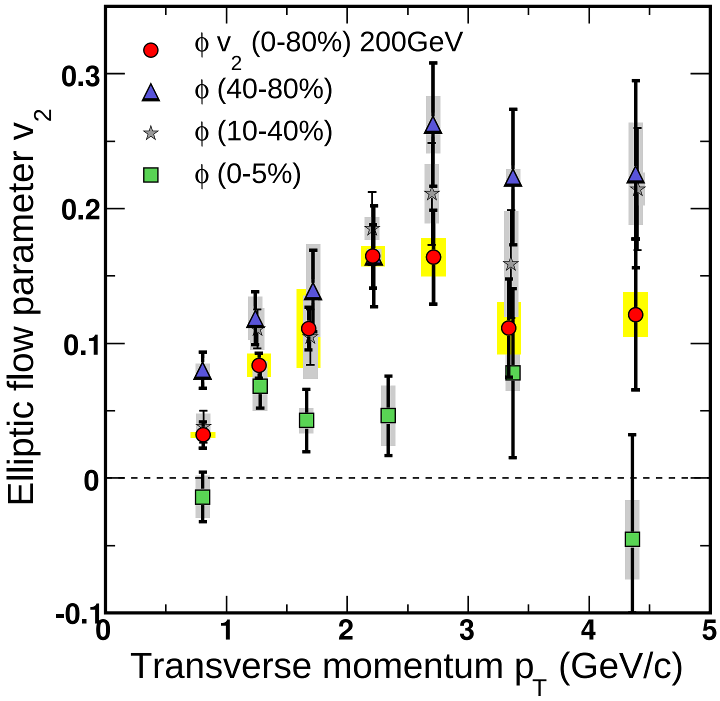


**Figure 4.4**: $\phi$-meson $v_2(p_T)$ for four centrality bins: 0-5% (squares), 10-40% (stars), 40-80% (triangles) and 0-80% (circles). Error bars represent statistical errors and shaded bands represent systematic errors.

### 4.3.2 $v_2$ Scaling behaviour

In Fig. 4.5 the minimum bias $\phi$-meson $v_2(p_T)$ (already presented in Fig. 4.4) is compared to the $v_2$ results for $\Lambda$ and $K_S^0$ measured by STAR [33]. At low $p_T$ ($p_T < 2$ GeV/$c$), one can observe a mass-ordered heirarchy (within the errors) in the $v_2$ values of the studied particles. The $\phi$ $v_2$ trend falls between that of the lighter $K_S^0$ and heavier $\Lambda$. This is consistent with the expectation from hydrodynamics where particles boosted with a common velocity will appear shifted in the $p_T$ variable due to their different masses.

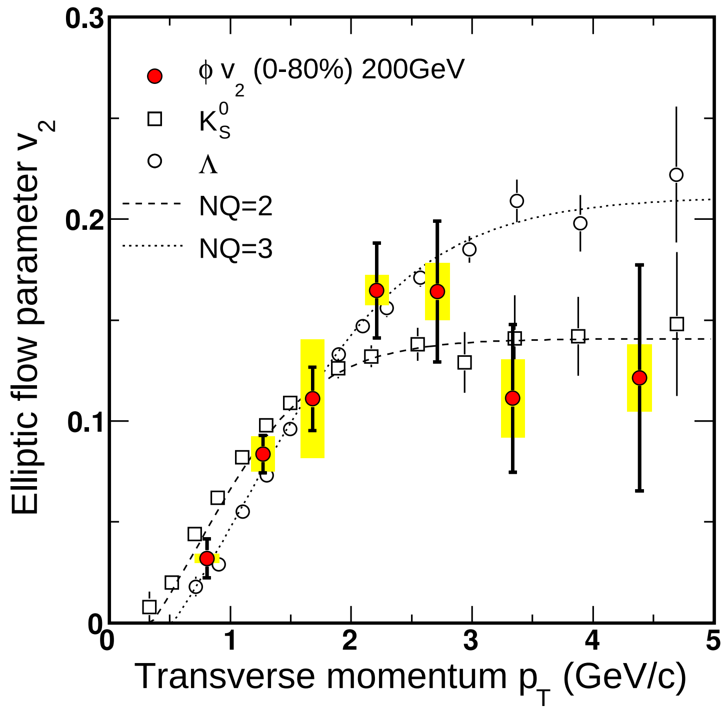


**Figure 4.5**: Minimum bias (0-80%) $\phi$ $v_2(p_T)$ (filled circles) for Au+Au collisions at $\sqrt{s_{NN}} = 200$ GeV. Also shown are $v_2(p_T)$ results for $\Lambda$ (open circles) and $K_S^0$ (squares) from [33]. The dashed and dotted lines represent parameterizations [47] for number of quark (NQ) scaling = 2 and 3 respectively.

As mentioned in section 1.3.4, the phenomenon of *quark number scaling*, where the $v_2(p_T)$ of mesons and baryons scales according to their number of valence quarks, has been observed in Au+Au collisions at RHIC at intermediate $p_T$, $2 \lesssim p_T \lesssim 5$. The dotted and dashed lines in Fig. 4.5 are parameterizations for baryon (NQ = 3) and meson-scaling (NQ = 2) taken from [47] which have the form:

$$f_{v_2}(n) = \frac{an}{1 + \exp\left(-(p_T/n - b)/c\right)} - dn \tag{4.3}$$

where $n$ is the number of valence or constituent quarks and the parameters $a, b, c$ and $d$ were extracted by fitting to STAR results for $\Lambda$ and $K^0_S$ simultaneously. One can see that in the intermediate $p_T$ range, the $v_2(p_T)$ of the $\phi$-meson is consistent with that of the $K^0_S$ and the parameterization for meson-scaling (NQ = 2). In order to quantify the level of consistency with meson-scaling observed for $p_T/n_q \gtrsim 0.75$ GeV/$c$ [45], the $\phi$ $v_2(p_T)$ for $p_T/n_q > 0.75$ GeV/$c$ (i.e excluding the lowest two datapoints) was fitted using the function in equation 4.3. The values of $a, b, c$ and $d$ were fixed to the values in [47] but the number of quarks, $n$, was left as a free parameter in the fit. The results for $n$ are presented in Table 4.6 for the case of fitting to the datapoints including only statistical errors and for the case where both the statistical and systematic errors were taken into account by taking the square root of their quadrature sum as the error on the datapoints. Within the errors, the values obtained for $n$ show that the $\phi$ $v_2$ results follow the meson-scaling trend.

| **Details of fitted data** | $\boldsymbol{n}$ |
|---|---|
| Using statistical errors on $v_2(p_T)$ only | $2.1 \pm 0.3$ |
| Using quadrature sum of statistical and systematic errors on $v_2(p_T)$ | $2.2 \pm 0.3$ |

**Table 4.6**: Results for $n$ from fitting the quark number scaling function from [47] to the $\phi$-meson minimum bias $v_2(p_T)$ results for two sets of error options (statistical errors only, and combination of statistical and systematic errors).

### 4.3.3 Energy dependence of $v_2$

The collision energy dependence of the $\phi$ $v_2(p_T)$ is studied by comparing the results from minimum bias Au+Au collisions at $\sqrt{s_{NN}} = 62.4$ GeV and 200 GeV in Fig. 4.6. Due to the limited statistics in the 62 GeV dataset, the $v_2(p_T)$ was measured over a smaller $p_T$ range than for 200 GeV collisions. The systematic errors for the 62.4 GeV $v_2(p_T)$ result includes the difference between using the standard event plane ($\phi$-binning) method and the $v_2$ vs. mass method in addition to the contributions described in section 3.4.3.

Within the large statistical and systematic uncertainties of the 62.4 GeV result, the two measurements appear consistent with each other which is in agreement with measurements for other identified particles at the two energies [88].

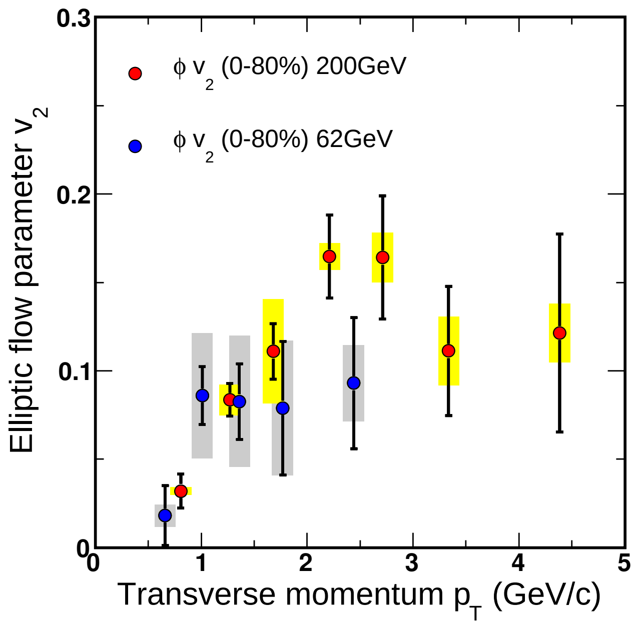


**Figure 4.6**: Minimum bias (0-80%) $\phi$ $v_2(p_T)$ for Au+Au collisions at $\sqrt{s_{NN}} = 200$ GeV (red circles) and $\sqrt{s_{NN}} = 62.4$ GeV (blue circles). Error bars represent statistical errors and shaded bands represent systematic errors.

### 4.3.4 $\langle v_2 \rangle$ and $\langle v_2 \rangle/\epsilon$

Studies of the integrated or mean elliptic flow, $\langle v_2 \rangle$, are useful to investigate trends as a function of collision centrality. Figure 4.7 presents the $\phi$-meson $\langle v_2 \rangle$ for 0-5%, 10-40% and 40-80% central Au+Au collisions at $\sqrt{s_{NN}}$ = 200 GeV. The $\langle v_2 \rangle$ values for $K^0_S$, $\Lambda$ and $\Xi$ for 0-10%, 10-40% and 40-80% central collisions were also calculated, following the method described in section 3.4.4, using the $v_2(p_T)$ results from [88,89]. Also shown in the plot are the results for charged hadrons ($h^{\pm}$) from [43] extracted using the standard event plane method.

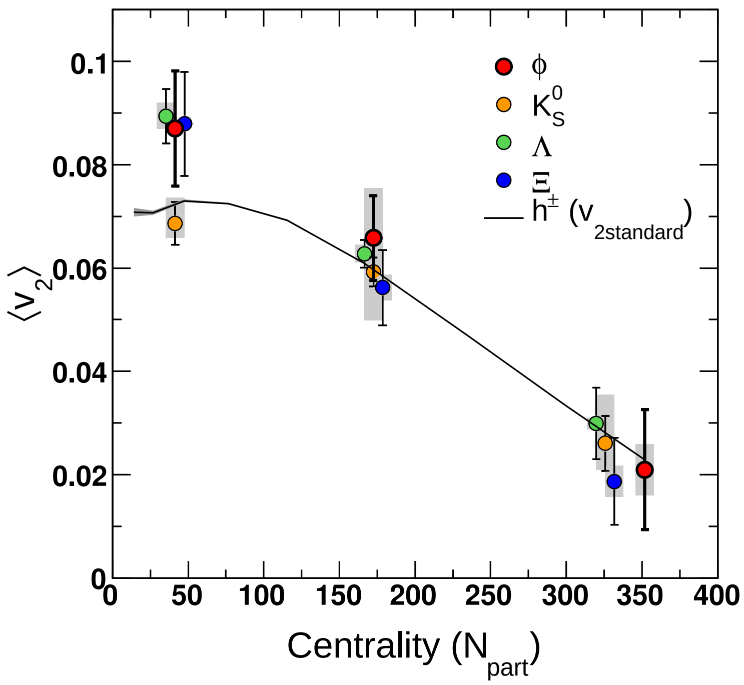


**Figure 4.7**: $\langle v_2 \rangle$ for identified strange particles. Centrality bins for $K^0_S$, $\Lambda$, $\Xi$ are 0-10%, 10-40%, 40-80%. The datapoints are shifted in the variable, $N_{part}$ for clarity in presentation. The centrality bins for $\phi$ are 0-5%, 10-40%, 40-80%. The error bars are the statistical errors and the shaded bands represent the systematic uncertainties.

The $\langle v_2 \rangle$ values decrease with increasing centrality for all the identified particles as well as the charged hadrons. This is expected since the eccentricity of the initial overlap region of the colliding nuclei decreases from peripheral to central collisions.

In order to investigate the collectivity of the medium further and remove the effects due to the initial spatial geometry of the produced medium, it is of interest to study the centrality dependence of the integrated elliptic flow, $\langle v_2 \rangle$, divided by the eccentricity, $\epsilon$, of the system. Here the participant eccentricity, $\epsilon_{part}$, calculated using a Monte Carlo Glauber Model, is used. The values for $\epsilon_{part}$ are from [90]. The motivation for using $\epsilon_{part}$, is that this calculation of the eccentricity takes into account fluctuations in $\epsilon$ for a fixed impact parameter event-by-event. As discussed in [91, 92] even for collisions with the same impact parameter, there are various sources of fluctuations. For example the absolute number of participating nucleons involved may vary and their positions in the transverse plane can fluctuate from event to event. Therefore, in [91], the participant eccentricity calculation takes the fluctuations into account by incorporating the fluctuations in the direction of the major axes of the overlap region and the fluctuations in its center of mass.

Figure 4.8 presents the $\langle v_2 \rangle / \epsilon_{part}$ as a function of centrality for the $\phi$-meson, $K^0_S$, $\Lambda$, $\Xi$ and charged hadrons. Also shown in the plot are hydrodynamical model calculations for $\langle v_2 \rangle / \epsilon$ for $K^0_S$, $\Lambda$ and $\Xi$ from [89, 93] where in this case $\epsilon$ is the standard eccentricity (described in section 1.3.4), appropriate for the comparison here since in the calculations, the reaction plane is known exactly and does not have to estimated as it does for the experimental case. Within the errors, one can observe an upward trend in $\langle v_2 \rangle / \epsilon_{part}$ with increasing centrality of the collisions. Non-flow effects (which may be significant in central collisions [88]) have not been included in the results for statistical reasons explained before. However, the increase in $\langle v_2 \rangle / \epsilon_{part}$ with centrality may imply that there is greater collectivity in the system created in central Au+Au collisions than in peripheral collisions at RHIC. For this observable, it is also for the most central collisions that the hydrodynamical model and data agree (within the statistical errors).

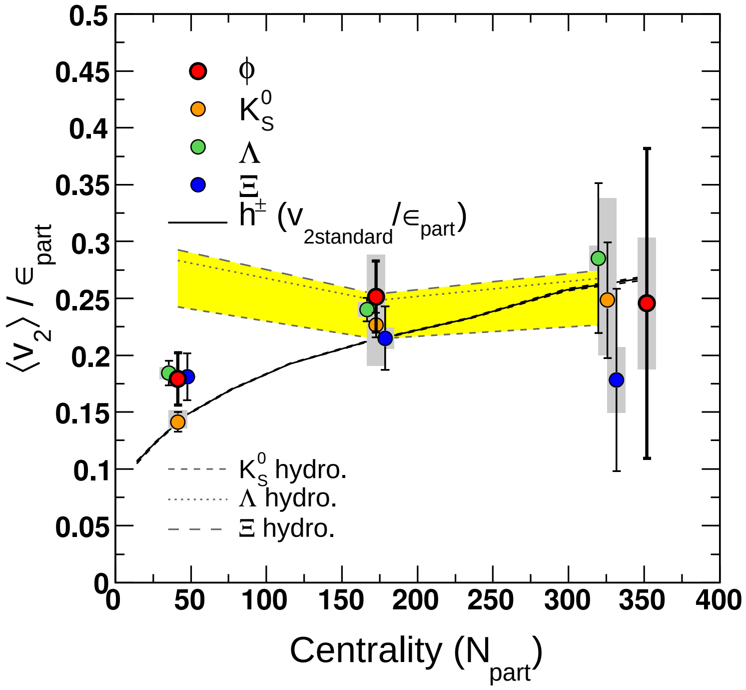


**Figure 4.8**: $\langle v_2 \rangle / \epsilon_{part}$ for identified strange particles. Centrality bins for $K_S^0$, $\Lambda$, $\Xi$ are 0-10%, 10-40%, 40-80% [89]. The datapoints are shifted in the variable, $N_{part}$ for clarity in presentation. The centrality bins for $\phi$ are 0-5%, 10-40%, 40-80%.

## 4.4 The $N(\Omega)/N(\phi)$ ratios and comparison to recombination model expectations

As discussed in section 1.3.3, anomalously large baryon/meson yield ratios (e.g. for $p/\pi$ and $\Lambda/K_S^0$) of $\sim 1$ have been observed at intermediate $p_T$ ($2 < p_T < 5$ GeV/$c$) in Au+Au collisions at RHIC [35,36]. This so-called "baryon anomaly" prompted the description of particle production through quark coalescence and models of this mechanism [34,39,94,95] have been successful in qualitatively describing the measured ratios as a function of $p_T$. The splitting of the identified particle $R_{CP}$ into baryon and meson bands and the number of quark scaling in the $v_2$ results from RHIC also lend support to the picture of particle production through quark recombination at intermediate $p_T$. In order to test the recombination hypothesis further, in this section we present the multistrange baryon/meson ratios, $N(\Omega)/N(\phi)$ vs. $p_T$ as a function of collision centrality and compare to the expectations from three different recombination models.

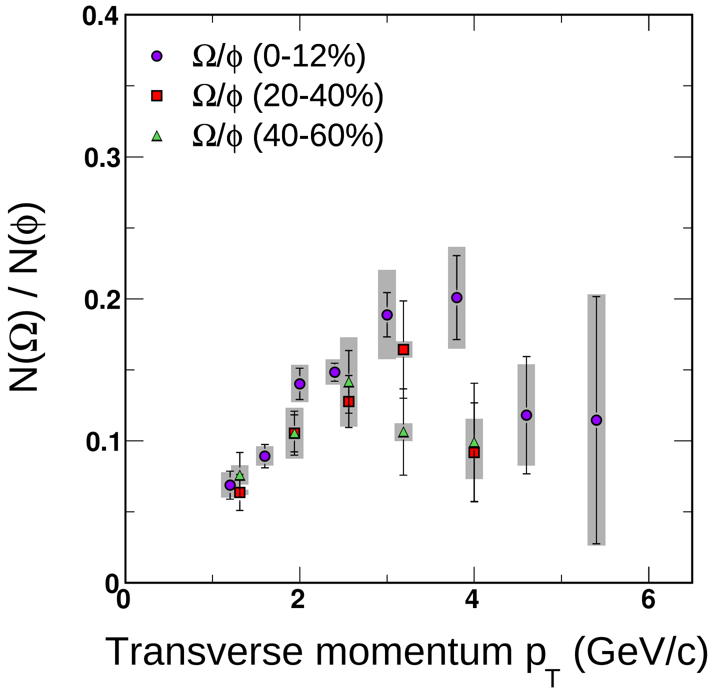


**Figure 4.9**: $N(\Omega)/N(\phi)$ ratios vs. $p_T$ for three centrality bins: circles represent 0-12%, squares represent 20-40% and triangles represent 40-60% ratios. The error bars indicate the statistical errors and the shaded bands show the systematic uncertainties. The $\Omega$ data are taken from [22] for the most central bin and [96] for 20-40% and 40-60% bins.

In Fig. 4.9 we present the centrality dependence of the $N(\Omega)/N(\phi)$ ratios vs. $p_T$. The most central $\Omega$ spectrum used in the central ratio is from [22] and the 20-40% and 40-60% $\Omega$ spectra are from [96]. The $\phi$ spectra were measured as part of the work for this thesis. The systematic and statistical errors are dominated by the $\Omega$ measurements from the smaller statistics 200 GeV Au+Au dataset from the 2002 RHIC run. Systematic errors were not available for the $\Omega$ $p_T$ spectra and were estimated from measurements of the $\Xi$ baryon which used a similar analysis procedure [97]. In the figure, one can see that the $N(\Omega)/N(\phi)$ ratios increase from low $p_T$, turn over at intermediate $p_T$ and decrease towards higher $p_T$ for all three centralities. The ratios also increase with increasing centrality, as has been observed for example in the $N(p)/N(\pi)$ [36] and $N(\Lambda)/N(K^0_S)$ [35] ratios at RHIC. In addition, with increasing centrality, the ratios seem to turn over at successively higher values of $p_T$.

### 4.4.1 Comparison to models of quark recombination

In the following section, the expectations of three recombination models by Fries et al. [34], Hwa and Yang [58] and Chen and Ko [98] are compared to the $\Omega$ and $\phi$ $p_T$ spectra and the resulting ratios of their yields, $N(\Omega)/N(\phi)$, as a function of $p_T$ and centrality.

The left panels of Figures 4.10, 4.12 and 4.14 show the $p_T$ spectra measurements by the STAR experiment for the $\Omega$ baryon in Au+Au collisions at $\sqrt{s_{NN}}$ = 200 GeV. The 0-10% spectrum is from [22] and the 20-40% and 40-60% spectra are from [96]. The right panels of Figures 4.10, 4.12 and 4.14 present the $\phi$-meson spectra for 0-12% (taken from the central-triggered dataset), 20-40% and 40-60% collisions for the same binning in $p_T$ as the $\Omega$ data. Figures 4.11, 4.13 and 4.15 present the $N(\Omega)/N(\phi)$ ratios vs. $p_T$ for each centrality bin compared to model expectations. In the following, the model calculations usually refer to the collision centrality in terms of the impact parameter $b$. For ease of comparison, it should be noted that the 0-10%, 20-40% and 40-60% centrality bins used for the data analysis, correspond to impact parameter values of $b \sim 3.2$, 8.1, and 10.5 respectively, as calculated using a Glauber model by STAR [99].

#### Model 1: Fries et al.

The dynamical recombination model employed by Fries et al. in [34] for 200 GeV Au+Au collisions, assumes that before hadronization, the underlying parton distribution of the system consists of two parts: an exponential distribution describing the bulk at low $p_T$ and a perturbative QCD power-law tail at higher $p_T$. The distributions for the different quark flavours vary in their normalizations i.e. the distributions for the lighter $u$ and $d$ quarks are higher than for the heavier $s$ quarks. In this model, constituent quarks from the exponential distribution are recombined into hadrons acccording to the model formalism while other hadrons are formed via fragmentation from the pQCD distribution. The contributions are added together to obtain the final $p_T$ distributions of the hadrons. Due to large theoretical uncertainties and a lack of appropriate fragmentation functions for the multistrange hadrons $\Omega$ and $\phi$, the authors calculate only the recombination contribution based on the underlying exponential parton distribution for these particles and neglect any perturbative fragmentation contribution. In this model framework, the distribution of mesons is proportional to

$$\frac{dN_M}{d^3p} \propto \int f(\overrightarrow{r}, \overrightarrow{p}) \times \rho^W(\overrightarrow{r}, \overrightarrow{p}) d^3\overrightarrow{r} \tag{4.4}$$

where $f(\overrightarrow{r}, \overrightarrow{p})$ represents the parton phase space distribution and $\rho^W(\overrightarrow{r}, \overrightarrow{p})$ is the Wigner phase-space distribution of quarks inside the meson [34]. The formalism is extended also to the case of baryons in [34]. The normalizations for the different particles are extracted from fits to data, for example particle yields, measured in experiment.

The model expectations from Fries et al. are compared to the $\Omega$ and $\phi$ spectra in Fig. 4.10. In the left panel, the thick solid, dashed, and thin solid lines represent the model expectations for the $\Omega$ $p_T$ distributions for 0-10%, 20-40% and 40-60% central Au+Au collisions respectively. The model curves are higher than the STAR data in all cases. However, in an attempt to gain information from the model in terms of the expected shape of the distribution (and neglecting the absolute normalization), we have rescaled the model curve for central collisions by a factor of $\pi$ (arbitrary scaling factor), which brings the curve into good agreement with the data as shown by the dotted line in the figure. The model expectations agree well with the $\phi$ spectra between $2 < p_T < 4$ GeV/$c$ which can be seen in the right panel of Fig. 4.10.

The model expectation for the $N(\Omega)/N(\phi)$ ratios for all centrality bins, illustrated by the thick solid line, is compared to the data in Fig. 4.11. This model has only one expectation for all three centrality bins since the model

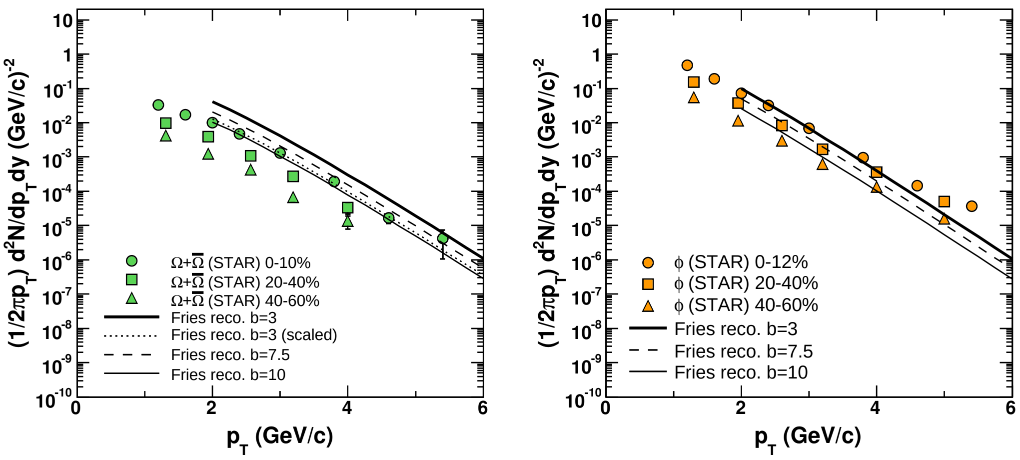


**Figure 4.10**: **Left panel:** $\Omega$ $p_T$ spectra for 0-10% [22], 20-40% and 40-60% [96] central Au+Au collisions at $\sqrt{s_{NN}} = 200$ GeV/$c$ from the STAR experiment compared to recombination model curves by Fries et al. [34] The dotted curve represents the central recombination curve (b=3 fm) scaled down by a factor of $\pi$. **Right panel:** $\phi$-meson $p_T$ spectra for 0-12%, 20-40%, 40-60% central Au+Au collisions compared to recombination model curves by Fries et al. [34].

curves for the $\Omega$ and $\phi$ spectra are scaled versions of each other i.e. the ratio per centrality bin gives the same result. Since the model overpredicts the $\Omega$ data, the resulting expectation for the ratio is much higher (greater than a factor of 2) than observed in the data. However, when using the scaled $\Omega$ model spectra to calcuate the ratios, as shown by the dotted curve in the plot, the agreement with the most central data, at least in the range $2 < p_T < 4$ GeV/$c$, is much better.

### Model 2: Chen and Ko

The coalescence model used by Chen and Ko [98] to describe the production of $\Omega$ and $\phi$ is similar in its formalism to the one by Fries et al. and is also a dynamical model involving modelling of the evolution of the system created in heavy-ion collisions. As for the Fries et al. model, the yield of mesons can also be described by equation 4.4. However, in Chen and Ko's model, instead of assuming a particular shape, the underlying parton phase-space

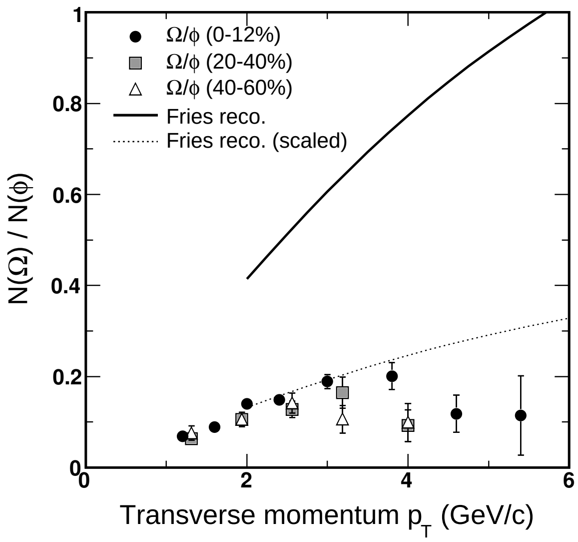


**Figure 4.11**: $N(\Omega)/N(\phi)$ ratios for 0-12% (circles), 20-40% (squares) and 40-60% (triangles) central collisions. The solid line is the recombination model expectation for all three centrality bins from Fries et al. [34]. The dotted line is the recombination model expectation using the $\Omega$ $p_T$ spectra scaled down by a factor of $\pi$.

distribution $f(\overrightarrow{r}, \overrightarrow{p})$ is taken from the AMPT model[1] [100] with string-melting. Fits to experimentally measured particle yields are used as input to the Wigner phase-space functions, $\rho^W(\overrightarrow{r}, \overrightarrow{p})$. The AMPT model is a hybrid model which combines different simulation generators to model the evolution of heavy-ion collisions from the initial conditions including partons from hard processes and strings from soft processes (HIJING[2] [101]) through the time evolution of the partons (ZPC[3] [102]), fragmentation into hadrons (PYTHIA [103]) and final-state hadronic interactions (ART model[4] [104]). In the Chen and Ko model, when so-called string-melting is included, the hadrons that would have been formed through string fragmentation are converted back into their valence quarks and these quarks are evolved through the ZPC model. When the interactions between the quarks and anti-quarks in the model stop, they are coalesced into hadrons according to the recombination model formalism.

[1] A Multi-Phase Transport model
[2] Heavy Ion Jet Interaction Generator
[3] Zhang's parton cascade
[4] A Relativistic Transport model

Figure 4.12 shows the model expectations for the $\Omega$ and $\phi$ spectra for two centrality bins (central and mid-central) from Chen and Ko [98] compared to the STAR data. For both particles, the model expects softer spectra than is observed in the data. A possible reason for the disagreement of the model with the data, suggested in [98], is that small current quark masses are used in the parton cascade stage which means that the quarks experience less radial collective flow. This results in softer quark distributions which in turn results in softer hadron spectra after coalescence.

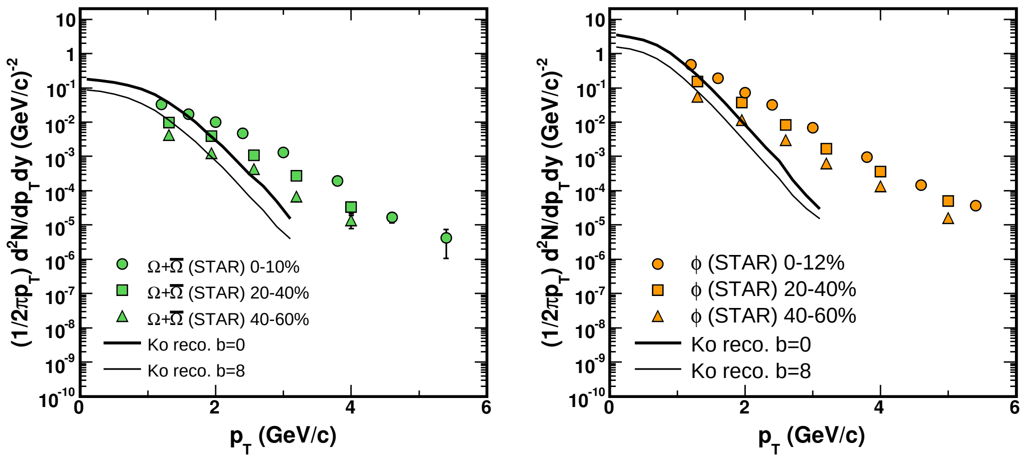


**Figure 4.12**: **Left panel:** $\Omega$ $p_T$ spectra for 0-10% [22], 20-40% and 40-60% [96] central Au+Au collisions at $\sqrt{s_{NN}} = 200$ GeV/$c$ from the STAR experiment compared to recombination model curves for different centralities by Ko et al. [98]. **Right panel:** $\phi$-meson $p_T$ spectra for 0-12%, 20-40%, 40-60% central Au+Au collisions compared to recombination model curves for different centralities by Ko et al. [98].

The $N(\Omega)/N(\phi)$ ratios obtained from the model spectra expectations are compared to the STAR data in Fig. 4.13. For all the centrality bins the model expectations are much higher than the data and have a different shape as a function of $p_T$. This is not surprising since the model expectations for the particle spectra already did not match the shape of the data.

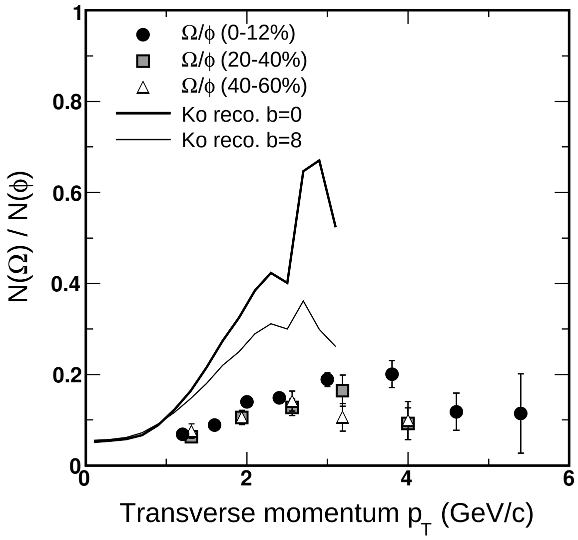


**Figure 4.13**: $N(\Omega)/N(\phi)$ ratios for 0-12% (circles), 20-40% (squares) and 40-60% (triangles) central collisions. The lines represent recombination model expectations for different centralities by Ko et al. [98].

### Model 3: Hwa and Yang

Hwa and Yang's model [58] is a non-dynamical model and has a slightly different framework to the previous two models. In this model, the distribution of mesons is proportional to

$$\frac{dN_M}{dp_T} \propto \int F_{qq'}(p_1, p_2) R_M(p_1, p_2, p) \tag{4.5}$$

where $R_M$ is the meson recombination function which includes the probability density of finding a quark with a certain momentum fraction inside the hadron i.e. it can be related to the Wigner functions of the previous two models. $F_{qq'}$ is known as the joint quark distribution and contains information about the medium properties and the underlying parton distributions. In this model, the joint quark distribution for the $\phi$-meson and $\Omega$ baryon are given by

$$F_{s\bar{s}} = T_sT_s + T_sS_s + S_sS_s \quad (4.6)$$

and (4.7)

$$F_{sss} = T_sT_sT_s + T_sT_sS_s + T_sS_sS_s + S_sS_sS_s \quad (4.8)$$

respectively, where $T_s$ stands for the thermal $s$ quark component and $S_s$ stands for the shower (fragmentation) $s$ quark component. The normalization factors for the specra are extracted by fitting to experimentally measured $p_T$ spectra for each particle type. Within this model, for $\Omega$ and $\phi$, the components involving $S_s$, the shower component, are very small since $s$ quark production from fragmentation from the lighter quarks and also gluons, is suppressed [58]. Therefore, the thermal components, $T_sT_s$ and $T_sT_sT_s$, dominate the $\phi$ and $\Omega$ production.

The model expectations from Hwa and Yang [58] for the most central $\Omega$ and $\phi$ $p_T$ spectra are compared to the data in Fig. 4.14. The dashed curves show the $T_sT_sT_s$ and $T_sT_s$ model contributions alone and the solid curves show the sum of all the model contributions. The sum lies on top of the thermal contributions for both particles, highlighting the dominance of recombination of thermal $s$ quarks to particle production in this framework. (The other model contributions are not shown.) One can see from both panels of Fig. 4.14 that the model shape agrees very well with the experimental values over the measured $p_T$ range for both particles.

The resulting $N(\Omega)/N(\phi)$ ratio obtained from the model is compared to the data in Fig. 4.15. The thermal $(T_sT_sT_s)/(T_sT_s)$ component is shown by the dashed line which increases monotonically over the $p_T$ range of the plot and the solid line represents the sum of all contributions. The model agrees well with the trend of the data up to $p_T \sim 4$ GeV/$c$ which covers $\sim$95% of the total yields for the $\Omega$ and $\phi$. In the context of this model, this implies that the production of these particles in central Au+Au collisions is predominantly through the recombination of thermal $s$ quarks. For $p_T > 4$ GeV/$c$, the model diverges from the data which may imply that the contribution from fragmentation or other mechanisms is larger than expected by the model in

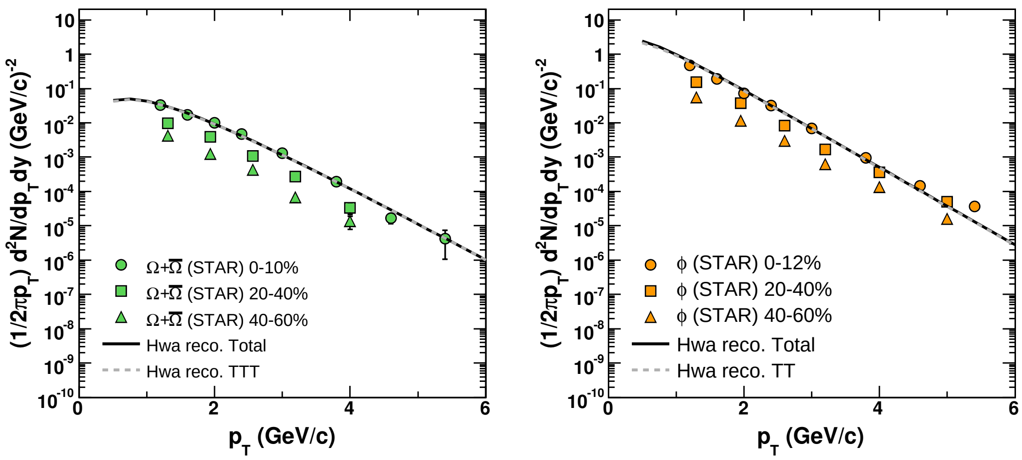


**Figure 4.14**: **Left panel:** $\Omega$ $p_T$ spectra for 0-10% [22], 20-40% and 40-60% [96] central Au+Au collisions at $\sqrt{s_{NN}}$ = 200 GeV/$c$ from the STAR experiment compared to recombination model curves for central collisions by Hwa et al. [58]. **Right panel:** $\phi$-meson $p_T$ spectra for 0-12%, 20-40%, 40-60% central Au+Au collisions compared to recombination model curves by Hwa et al. [58]. In both panels, the solid line represents the sum of all model contributions and the dashed line represents the contribution from thermal-thermal-thermal(TT) or thermal-thermal (TT) recombination for $\Omega$ and $\phi$ respectively.

this $p_T$ region.

### 4.4.2 Comparison of $N(\Omega)/N(\phi)$ ratio to other baryon/meson ratios

In Fig. 4.16 the central $N(\Omega)/N(\phi)$ ratio is compared to the central ratios of $N(p)/N(\pi^+)$ [36] and $N(\Lambda)/N(K_S^0)$ [35]. All three particle ratios exhibit a similar trend by increasing from low $p_T$, reaching a maximum and turning over at intermediate $p_T$ and decreasing towards higher $p_T$. It is also of note that the turning point of the ratios seems to shift to higher $p_T$ with increasing strangeness content of the measured particles i.e. the $N(p)/N(\pi^+)$ ratio turns over first while the $N(\Omega)/N(\phi)$ ratio has the highest $p_T$ value for its turn-over.

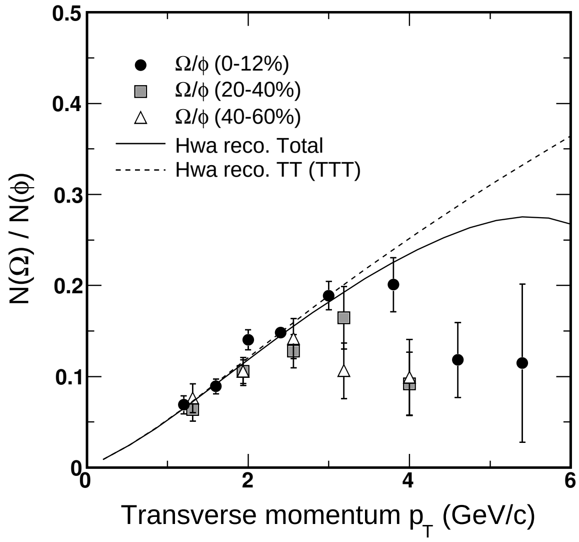


**Figure 4.15**: $N(\Omega)/N(\phi)$ ratios for 0-12% (circles), 20-40% (squares) and 40-60% (triangles) central collisions. The solid line represents the sum of the recombination model contributions for central collisions only. The dashed line represents the recombination model contribution for thermal-thermal-thermal [TTT]($\Omega$) / thermal-thermal [TT]($\phi$) production.

Also shown in Fig. 4.16 are the recombination model curves from Hwa et al. [58, 105] for the different particle types. In all cases the model gives the correct maximum value for the ratios but the turning points are consistently at higher $p_T$ than observed in the data.

## 4.5 Discussion

From the presented results, one may be able to infer various properties of the system created in Au+Au collisions at RHIC.

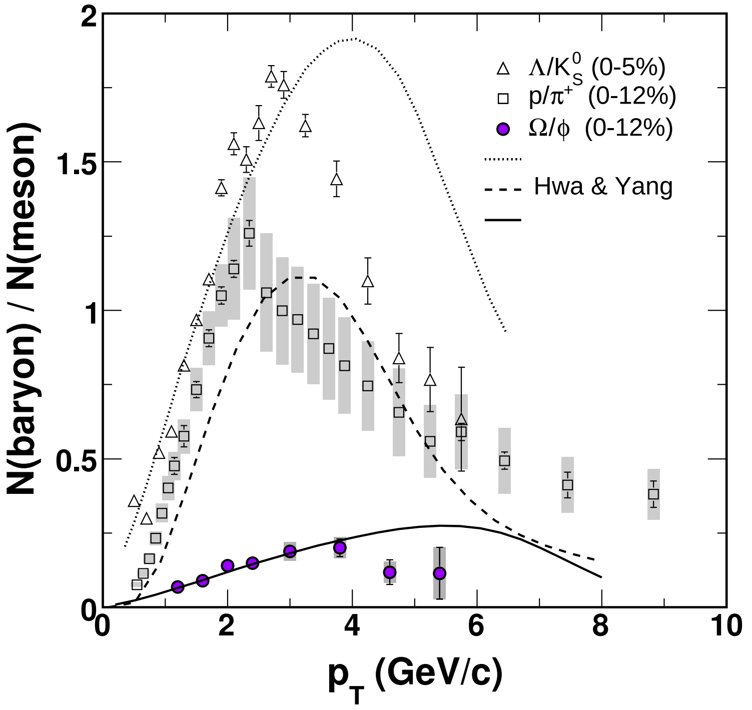


**Figure 4.16**: $N$(baryon)/$N$(meson) ratios vs. $p_T$ for central collisions for $\Lambda/K^0_S$ (triangles), p/$\pi^+$ (squares) and $\Omega/\phi$ (circles). The error bars represent the statistical errors and the shaded bands represent the systematic errors. All curves are recombination model expectations from Hwa et al. [58, 105].

### A sensitive probe

The hypothesis that the $\phi$ can be used as a probe, sensitive to the early stages of the system's evolution, is supported by the $\langle p_T\rangle$ results and the values for $T_{fo}$ vs. $\langle\beta\rangle$ extracted from blastwave fits to the $\phi$-meson $p_T$ spectra. The relatively small increase from peripheral to mid-peripheral centralities and the subsequent saturation of the $\langle p_T\rangle$ values up to central collisions compared to the continuous increase with centrality for the $\pi$, $K$ and $\bar{p}$, implies that the $\phi$ suffers fewer rescatterings in the hadronic stage, i.e. it freezes out earlier and therefore retains information from the early stage. The blastwave fit to the central $p_T$ spectrum returns values for the $T_{fo}$ and $\langle\beta\rangle$ which also imply that relative to $\pi$, $K$, $p$, the $\phi$-meson freezes out with a lower velocity and at a higher temperature for corresponding centrality bins i.e. at an earlier time when the system was hotter.

**Probing partonic collectivity and deconfinement**

As discussed in section 1.3.4, the elliptic flow $v_2$ is an observable built up at an early stage of the system's evolution. Interactions between the medium constituents result in the transformation of the initial spatial anisotropy of the nuclear overlap area into a momentum-space anisotropy. In addition to measurements of $v_2(p_T)$ for the multistrange $\Xi$ and $\Omega$ baryons [59], and given that the hidden strange $(s\bar{s})$ $\phi$-meson is not expected to interact much in the hadronic stage, the $v_2(p_T)$ results being comparable to that of other identified particles consisting of the lighter $u$ and $d$ quarks is strong evidence for the partonic collectivity of the system in the early stage. In addition, the quark number scaling in $v_2(p_T)$ observed for identified particles such as $\Lambda$, p, $K^0_S$ and $K^{\pm}$ [33, 43] has now also been observed for the $\phi$-meson. The scaling with quark number implies that during the time when the $v_2$ signal was built up, the system was in a state of deconfinement.

The increasing trend of the $\langle v_2 \rangle / \epsilon$ results for the identified particles and charged hadrons with increasing centrality may also imply that there is greater collectivity in the system created in central collisions compared to peripheral collisions at RHIC.

The quark number scaling observed in $v_2$ measurements at intermediate $p_T$ has also been seen in the measurement of the $\phi$-meson nuclear modification factor, $R_{CP}$ for (0-5%/40-80%). This result helps to confirm that the splitting in $R_{CP}$ for different identified particles is a baryon-meson effect rather than a mass-type effect since the $\phi$ scales like the $K^0_S$ despite its mass being very similar to that of the $\Lambda$ and proton.

**Probing particle production mechanisms**

Scaling of $v_2$ and $R_{CP}$ with number of constituent or valence quarks is a direct expectation of models of particle production involving recombination or coalescence of quarks [34, 39, 94]. In section 4.4.1 the expectations from three recombination models were compared to the $\phi$-meson $p_T$ spectra. Two of the models, Model 1 by Fries et al. [34] and Model 3 by Hwa and Yang [58], which each assume an underlying exponential (thermal) distribution of strange quarks from which the $\phi$ (and $\Omega$ baryon) is formed via quark coalesence, reproduce the shape of the central $\phi$-meson $p_T$ spectrum well up to $p_T \sim 4$ GeV/$c$. Note that although Model 3 also includes contributions from thermal-shower and shower-shower recombination, these contributions are suppressed by orders of magnitude with respect to the thermal-thermal contribution to $\phi$-meson production. We do not comment here on the absolute normalization of the model curves since they are fixed by fitting to data. The last model, Model 2 by Chen and Ko [98], which used the AMPT model to provide the underlying parton distribution, did not reproduce the shape of the $\phi$ $p_T$ spectra.

In order to further test the assumption in Models 1 and 3 of $\phi$-mesons being formed via recombination of thermal $s$ quarks, the model expectations were compared to the $N(\Omega)/N(\phi)$ ratios vs. $p_T$ as a function of centrality. In the case of Model 1, the model normalization for the $\Omega$ spectra is not in agreement with data (over-estimated), and therefore the model expectation for the $N(\Omega)/N(\phi)$ ratio is far above the data. However, upon rescaling the model curve for the central $\Omega$ spectrum by a constant factor of $\pi$, the resulting model ratio matches the central $N(\Omega)/N(\phi)$ ratio well up to $p_T \sim 4$ GeV/$c$. The expectation for $N(\Omega)/N(\phi)$ from Model 3, which is for central collisions only, is consistent with the data up to $p_T \sim 4$ GeV/$c$. For $p_T > 4$ GeV/$c$, the model curves diverge from the data: Model 1 expects an increase up to at least 6 GeV/$c$ while Model 3 expects a turnover around 5.5 GeV/$c$ which is at higher $p_T$ than observed in the data. This implies that the contributions from other mechanisms, for example fragmentation, to particle production are different to the model expectations for $p_T > 4$ GeV/$c$. However, the $p_T$ range $p_T < 4$ GeV/$c$, covers more than 95% of the $\Omega$ and $\phi$ yields and therefore, within the framework of the models [34, 58], the majority of multistrange hadrons would be formed through the coalescence of thermal $s$ quarks in central Au+Au collisions at RHIC.

In the measured data, the shift to higher $p_T$ values for the turning points of the $N(\Omega)/N(\phi)$ ratios with increasing centrality may imply that the contribution to $\phi$ and $\Omega$ production from thermal $s$ quarks is larger in central compared to peripheral collisions. This idea is supported by the evolution in the shape of the $\phi$-meson $p_T$ spectra which are exponential-like for central collisions but smoothly evolve to be more power-law-like (i.e. the better fit of the Levy function) for more peripheral collisions. The shift towards higher $p_T$ in the position of the turning points of the baryon/meson ratios with increasing strangeness content of the particles, may imply that there are different production mechanisms for strangeness compared to the lighter $u$ and $d$ flavours.

# Chapter 5

# Conclusion and Outlook

## 5.1 Conclusions

In summary, the work of this thesis has been to measure $\phi$-meson production and elliptic flow, $v_2$, with the aim of learning more about the characteristics of the medium created in Au+Au collisions at RHIC.

The $\phi$-meson invariant yields both integrated, and as a function of $p_T$, have been measured in Au+Au collisions at $\sqrt{s_{NN}} = 200$ GeV over a wide range of centralities using the STAR detector. The evolution in the shape of the transverse momentum distributions from exponential-like in the most central collisions to power-law-like in peripheral collisions indicates a change in the relative contributions from competing particle production mechanisms over the range in collision centrality. The exponential shape of the most central $p_T$ spectrum implies a smaller relative contribution to particle production from hard (pQCD) processes compared to the case in more peripheral collisions.

The $\langle p_T \rangle$ of the $\phi$ has been measured for narrower, as well as a larger number of centrality intervals than before and shows a shallow increase from the p+p values to Au+Au collisions. The $\langle p_T \rangle$ values seem to saturate at more peripheral centralities than for the $\bar{p}$. The shallow increase and flatter shape of the $\phi$ $\langle p_T \rangle$ distribution vs. centrality compared to $\pi$, $K$ and $\bar{p}$ may imply that the $\phi$-meson is less affected by hadronic rescattering and freezes out earlier than the other particles.

Nuclear modification factor, $R_{CP}$, measurements for two different choices of peripheral centrality bin show that the production of $\phi$-mesons, scaled by the corresponding number of binary collisions, is suppressed in central compared to more peripheral collisions. For the $R_{CP}$ result obtained using the centrality bins (0-5%)/(40-60%), the $\phi$-meson measurement is similar to the $K_S^0$ and is consistent with meson-scaling, providing further confirmation that the splitting of particles into bands in the $R_{CP}$ is dependent on particle type (i.e. baryon vs. meson) rather than particle mass. For a more peripheral denominator bin i.e. (0-5%)/(60-80%), the $\phi$-meson $R_{CP}$ seems to fall in between the trends for the $K_S^0$ and the $\Lambda$ and does not follow the scaling observed for (0-5%)/(40-60%). The reason is still an open issue but is likely to rely to some extent on a relative difference in the dominant particle production mechanisms for the different particle species as a function of changing centrality.

The centrality dependence of the $\phi$-meson $p_T$ spectra and the $N(\Omega)/N(\phi)$ ratios were compared to expectations from three models of particle production based on quark recombination [34, 58, 98]. The model in [58], which expects that the production of multistrange particles in central collisions is predominantly through the recombination of thermal $s$-quarks, describes the central $\phi$ and $\Omega$ spectra well and is consistent with the central $N(\Omega)/N(\phi)$ ratio for $p_T \lesssim 4$ GeV/$c$ which covers more than 95% of the particle yields.

The $\phi$-meson differential elliptic flow $v_2(p_T)$ was measured in miminum bias Au+Au collisions at two different energies: $\sqrt{s_{NN}} = 62.4$ GeV and 200 GeV. At both collision energies the $\phi$-meson exhibits a significant amount of elliptic flow which is comparable to that of particles consisting of the lighter $u$ and $d$ quarks. The applicability of a new measurement technique, the $v_2$ vs. $m_{inv}$ method [81], was shown using the 62 GeV dataset through the consistency in the results obtained with this method compared to the established $\phi$-binning method which has been used previously for identified particle $v_2$ studies. Within the statistical and systematic uncertainties, the

$v_2(p_T)$ results for the two energies are consistent with each other.

For 200 GeV Au+Au collisions, the minimum bias $v_2(p_T)$ results at low $p_T$ ($< 2$ GeV/$c$) are consistent with a mass ordering trend and hydrodynamical expectations. At intermediate $p_T$ ($2 < p_T < 5$ GeV/$c$), the hidden strange $\phi$-meson $v_2(p_T)$ is comparable to that of particles composed of the lighter $u$ and $d$ quarks and is also consistent with number of quark=2 scaling. This strongly implies that there are a significant number of interactions between quarks at the partonic stage and is therefore strong evidence for partonic collectivity and deconfinement of the medium created in Au+Au collisions at RHIC.

The centrality dependence of the $\phi$-meson $v_2(p_T)$ has also been measured for the first time. The results show a decrease with increasing centrality as expected from the decreasing eccentricity in the initial nuclear overlap shape. The $v_2(p_T)$ results for the $\phi$ and other identified particles ($K_S^0$, $\Lambda$, $\Xi$) were integrated over $p_T$ to obtain the $\langle v_2 \rangle$ vs. centrality. The trend is the same as for $v_2(p_T)$: a decrease with centrality for all the identified particles which is consistent with previously measured results for the charged hadrons measured by STAR. Dividing by the average eccentricity, $\epsilon_{part}$, of the system created in collisions in the studied centrality ranges, as a means of removing the observable's dependence on the intial system geometry, the trend is reversed: $\langle v_2 \rangle / \epsilon_{part}$ increases with centrality for the identified particles and charged hadrons. This may imply that there is greater collectivity in the system created in central Au+Au collisions compared to peripheral collisions. Hydrodynamic calculations for $K_S^0$, $\Lambda$, and $\Xi$ [89, 93] for the same quantity are relatively constant vs. centrality. The model and data are consistent within the errors for the most central collisions which also supports the idea of partonic collectivity (and possible thermalization) of the medium created in Au+Au collisions at $\sqrt{s_{NN}} = 200$ GeV.

## 5.2 Future Directions

In addition to the measurements which have been made to date of the $\phi$-meson at RHIC, there are yet further interesting aspects to study in the future which may help to provide further information about the system created in ultrarelativistic nucleus-nucleus collisions.

Previous studies of the $\phi$-meson for RHIC data [57, 60, 106] have measured $\phi$ production via its decay to charged kaons. Studies of $\phi$ production via measurements of the di-electron decay channel $\phi \rightarrow e^+e^-$ (branching ratio $= 2.97 \times 10^{-4}$) and comparison to current measurements may help to disentangle contributions from hadronic rescattering. While kaons can undergo recatterings in the hadronic stage which may distort the $\phi$ signal, electrons do not interact strongly. Therefore $\phi$-mesons reconstructed through this channel may provide information, undiluted by subsequent hadronic interactions, from the early stages of the system's evolution. For example, possible in-medium mass modifications [107] of the $\phi$ might be probed through the di-electron channel.

Due to the several orders of magnitude suppression in the branching ratio and within the current statistics and particle identification capabilities of the STAR TPC, the resulting large combinatorial backgrounds have to date not allowed the extraction of a $\phi$-meson signal in the di-electron channel. Studies of the $\phi$ via the di-electron channel have been made by the PHENIX experiment [108] and compared to the kaon channel measurements, but the statistical and systematic errors are too large for definitive conclusions to be drawn. Further studies in this direction will rely on detector upgrades for both the STAR and PHENIX experiments. PHENIX plans to install a hadron-blind detector to improve di-electron measurements. The STAR upgraded Time-Of-Flight detector will provide improved electron identification capabilities over the full azimuthal range.

In addition to different decay channel measurements, there are measurements of different observables to be made using the $\phi$-meson in Au+Au collisions at RHIC. For example, recent measurements of angular correlations using the multistrange $\Omega$ baryon as a trigger particle [109] have challenged expectations for particle production in the context of recombination models [58]. Since, in the framework of this model, $\phi$ and $\Omega$ production from jet fragmentation is suppressed, it is expected that there should be no angular correlation of particles with respect to one of these particles used as a trigger particle. In contrast, the $\Omega$ studies by STAR [109] suggest that a correlation may have been observed and similar future measurements for the $\phi$ may provide additional insights.

**From strangeness to charm**

The measurements of the $\phi$-meson elliptic flow at RHIC and its scaling with number of constituent quarks like the particles composed of the lighter $u$ and $d$ quarks, provides strong evidence for partonic collectivity of the medium created at RHIC. The question of whether the matter created in Au+Au collisions is thermalized might be answered in the future by $v_2$ measurements for particles containing the even heavier $c$ quark. Even inside the QGP, if chiral symmetry is restored, the charm quark remains heavy (due to its coupling to the Higgs field [110]) while the lighter flavours obtain their small current quark masses. Therefore, if the heavy $c$ quark is observed to flow, this implies multiple interactions at the partonic level, which means that the light quarks are likely to be thermalized [111]. Direct measurements of charmed particle $v_2$ are the ideal probe of charm flow. Tracking detector upgrades are planned for the STAR and PHENIX experiments to enable the direct reconstruction of $D$-mesons through their displaced decay vertices. In addition, $v_2$ measurements for the charm-analogue to the $\phi$, the hidden charm meson, $J/\psi$ ($c\bar{c}$), would be ideal in helping to provide a more definitive answer to the question of thermalization of the medium created in ultra-relativistic nucleus-nucleus collisions at RHIC.

# Appendix A

# Data Tables

## A.1 $p_T$ Spectra

| Centrality: 0–5% | | | |
|---|---|---|---|
| $p_T$ **(GeV/$c$)** | **Invariant yield** (GeV/c)$^{-2}$ | **± (stat.)** | **± (sys)** |
| 0.4 – 0.5 | 2.35e+00 | 2.54e–01 | 5.37e–01 |
| 0.5 – 0.6 | 1.74e+00 | 1.18e–01 | 5.21e–01 |
| 0.6 – 0.7 | 1.43e+00 | 6.87e–02 | 3.28e–01 |
| 0.7 – 0.8 | 1.19e+00 | 4.72e–02 | 2.63e–01 |
| 0.8 – 1.0 | 9.71e–01 | 2.46e–02 | 2.14e–01 |
| 1.0 – 1.2 | 6.88e–01 | 1.91e–02 | 1.45e–01 |
| 1.2 – 1.5 | 3.68e–01 | 1.17e–02 | 7.80e–02 |
| 1.5 – 1.8 | 1.98e–01 | 8.28e–03 | 4.27e–02 |
| 1.8 – 2.2 | 7.79e–02 | 3.84e–03 | 1.75e–02 |
| 2.2 – 2.6 | 3.55e–02 | 2.01e–03 | 7.61e–03 |
| 2.6 – 3.0 | 1.29e–02 | 9.71e–04 | 3.09e–03 |
| 3.0 – 3.5 | 3.21e–03 | 3.01e–04 | 1.18e–03 |
| 3.5 – 4.0 | 1.07e–03 | 1.57e–04 | 2.26e–04 |
| 4.0 – 5.0 | 1.70e–04 | 2.62e–05 | 3.68e–05 |

**Table A.1**: Invariant yields for $\phi$ for 0-5% central Au+Au collisions.

| Centrality: 0–10% | | | |
|---|---|---|---|
| $p_T$ **(GeV/$c$)** | **Invariant yield** $(\mathrm{GeV/c})^{-2}$ | **± (stat.)** | **± (sys)** |
| 0.4 – 0.5 | 1.61e+00 | 2.69e–01 | 2.13e–01 |
| 0.5 – 0.6 | 1.69e+00 | 1.80e–01 | 2.51e–01 |
| 0.6 – 0.7 | 1.49e+00 | 1.04e–01 | 2.49e–01 |
| 0.7 – 0.8 | 1.08e+00 | 6.84e–02 | 1.68e–01 |
| 0.8 – 1.0 | 9.77e–01 | 3.99e–02 | 1.31e–01 |
| 1.0 – 1.2 | 6.28e–01 | 3.10e–02 | 8.27e–02 |
| 1.2 – 1.5 | 3.58e–01 | 2.10e–02 | 4.67e–02 |
| 1.5 – 1.8 | 1.76e–01 | 1.39e–02 | 3.14e–02 |
| 1.8 – 2.2 | 7.47e–02 | 6.70e–03 | 1.10e–02 |
| 2.2 – 2.6 | 2.91e–02 | 3.26e–03 | 5.60e–03 |
| 2.6 – 3.0 | 1.16e–02 | 2.30e–03 | 4.19e–03 |
| 3.0 – 3.5 | 3.57e–03 | 6.15e–04 | 1.41e–03 |
| 3.5 – 4.0 | 7.88e–04 | 1.58e–04 | 1.76e–04 |
| 4.0 – 5.0 | 2.05e–04 | 7.18e–05 | 5.68e–05 |

**Table A.2**: Invariant yields for $\phi$ for 0-10% central Au+Au collisions.

| Centrality: 10–20% | | | |
|---|---|---|---|
| $p_T$ **(GeV/$c$)** | **Invariant yield** $(\mathrm{GeV/c})^{-2}$ | **± (stat.)** | **± (sys)** |
| 0.4 – 0.5 | 1.31e+00 | 2.36e–01 | 5.01e–01 |
| 0.5 – 0.6 | 1.09e+00 | 1.29e–01 | 4.29e–01 |
| 0.6 – 0.7 | 9.72e–01 | 6.99e–02 | 1.22e–01 |
| 0.7 – 0.8 | 7.45e–01 | 4.52e–02 | 8.83e–02 |
| 0.8 – 1.0 | 6.40e–01 | 2.52e–02 | 8.16e–02 |
| 1.0 – 1.2 | 4.69e–01 | 2.07e–02 | 6.37e–02 |
| 1.2 – 1.5 | 2.68e–01 | 1.41e–02 | 2.97e–02 |
| 1.5 – 1.8 | 1.03e–01 | 8.35e–03 | 1.34e–02 |
| 1.8 – 2.2 | 5.72e–02 | 4.56e–03 | 9.50e–03 |
| 2.2 – 2.6 | 2.25e–02 | 2.30e–03 | 4.80e–03 |
| 2.6 – 3.0 | 7.21e–03 | 9.86e–04 | 1.42e–03 |
| 3.0 – 3.5 | 3.24e–03 | 5.24e–04 | 1.06e–03 |
| 3.5 – 4.0 | 7.60e–04 | 1.05e–04 | 1.52e–04 |
| 4.0 – 5.0 | 1.66e–04 | 3.63e–05 | 3.02e–05 |

**Table A.3**: Invariant yields for $\phi$ for 10-20% central Au+Au collisions.

| Centrality: 20–30% | | | |
|---|---|---|---|
| $p_T$ **(GeV/$c$)** | **Invariant yield** (GeV/c)$^{-2}$ | **± (stat.)** | **± (sys)** |
| 0.4 – 0.5 | 9.70e–01 | 1.40e–01 | 2.76e–01 |
| 0.5 – 0.6 | 7.38e–01 | 7.55e–02 | 9.80e–02 |
| 0.6 – 0.7 | 6.94e–01 | 5.31e–02 | 1.03e–01 |
| 0.7 – 0.8 | 5.47e–01 | 3.19e–02 | 7.05e–02 |
| 0.8 – 1.0 | 4.04e–01 | 1.53e–02 | 5.25e–02 |
| 1.0 – 1.2 | 2.99e–01 | 1.27e–02 | 3.76e–02 |
| 1.2 – 1.5 | 1.50e–01 | 8.13e–03 | 2.04e–02 |
| 1.5 – 1.8 | 8.73e–02 | 6.59e–03 | 1.06e–02 |
| 1.8 – 2.2 | 4.11e–02 | 3.58e–03 | 5.19e–03 |
| 2.2 – 2.6 | 1.68e–02 | 1.77e–03 | 4.23e–03 |
| 2.6 – 3.0 | 6.10e–03 | 8.58e–04 | 7.76e–04 |
| 3.0 – 3.5 | 1.85e–03 | 2.70e–04 | 3.13e–04 |
| 3.5 – 4.0 | 6.06e–04 | 1.23e–04 | 8.81e–05 |
| 4.0 – 5.0 | 2.14e–04 | 3.27e–05 | 6.33e–05 |

**Table A.4**: Invariant yields for $\phi$ for 20-30% central Au+Au collisions.

| Centrality: 30–40% | | | |
|---|---|---|---|
| $p_T$ **(GeV/$c$)** | **Invariant yield** (GeV/c)$^{-2}$ | **± (stat.)** | **± (sys)** |
| 0.4 – 0.5 | 7.55e–01 | 1.27e–01 | 1.68e–01 |
| 0.5 – 0.6 | 4.65e–01 | 4.62e–02 | 8.27e–02 |
| 0.6 – 0.7 | 3.80e–01 | 2.73e–02 | 7.84e–02 |
| 0.7 – 0.8 | 3.51e–01 | 2.16e–02 | 6.04e–02 |
| 0.8 – 1.0 | 2.53e–01 | 9.83e–03 | 4.05e–02 |
| 1.0 – 1.2 | 2.05e–01 | 8.79e–03 | 3.16e–02 |
| 1.2 – 1.5 | 1.05e–01 | 5.58e–03 | 1.60e–02 |
| 1.5 – 1.8 | 5.39e–02 | 4.01e–03 | 9.30e–03 |
| 1.8 – 2.2 | 2.61e–02 | 2.34e–03 | 4.46e–03 |
| 2.2 – 2.6 | 9.20e–03 | 9.06e–04 | 1.38e–03 |
| 2.6 – 3.0 | 3.67e–03 | 5.26e–04 | 7.34e–04 |
| 3.0 – 3.5 | 1.36e–03 | 1.79e–04 | 2.06e–04 |
| 3.5 – 4.0 | 3.68e–04 | 5.73e–05 | 6.77e–05 |
| 4.0 – 5.0 | 1.04e–04 | 2.00e–05 | 3.19e–05 |

**Table A.5**: Invariant yields for $\phi$ for 30-40% central Au+Au collisions.

| Centrality: 40–50% | | | |
|---|---|---|---|
| $p_T$ **(GeV/$c$)** | **Invariant yield** (GeV/c)$^{-2}$ | **± (stat.)** | **± (sys)** |
| 0.4 – 0.5 | 4.49e–01 | 7.97e–02 | 7.20e–02 |
| 0.5 – 0.6 | 2.98e–01 | 3.06e–02 | 4.68e–02 |
| 0.6 – 0.7 | 2.75e–01 | 2.26e–02 | 5.03e–02 |
| 0.7 – 0.8 | 2.54e–01 | 1.65e–02 | 4.53e–02 |
| 0.8 – 1.0 | 1.63e–01 | 6.60e–03 | 2.13e–02 |
| 1.0 – 1.2 | 1.25e–01 | 5.78e–03 | 1.64e–02 |
| 1.2 – 1.5 | 5.71e–02 | 3.14e–03 | 7.61e–03 |
| 1.5 – 1.8 | 3.15e–02 | 2.80e–03 | 5.64e–03 |
| 1.8 – 2.2 | 1.26e–02 | 1.20e–03 | 2.07e–03 |
| 2.2 – 2.6 | 6.77e–03 | 6.69e–04 | 8.85e–04 |
| 2.6 – 3.0 | 1.81e–03 | 2.53e–04 | 2.36e–04 |
| 3.0 – 3.5 | 6.65e–04 | 1.01e–04 | 1.39e–04 |
| 3.5 – 4.0 | 2.11e–04 | 3.62e–05 | 2.78e–05 |
| 4.0 – 5.0 | 6.11e–05 | 1.05e–05 | 8.54e–06 |

**Table A.6**: Invariant yields for $\phi$ for 40-50% central Au+Au collisions.

| Centrality: 50–60% | | | |
|---|---|---|---|
| $p_T$ **(GeV/$c$)** | **Invariant yield** (GeV/c)$^{-2}$ | **± (stat.)** | **± (sys)** |
| 0.4 – 0.5 | 2.58e–01 | 4.67e–02 | 3.64e–02 |
| 0.5 – 0.6 | 2.50e–01 | 2.81e–02 | 3.70e–02 |
| 0.6 – 0.7 | 1.70e–01 | 1.44e–02 | 2.19e–02 |
| 0.7 – 0.8 | 1.46e–01 | 1.02e–02 | 2.07e–02 |
| 0.8 – 1.0 | 9.17e–02 | 4.15e–03 | 1.11e–02 |
| 1.0 – 1.2 | 5.75e–02 | 2.95e–03 | 7.69e–03 |
| 1.2 – 1.5 | 3.30e–02 | 1.98e–03 | 4.98e–03 |
| 1.5 – 1.8 | 1.43e–02 | 1.39e–03 | 1.72e–03 |
| 1.8 – 2.2 | 6.86e–03 | 7.30e–04 | 8.34e–04 |
| 2.2 – 2.6 | 2.90e–03 | 3.16e–04 | 4.16e–04 |
| 2.6 – 3.0 | 1.14e–03 | 1.41e–04 | 1.42e–04 |
| 3.0 – 3.5 | 3.84e–04 | 5.73e–05 | 5.23e–05 |
| 3.5 – 4.0 | 1.55e–04 | 2.74e–05 | 3.20e–05 |
| 4.0 – 5.0 | 4.40e–05 | 7.08e–06 | 1.07e–05 |

**Table A.7**: Invariant yields for $\phi$ for 50-60% central Au+Au collisions.

| Centrality: 60–70% | | | |
|---|---|---|---|
| $p_T$ **(GeV/**$c$**)** | **Invariant yield** (GeV/c)$^{-2}$ | $\pm$ **(stat.)** | $\pm$ **(sys)** |
| 0.4 – 0.5 | 1.52e–01 | 3.58e–02 | 2.20e–02 |
| 0.5 – 0.6 | 9.51e–02 | 1.29e–02 | 1.13e–02 |
| 0.6 – 0.7 | 8.36e–02 | 8.68e–03 | 1.06e–02 |
| 0.7 – 0.8 | 7.85e–02 | 6.77e–03 | 8.86e–03 |
| 0.8 – 1.0 | 5.02e–02 | 2.88e–03 | 5.54e–03 |
| 1.0 – 1.2 | 3.18e–02 | 1.96e–03 | 3.53e–03 |
| 1.2 – 1.5 | 1.68e–02 | 1.31e–03 | 2.47e–03 |
| 1.5 – 1.8 | 7.00e–03 | 8.06e–04 | 1.77e–03 |
| 1.8 – 2.2 | 3.10e–03 | 3.73e–04 | 4.44e–04 |
| 2.2 – 2.6 | 1.49e–03 | 2.43e–04 | 3.41e–04 |
| 2.6 – 3.0 | 4.47e–04 | 7.25e–05 | 6.37e–05 |
| 3.0 – 3.5 | 2.27e–04 | 3.07e–05 | 2.68e–05 |
| 3.5 – 4.0 | 7.22e–05 | 1.44e–05 | 8.22e–06 |
| 4.0 – 5.0 | 1.86e–05 | 3.48e–06 | 2.65e–06 |

**Table A.8**: Invariant yields for $\phi$ for 60-70% central Au+Au collisions.

| Centrality: 70–80% | | | |
|---|---|---|---|
| $p_T$ **(GeV/**$c$**)** | **Invariant yield** (GeV/c)$^{-2}$ | $\pm$ **(stat.)** | $\pm$ **(sys)** |
| 0.4 – 0.5 | 6.14e–02 | 1.68e–02 | 9.62e–03 |
| 0.5 – 0.6 | 5.37e–02 | 1.03e–02 | 7.93e–03 |
| 0.6 – 0.7 | 4.49e–02 | 5.76e–03 | 6.53e–03 |
| 0.7 – 0.8 | 3.39e–02 | 4.02e–03 | 5.01e–03 |
| 0.8 – 1.0 | 2.28e–02 | 1.66e–03 | 3.44e–03 |
| 1.0 – 1.2 | 1.37e–02 | 1.10e–03 | 1.92e–03 |
| 1.2 – 1.5 | 7.01e–03 | 5.95e–04 | 1.09e–03 |
| 1.5 – 1.8 | 3.55e–03 | 4.75e–04 | 5.42e–04 |
| 1.8 – 2.2 | 1.29e–03 | 1.46e–04 | 2.22e–04 |
| 2.2 – 2.6 | 7.72e–04 | 1.08e–04 | 2.72e–04 |
| 2.6 – 3.0 | 1.92e–04 | 3.85e–05 | 6.48e–05 |
| 3.0 – 3.5 | 7.79e–05 | 2.00e–05 | 1.44e–05 |
| 3.5 – 4.0 | 1.70e–05 | 4.23e–06 | 2.55e–06 |
| 4.0 – 5.0 | 6.46e–06 | 1.91e–06 | 2.09e–06 |

**Table A.9**: Invariant yields for $\phi$ for 70-80% central Au+Au collisions.

## A.2 $v_2$ Results

| $\sqrt{s_{NN}}$ = 200 GeV | | | |
|---|---|---|---|
| $p_T$ (GeV/$c$) | $v_2$ | ± **(stat. err.)** | ± **(sys. err.)** |
| 0.5 – 1.0 | 0.03201 | 0.00966 | 0.00228 |
| 1.0 – 1.5 | 0.08354 | 0.00924 | 0.00872 |
| 1.5 – 2.0 | 0.11097 | 0.01580 | 0.02935 |
| 2.0 – 2.5 | 0.16466 | 0.02355 | 0.00752 |
| 2.5 – 3.0 | 0.16403 | 0.03484 | 0.01420 |
| 3.0 – 4.0 | 0.11122 | 0.03648 | 0.01937 |
| 4.0 – 5.0 | 0.12134 | 0.05603 | 0.01659 |
| $\sqrt{s_{NN}}$ = 62.4 GeV | | | |
| $p_T$ (GeV/$c$) | $v_2$ | ± **(stat. err.)** | ± **(sys. err.)** |
| 0.4 – 0.8 | 0.01814 | 0.01694 | 0.00636 |
| 0.8 – 1.2 | 0.08599 | 0.01641 | 0.03539 |
| 1.2 – 1.6 | 0.08267 | 0.02137 | 0.03703 |
| 1.6 – 2.0 | 0.07897 | 0.03774 | 0.03814 |
| 2.0 – 4.0 | 0.09303 | 0.03710 | 0.02154 |

**Table A.10**: Minimum bias $v_2$ results for the $\phi$-meson in Au+Au collisions at $\sqrt{s_{NN}}$ = 200 GeV and 62.4 GeV.

| 0-5% | | | |
|---|---|---|---|
| $p_T$ (GeV/$c$) | $v_2$ | ± **(stat. err.)** | ± **(sys. err.)** |
| 0.5 – 1.0 | -0.01399 | 0.01834 | 0.01553 |
| 1.0 – 1.5 | 0.06838 | 0.01641 | 0.01844 |
| 1.5 – 2.0 | 0.04271 | 0.02303 | 0.00932 |
| 2.0 – 3.0 | 0.04625 | 0.02956 | 0.02244 |
| 3.0 – 4.0 | 0.07802 | 0.06276 | 0.01334 |
| 4.0 – 5.0 | -0.04559 | 0.07776 | 0.02945 |

**Table A.11**: $\phi$-meson $v_2$ results obtained from 0-5% central-triggered data from Au+Au collisions at $\sqrt{s_{NN}}$ = 200 GeV.

| | 10-40% | | | 40-80% | | |
|---|---|---|---|---|---|---|
| $p_T$ (GeV/$c$) | $v_2$ | **± (stat.)** | **± (sys.)** | $v_2$ | **± (stat.)** | **± (sys.)** |
| 0.5 – 1.0 | 0.03818 | 0.01196 | 0.00944 | 0.08009 | 0.01363 | 0.00456 |
| 1.0 – 1.5 | 0.11075 | 0.01430 | 0.01544 | 0.11866 | 0.01969 | 0.01619 |
| 1.5 – 2.0 | 0.10462 | 0.02061 | 0.03101 | 0.13893 | 0.03037 | 0.03447 |
| 2.0 – 2.5 | 0.18516 | 0.02705 | 0.00849 | 0.16470 | 0.03736 | 0.00516 |
| 2.5 – 3.0 | 0.21093 | 0.03763 | 0.02189 | 0.26246 | 0.04574 | 0.02110 |
| 3.0 – 4.0 | 0.15884 | 0.04015 | 0.03923 | 0.22322 | 0.05030 | 0.00608 |
| 4.0 – 5.0 | 0.21446 | 0.04541 | 0.01221 | 0.22558 | 0.06960 | 0.03800 |

**Table A.12**: $\phi$-meson $v_2$ results from 10-40% and 40-80% central Au+Au collisions at $\sqrt{s_{NN}} = 200$ GeV.

| **Centrality** (%) | $\langle v_2 \rangle$ | **± (stat. err.)** | **± (sys. err.)** |
|---|---|---|---|
| 40-80 | 0.0870 | 0.0111 | 0.0002 |
| 10-40 | 0.0658 | 0.0082 | 0.0016 |
| 0-5 | 0.0210 | 0.0116 | 0.0050 |

**Table A.13**: $\langle v_2 \rangle$ for the $\phi$-meson for three centrality bins including the statistical and systematic errors.

| **Centrality** (%) | $\epsilon$ | $\langle v_2 \rangle/\epsilon$ | **± (stat. err.)** | **± (sys. err.)** |
|---|---|---|---|---|
| 40-80 | 0.485447 | 0.179 | 0.023 | 0.0004 |
| 10-40 | 0.261468 | 0.252 | 0.031 | 0.0061 |
| 0-5 | 0.0854 | 0.246 | 0.136 | 0.0580 |

**Table A.14**: $\langle v_2 \rangle/\epsilon$ obtained for the $\phi$-meson for three centrality bins including statistical and systemtatic errors. $\epsilon$ values are from [90].

## A.3 $N(\Omega)/N(\phi)$ Ratios

| Centrality: 0–12% | | | |
|---|---|---|---|
| $p_T$ (GeV/$c$) | $N(\Omega)/N(\phi)$ | ± **(stat.)** | ± **(sys.)** |
| 1.0 – 1.4 | 6.88e-02 | 9.93e-03 | 8.96e-03 |
| 1.4 – 1.8 | 8.92e-02 | 8.20e-03 | 6.83e-03 |
| 1.8 – 2.2 | 1.40e-01 | 1.11e-02 | 1.30e-02 |
| 2.2 – 2.6 | 1.48e-01 | 6.24e-03 | 8.80e-03 |
| 2.6 – 3.4 | 1.89e-01 | 1.56e-02 | 3.12e-02 |
| 3.4 – 4.2 | 2.01e-01 | 2.96e-02 | 3.57e-02 |
| 4.2 – 5.0 | 1.18e-01 | 4.12e-02 | 3.56e-02 |
| 5.0 – 5.8 | 1.15e-01 | 8.71e-02 | 8.84e-02 |

**Table A.15**: $N(\Omega)/N(\phi)$ ratio vs. $p_T$ for 0-12% central collisions.

| Centrality: 20–40% | | | |
|---|---|---|---|
| $p_T$ (GeV/$c$) | $N(\Omega)/N(\phi)$ | ± **(stat.)** | ± **(sys.)** |
| 1.0 – 1.6 | 6.36e-02 | 1.26e-02 | 1.77e-03 |
| 1.6 – 2.3 | 1.05e-01 | 1.30e-02 | 6.83e-03 |
| 2.3 – 2.9 | 1.28e-01 | 1.83e-02 | 1.64e-02 |
| 2.9 – 3.5 | 1.64e-01 | 3.43e-02 | 5.72e-03 |
| 3.5 – 4.5 | 9.19e-02 | 3.48e-02 | 1.85e-02 |

**Table A.16**: $N(\Omega)/N(\phi)$ ratio vs. $p_T$ for 20-40% central collisions.

| Centrality: 40–60% | | | |
|---|---|---|---|
| $p_T$ (GeV/$c$) | $N(\Omega)/N(\phi)$ | ± **(stat.)** | ± **(sys.)** |
| 1.0 – 1.6 | 7.59e-02 | 1.59e-02 | 6.75e-03 |
| 1.6 – 2.3 | 1.06e-01 | 1.55e-02 | 1.78e-02 |
| 2.3 – 2.9 | 1.42e-01 | 2.21e-02 | 3.15e-02 |
| 2.9 – 3.5 | 1.07e-01 | 3.04e-02 | 6.22e-03 |
| 3.5 – 4.5 | 9.90e-02 | 4.16e-02 | 1.66e-02 |

**Table A.17**: $N(\Omega)/N(\phi)$ ratio vs. $p_T$ for 40-60% central collisions.

# Appendix B

# $v_2$ Details

## B.1 $v_2$ Method Comparison

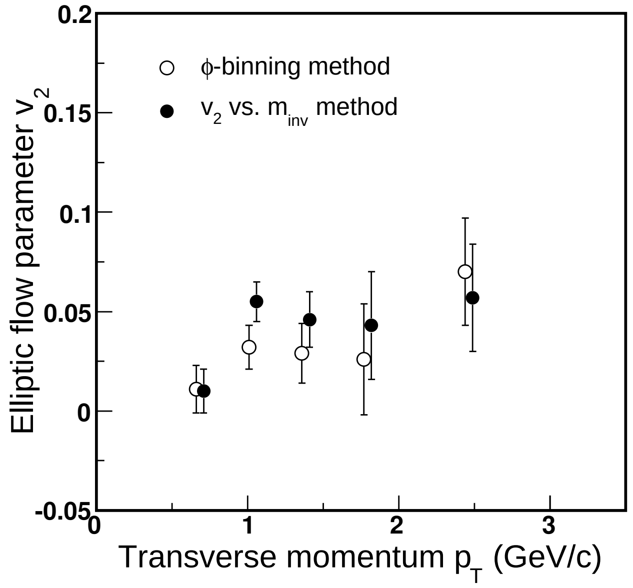


**Figure B.1**: Comparison of $v_2$ results (not corrected for event plane resolution effects) from the $\phi$-binning method (open circles) and the $v_2$ vs. $m_{inv}$ method (solid circles) for Au+Au collisions at $\sqrt{s_{NN}} = 62.4$ GeV. Data points offset for clarity. (Values are from Table 3.4).

## B.2 $v_2$ Systematics Details

### B.2.1 Variation in $S/(S+B)$ and $B/(S+B)$ ratios from extraction method

The $S/(S+B)$ and $B/(S+B)$ ratios are functions of $m_{inv}$ and were calculated in two ways to estimate the effect on the final extracted $v_2$ results.

In both cases, the signal distribution, $S(m_{inv})$, was obtained by subtracting the scaled mixed-event background $m_{inv}$ distribution from the same-event $m_{inv}$ distribution. The signal distribution was then fitted with a Breit-Wigner function plus a polynomial to describe the shape of the residual background. The residual background in the region of the $\phi$-meson mass peak, estimated by the polynomial function, was then further subtracted from the signal distribution and added into the scaled background distribution to find $B(m_{inv})$. In Fig. B.2, the blue histogram is the signal remaining after subtraction of the scaled mixed-event background. The Breit-Wigner + polynomial (first order) fit to the distribution is shown by the black lines. The green histogram is the resulting $S(m_{inv})$ distribution remaining after the residual background has been subtracted, in the region of the $\phi$ mass peak, from the blue histogram.

The $S/(S+B)$ and $B/(S+B)$ ratios were then obtained in two ways:

1. The $S(m_{inv})$ histogram was divided by the sum of the $S(m_{inv})$ and $B(m_{inv})$ histograms
2. $S(m_{inv})$ was taken from the Breit-Wigner fit function result and used in the ratio calculation

The $S/(S+B)$ and $B/(S+B)$ ratios obtained using the two methods are shown in Fig. B.3 and Fig. B.4 respectively for the case of 10-40% central 200 GeV Au+Au collisions and an arbitrary choice of $p_T$ bin.

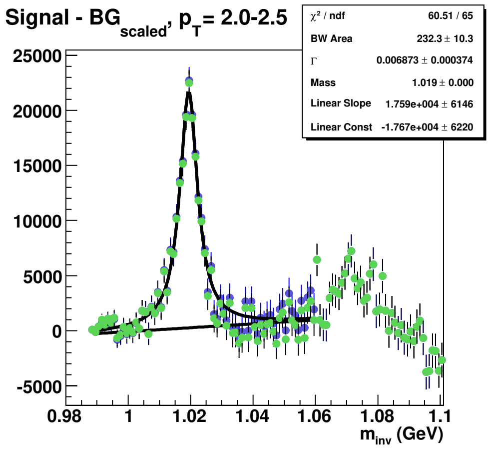


**Figure B.2**: The blue histogram is the signal remaining after subtraction of the scaled mixed-event background. The green histogram is the signal remaining ($S$) after the further subtraction of the residual background (quantified by the polynomial function) in the region of the $\phi$-meson mass peak.

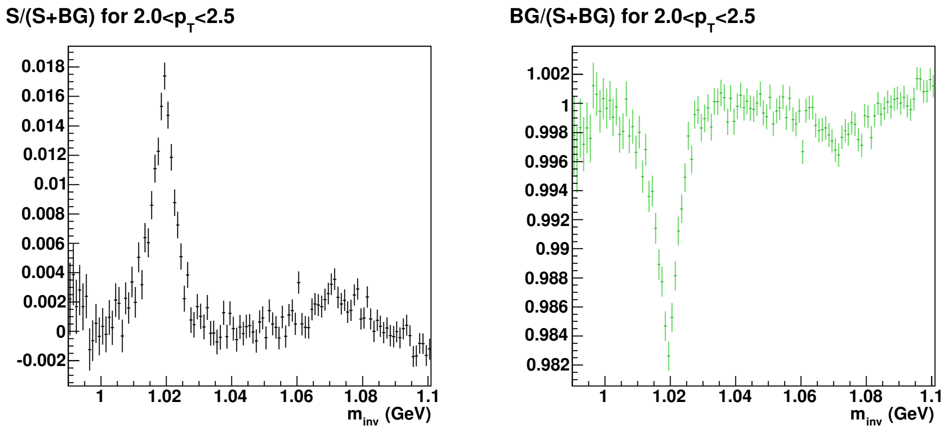


**Figure B.3**: $S/(S+B)$ and $B/(S+B)$ ratios obtained using the $S$ and $B$ $m_{inv}$ histograms.

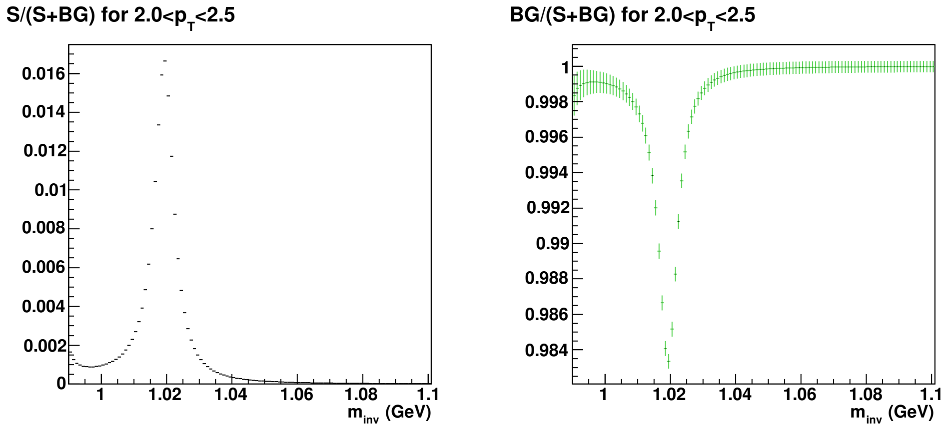


**Figure B.4**: $S/(S+B)$ and $B/(S+B)$ ratios obtained using $S$ from the Breit-Wigner function fit to the $m_{inv}$ distribution.

### B.2.2 Variation in $S/(S+B)$ and $B/(S+B)$ ratios when over- or under-estimating raw $\phi$ yield

The over- and under-estimates of the raw $\phi$-yields were made by fitting the background-subtracted signal $m_{inv}$ distribution with a Breit-Wigner function + second order polynomial and forcing the fit to return the Breit-Wigner area parameter to be 120% or 80% of the best fitted area value. The left and right panels of Fig. B.5 illustrate the resulting fit shapes for over- and under-estimating the raw $\phi$-meson yields for the same centrality and arbitrary choice of $p_T$ bin as discussed in the previous section. The blue and green histograms have the same meaning as in Fig. B.2.

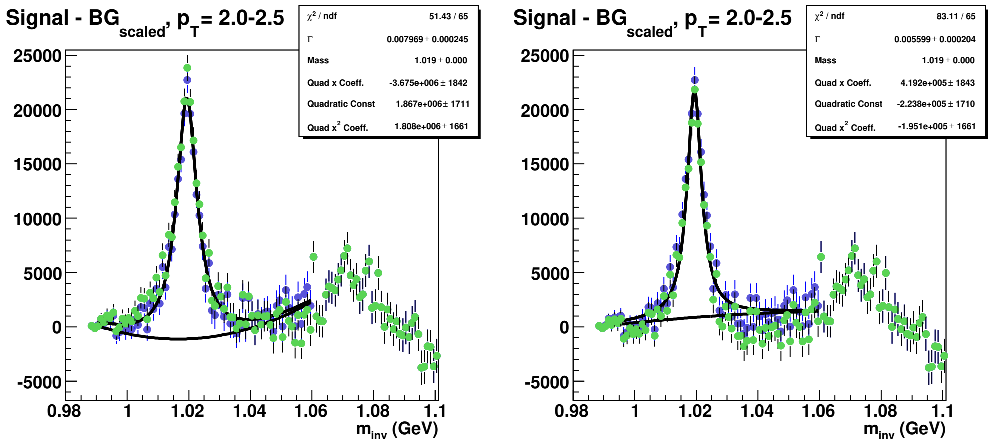


**Figure B.5**: **Left panel:** Breit-Wigner + second order polynomial with fit forced to return 120% (yield over-estimate) of best fit yield shown in Fig. B.2. **Right panel:** Breit-Wigner + second order polynomial with fit forced to return 80% (yield under-estimate) of best fit yield shown in Fig. B.2.

The resulting $S/(S+B)$ and $B/(S+B)$ ratios obtained from over and under-estimating the raw $\phi$ yield are presented in Fig. B.6 and Fig. B.7 respectively.

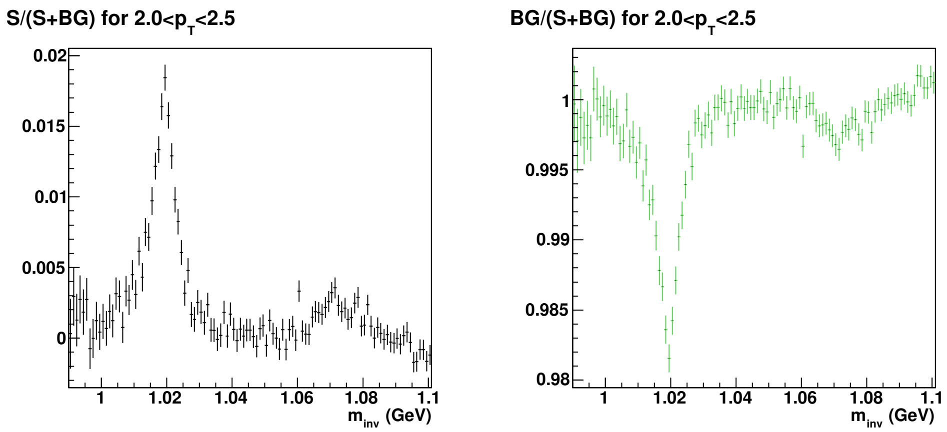


**Figure B.6**: $S/(S+B)$ and $B/(S+B)$ ratios obtained when over-estimating the raw $\phi$-meson yield.

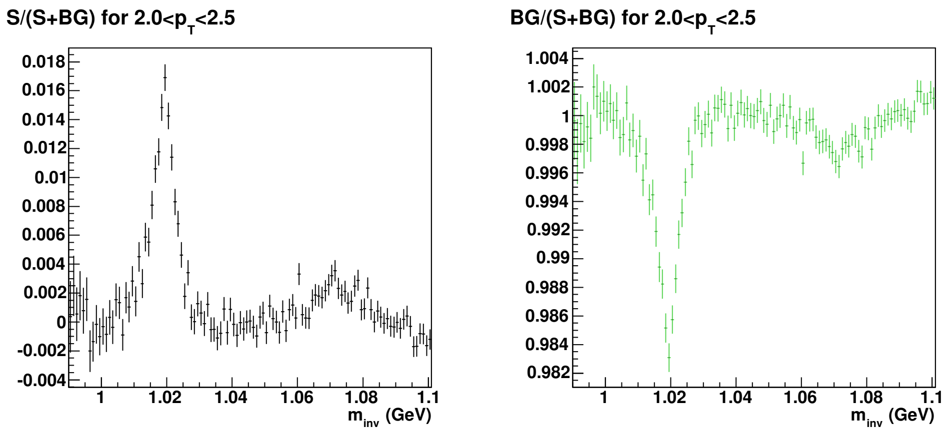


**Figure B.7**: $S/(S+B)$ and $B/(S+B)$ ratios obtained when under-estimating the raw $\phi$-meson yield.

## B.3 $\langle v_2 \rangle$ Method Details

The general method for obtaining $\langle v_2 \rangle$ is illustrated for the $\phi$-meson for the 10-40% central case in the four-panel plot in Fig. B.8:

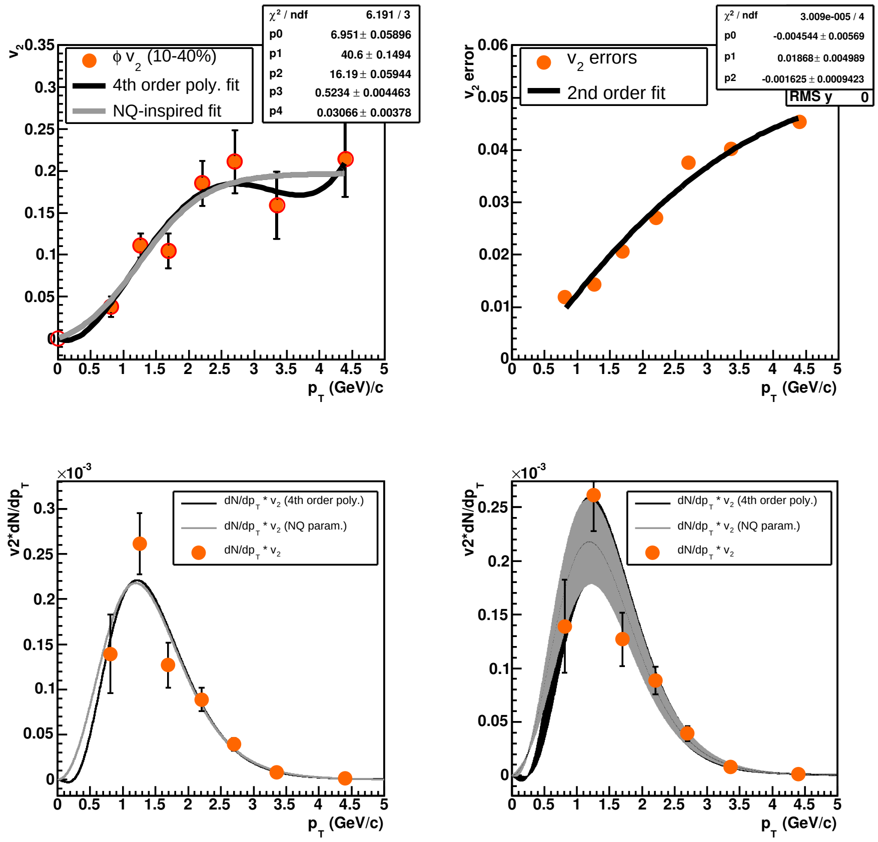


**Figure B.8**: Illustration of the method of extracting $\langle v_2 \rangle$ as described in the text. **Top left panel:** $v_2(p_T)$ for the $\phi$-meson for 10-40% central collisions. The black curve is a 4th order polynomial fit and the grey curve is the fit from equation 3.20. **Bottom left panel:** Normalized $\phi$ $dN/dp_T$ distribution multiplied with corresponding $v_2(p_T)$ parameterization (curve colours are the same as before). The datapoints show the datapoints from the top left panel multiplied by $dN/dp_T$ for corresponding $p_T$. **Top right panel:** Error on $v_2$ vs. $p_T$. The black curve is a second order polynomial fit to the data points. **Bottom right panel:** Same as bottom left panel but including statistical errors.

- The $v_2(p_T)$ is parameterized with both a polynomial function and with the function given by equation 3.20 (top left panel). The parameterization is forced to zero at the origin since $v_2(p_T = 0) = 0$ by definition.

- The normalized (i.e. integral=1) $dN/dp_T$ distribution (taken from fitting the $p_T$ spectrum) is multiplied with each of the $v_2$ parameterizations and shown in the bottom left panel by the black and grey histograms (bottom left panel).

- The errors on $v_2$ are parameterized as a function of $p_T$ and extrapolated to low and high $p_T$ (top right panel). For comparison, the $v_2$ datapoints from the top left panel are multiplied by the $dN/dp_T$ value at the corresponding $p_T$ and are also shown.

- The statistical errors are propagated into the distributions (bottom right panel).

- The $\langle v_2 \rangle$ for each choice of $v_2(p_T)$ parameterization is given by the integral of the corresponding distributions in the bottom right panel. The final $\langle v_2 \rangle$ was obtained from calculating the mean of the two $\langle v_2 \rangle$ results and the systematic error was estimated from their difference.

For the case of the $K^0_S$ $\langle v_2 \rangle$, a further consideration needed to be taken into account. The STAR $K^{\pm}$ and $K^0_S$ spectra do not have consistent shapes as would be expected and the source of the inconsistency has not yet been resolved. Therefore, to take this uncertainty into account, both the $K^0_S$ and $K^{\pm}$ spectra were used to determine the $K^0_S$ $\langle v_2 \rangle$ as shown in Fig. B.9. This resulted in an additional contribution to the $K^0_S$ $\langle v_2 \rangle$ systematic error.

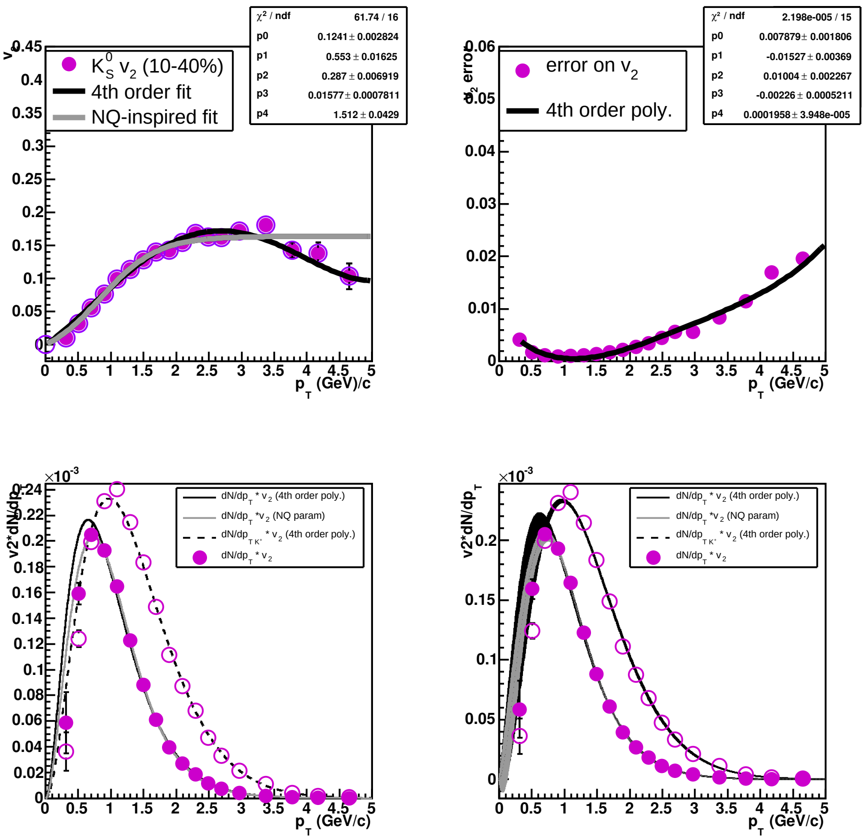


**Figure B.9**: The method described above for obtaining $\langle v_2 \rangle$, applied for the case of $K_S^0$. **Top left panel:** $v_2(p_T)$ for the $K_S^0$ for 10-40% central collisions [88]. The black curve is a 4th order polynomial fit and the grey curve is the fit from equation 3.20. **Bottom left panel:** Normalized $K_S^0$ $dN/dp_T$ distribution multiplied with corresponding $v_2(p_T)$ parameterization shown by the solid curves (curve colours are the same as before). The dashed curve shows the normalized $K^+$ $dN/dp_T$ distribution multiplied with the 4th order polynomial $v_2(p_T)$ parameterization. The solid(open) datapoints show the datapoints from the top left panel multiplied by the $K_S^0(K^+)$ $dN/dp_T$ for corresponding $p_T$. **Top right panel:** Error on $v_2$ vs. $p_T$. The black curve is a fourth order polynomial fit to the data points. **Bottom right panel:** Same as bottom left panel but including statistical errors.

# Appendix C

# Invariant mass distributions

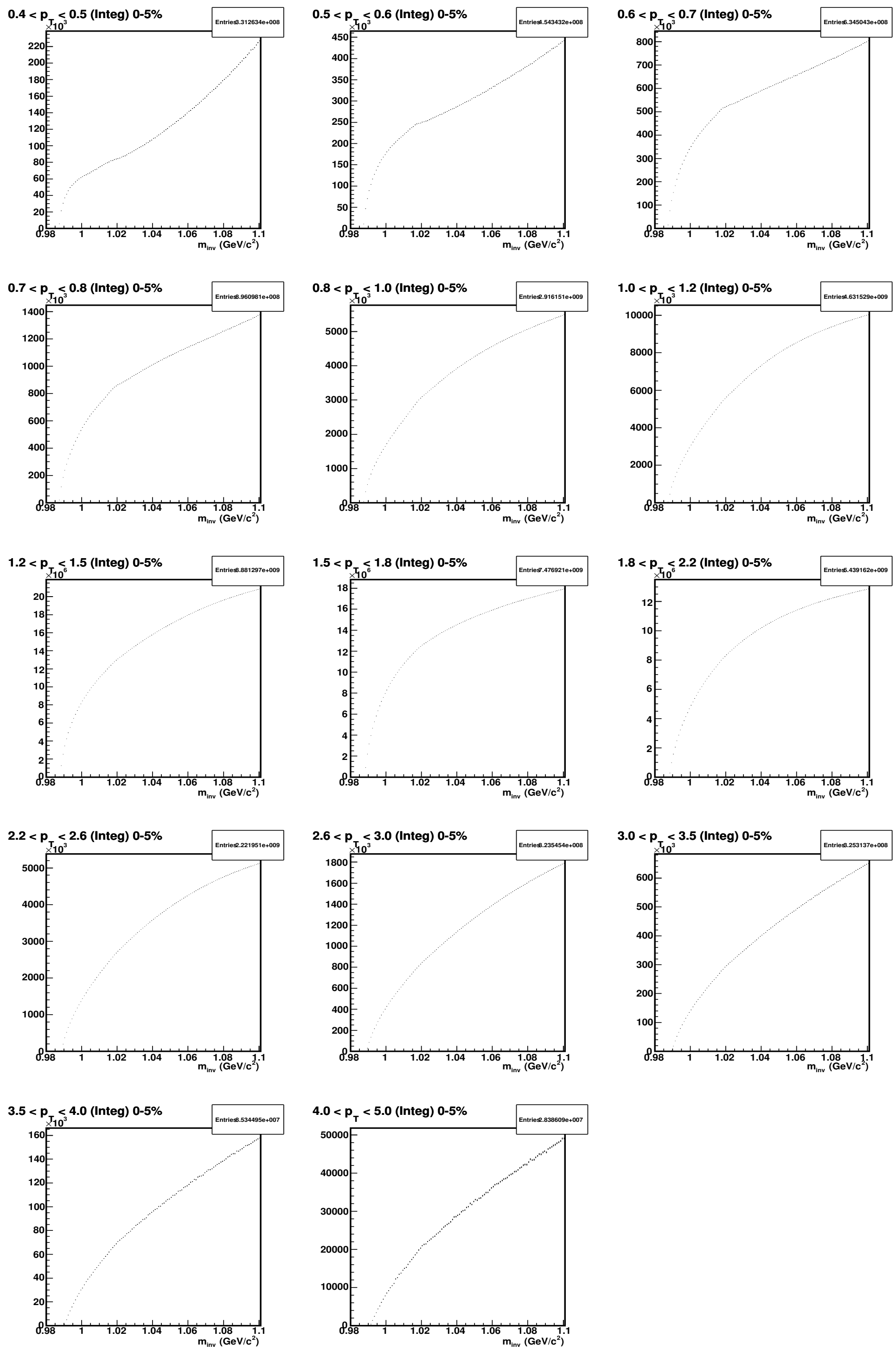


**Figure C.1**: Same-event $m_{inv}$ distribution for Au+Au collisions at $\sqrt{s_{NN}} = 200$ GeV for 0-5% centrality. (From central-triggered dataset.)

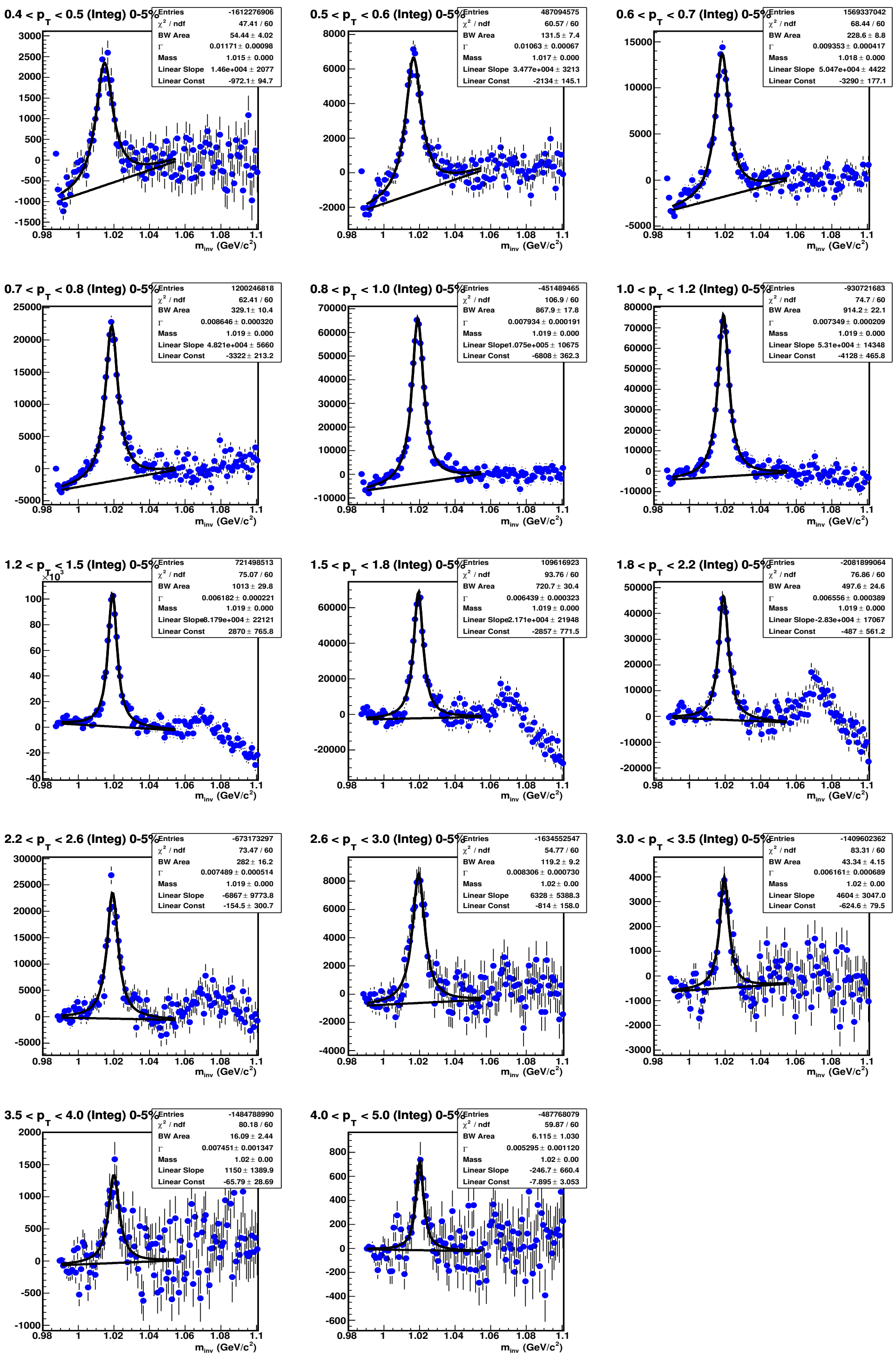


**Figure C.2**: $m_{inv}$ distribution after subtraction of scaled mixed-event background for Au+Au collisions at $\sqrt{s_{NN}} = 200$ GeV for 0-5% centrality. (From central-triggered dataset.)

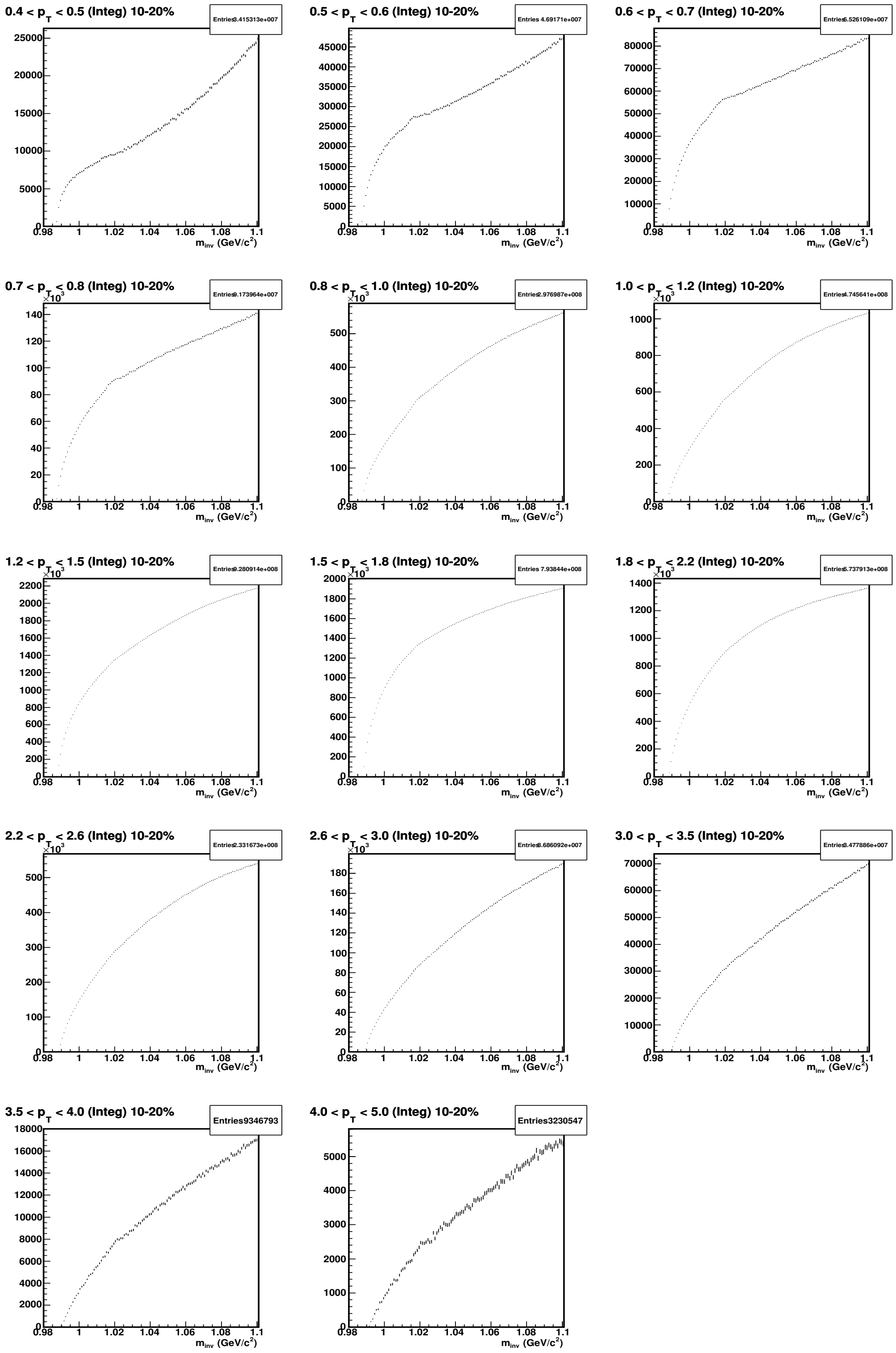

**Figure C.3**: Same-event $m_{inv}$ distribution for Au+Au collisions at $\sqrt{s_{NN}} = 200$ GeV for 10-20% centrality.

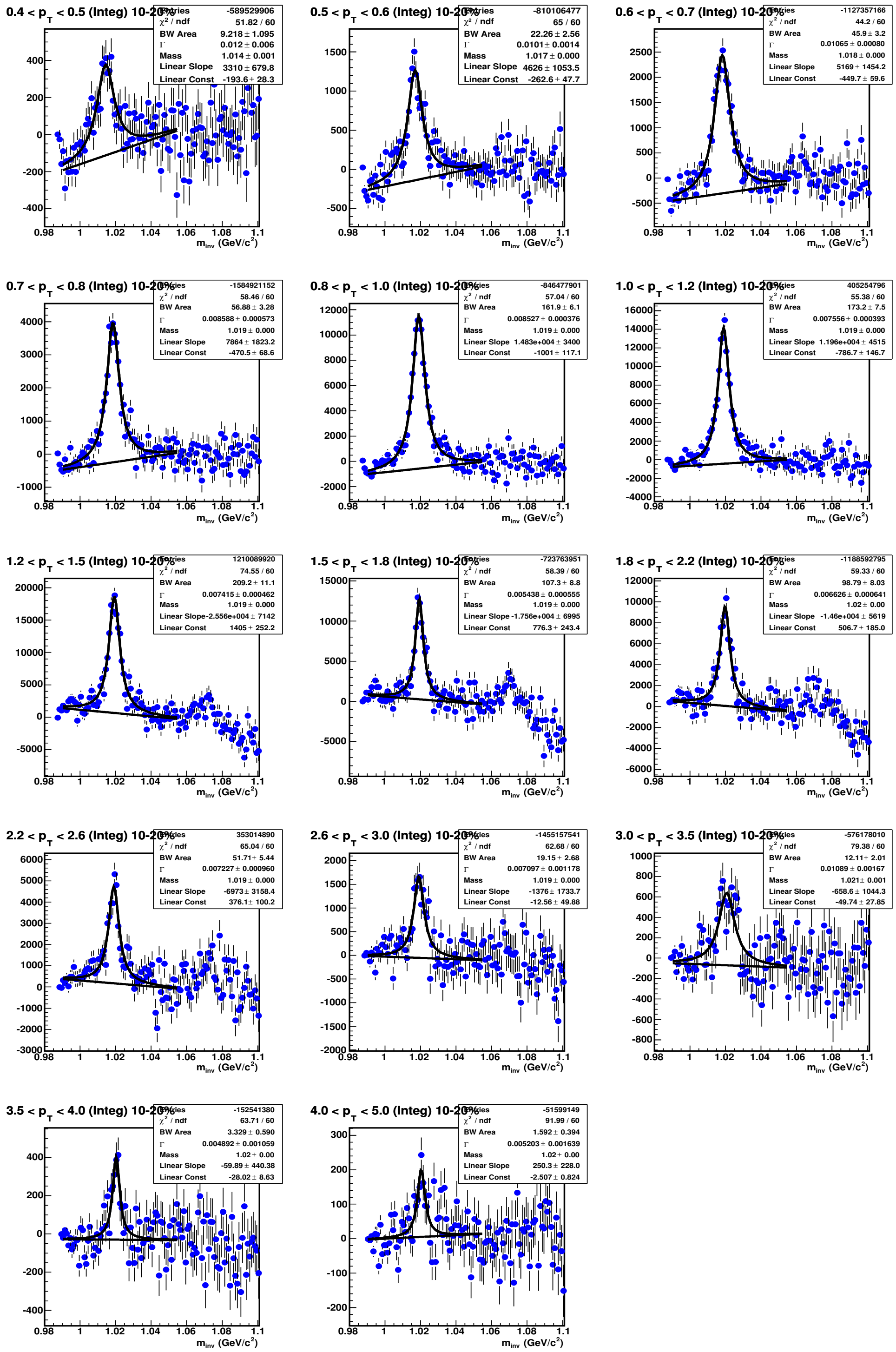

**Figure C.4**: $m_{inv}$ distribution after subtraction of scaled mixed-event background for Au+Au collisions at $\sqrt{s_{NN}}$ = 200 GeV for 10-20% centrality.

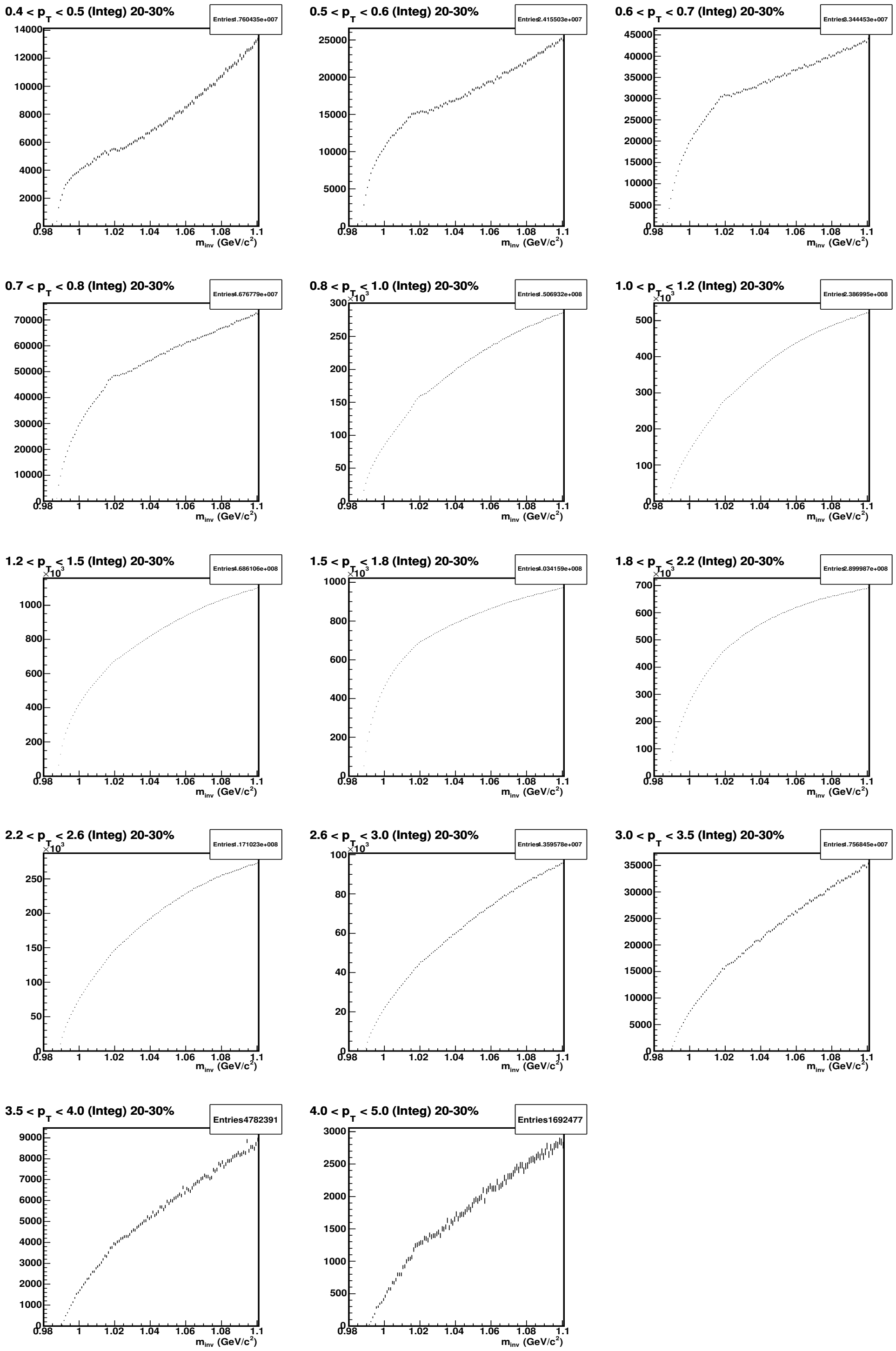

**Figure C.5**: Same-event $m_{inv}$ distribution for Au+Au collisions at $\sqrt{s_{NN}} = 200$ GeV for 20-30% centrality.

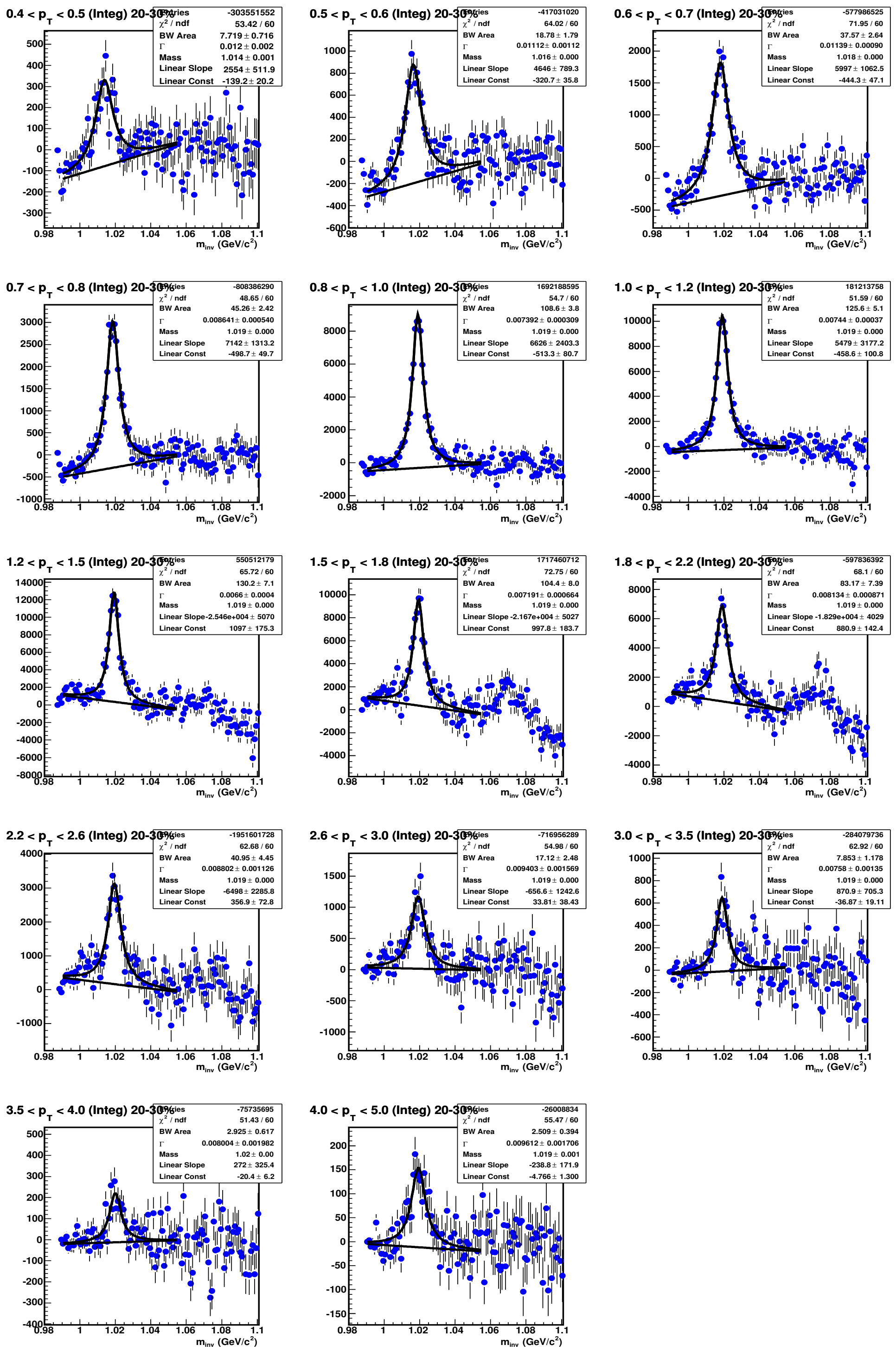


**Figure C.6**: $m_{inv}$ distribution after subtraction of scaled mixed-event background for Au+Au collisions at $\sqrt{s_{NN}} = 200$ GeV for 20-30% centrality.

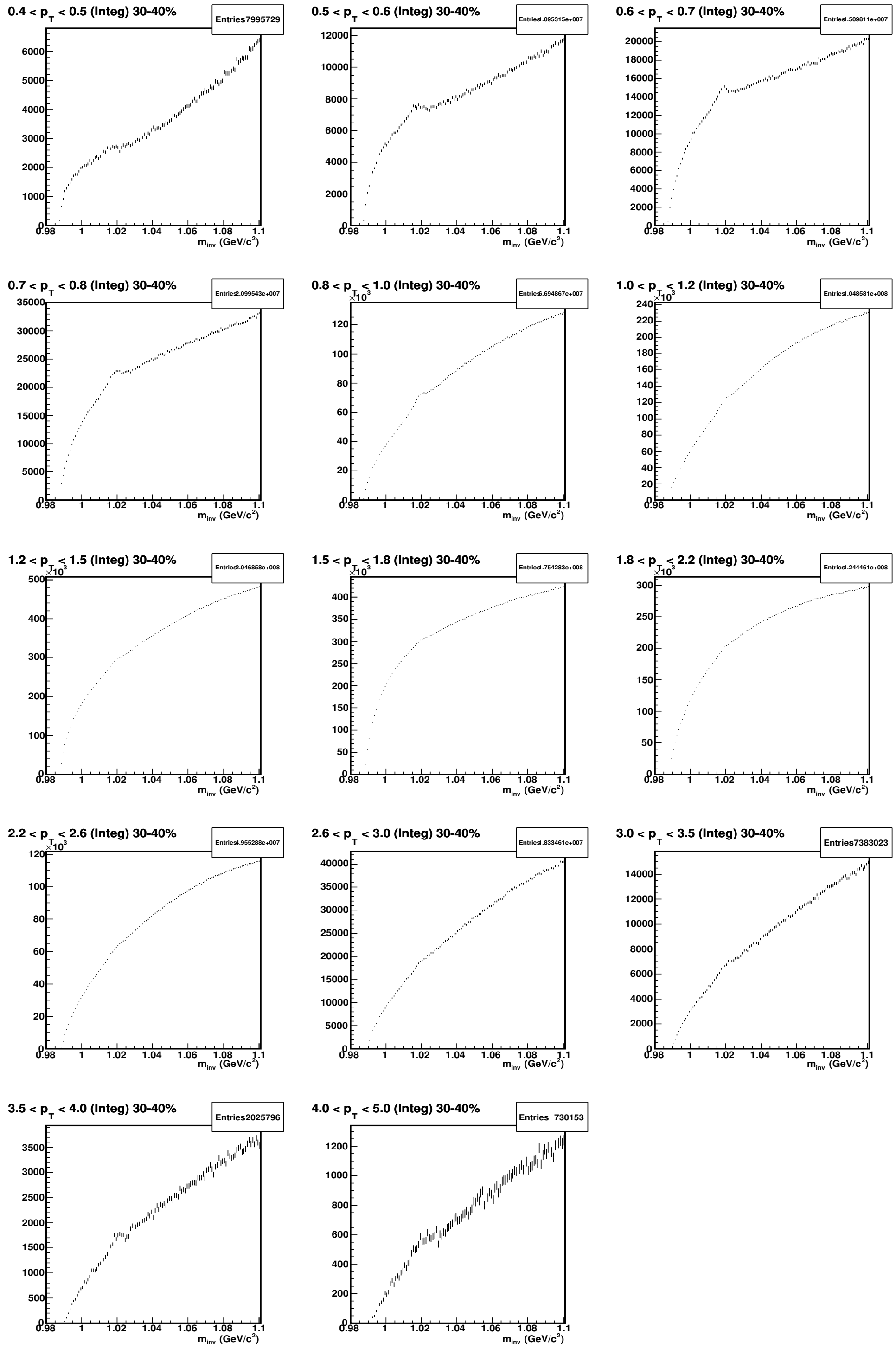


**Figure C.7**: Same-event $m_{inv}$ distribution for Au+Au collisions at $\sqrt{s_{NN}} = 200$ GeV for 30-40% centrality.

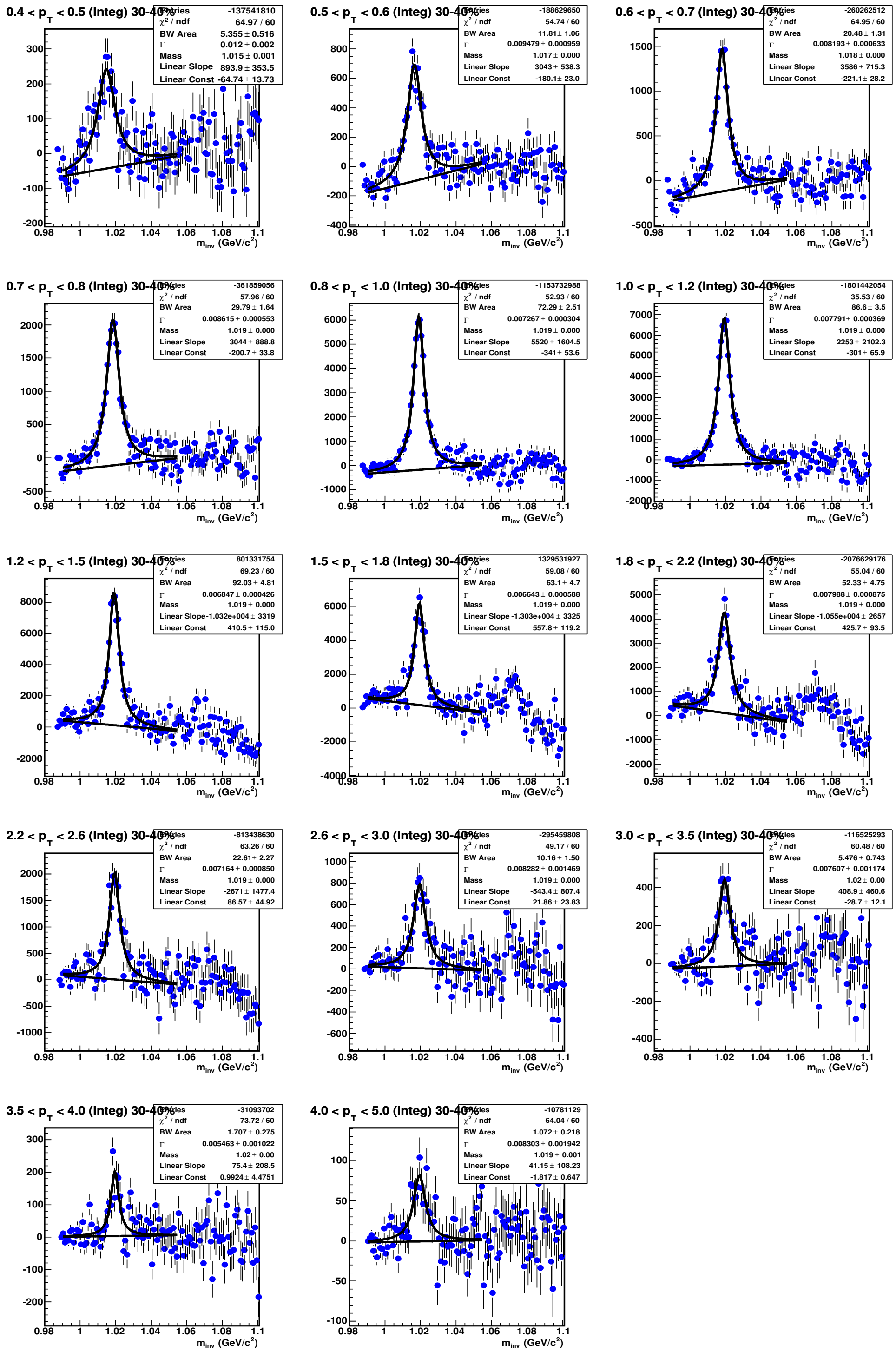

**Figure C.8**: $m_{inv}$ distribution after subtraction of scaled mixed-event background for Au+Au collisions at $\sqrt{s_{NN}}$ = 200 GeV for 30-40% centrality.

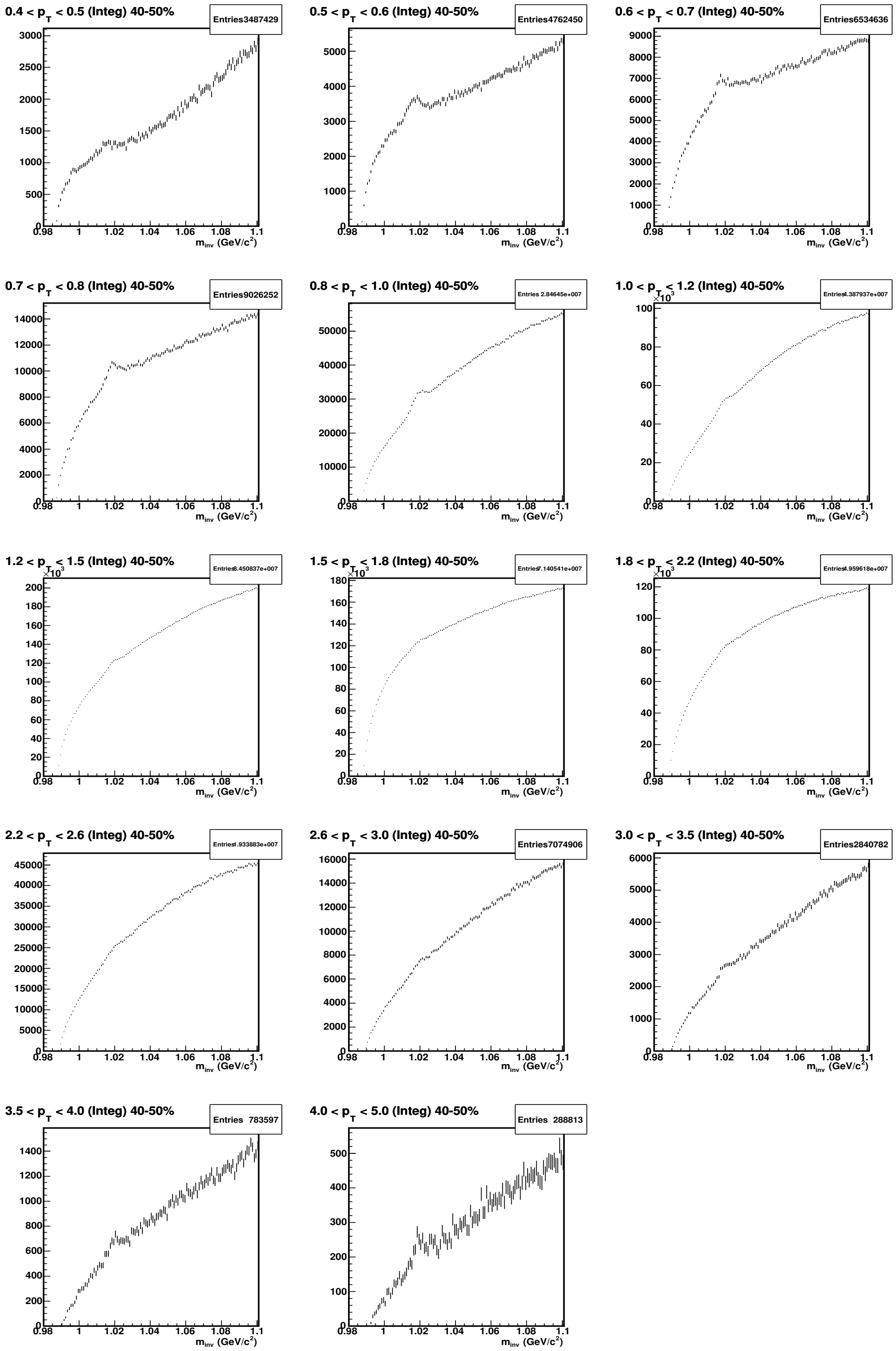

**Figure C.9**: Same-event $m_{inv}$ distribution for Au+Au collisions at $\sqrt{s_{NN}} = 200$ GeV for 40-50% centrality.

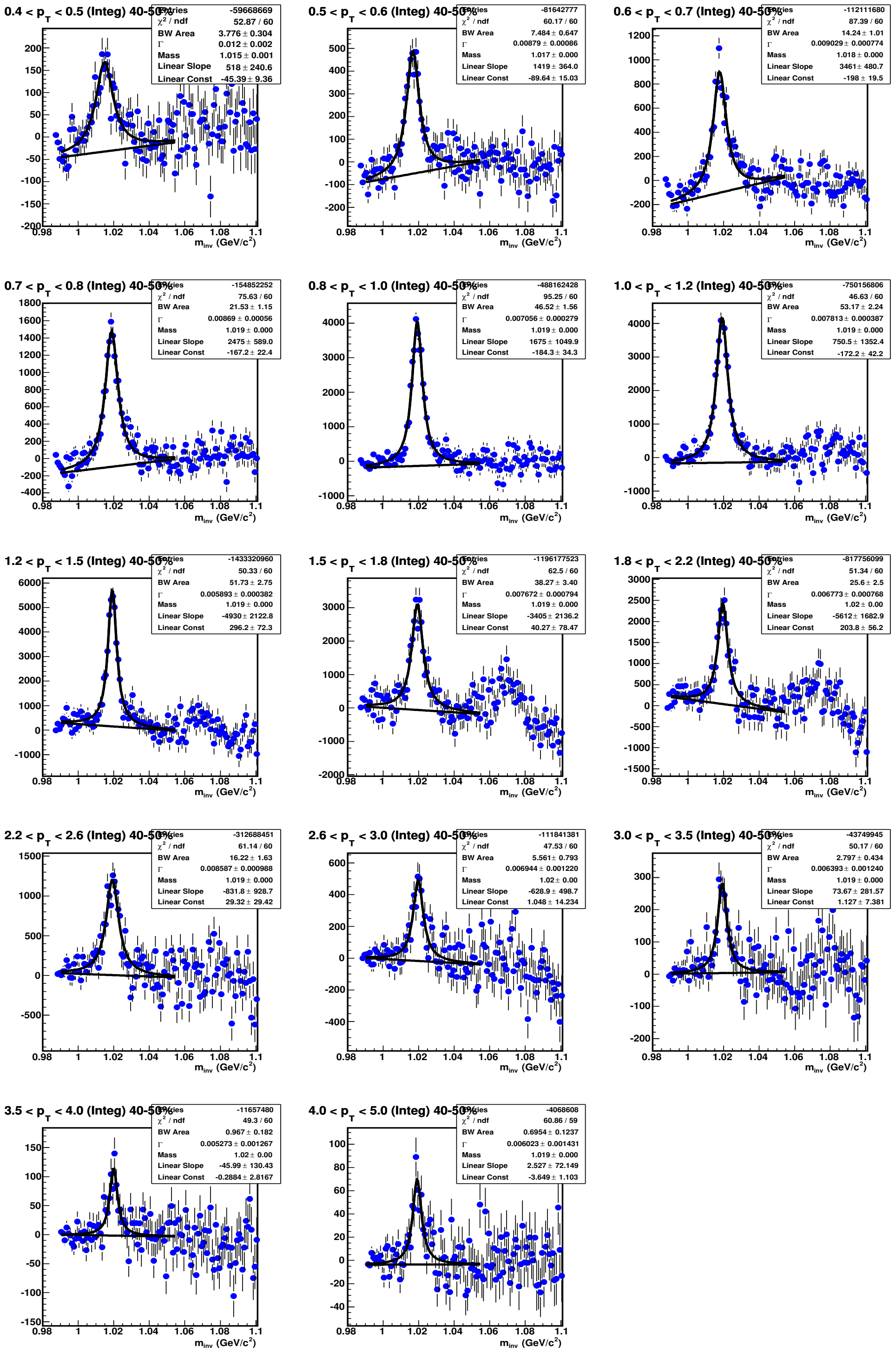

**Figure C.10**: $m_{inv}$ distribution after subtraction of scaled mixed-event background for Au+Au collisions at $\sqrt{s_{NN}} = 200$ GeV for 40-50% centrality.

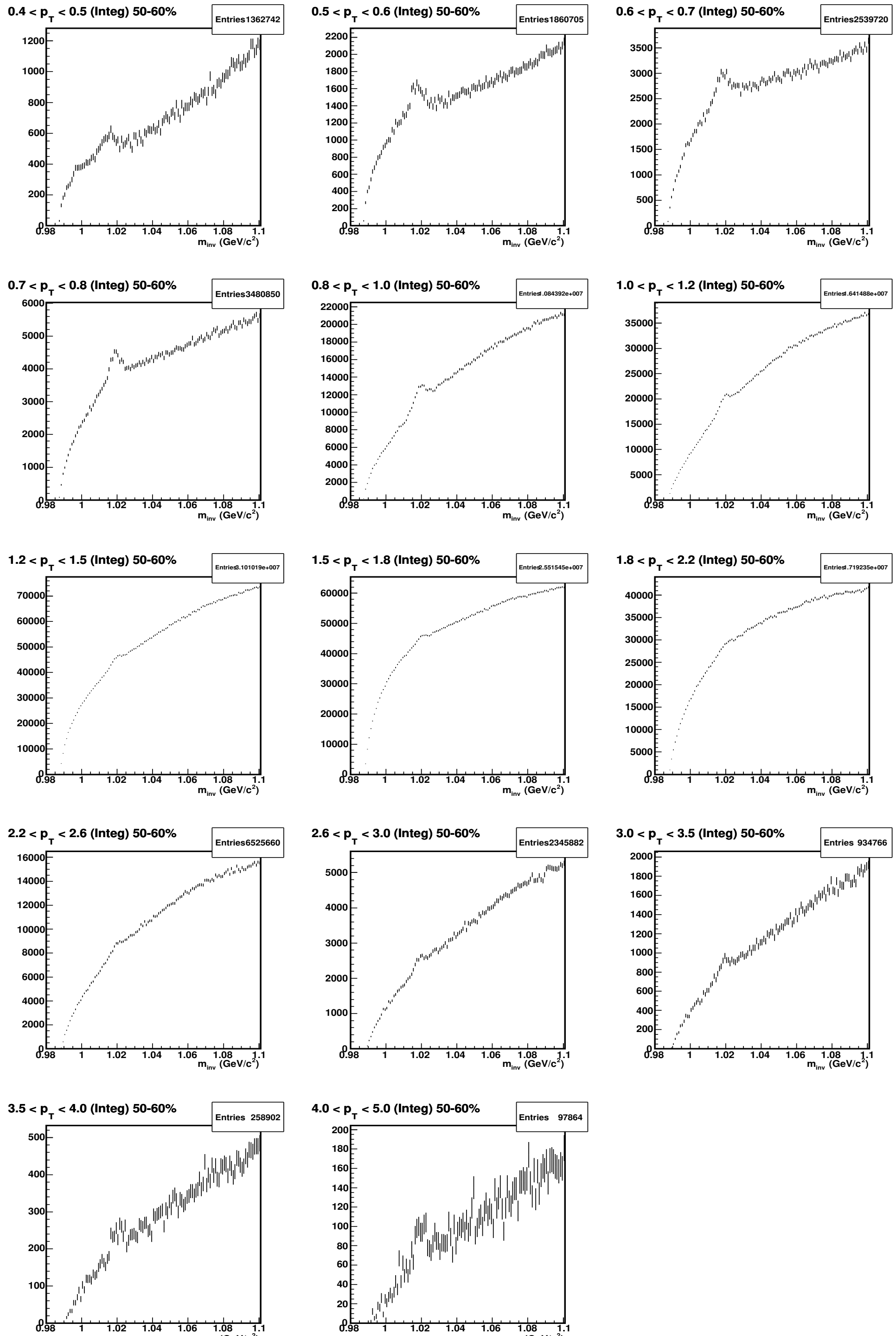


**Figure C.11**: Same-event $m_{inv}$ distribution for Au+Au collisions at $\sqrt{s_{NN}} = 200$ GeV for 50-60% centrality.

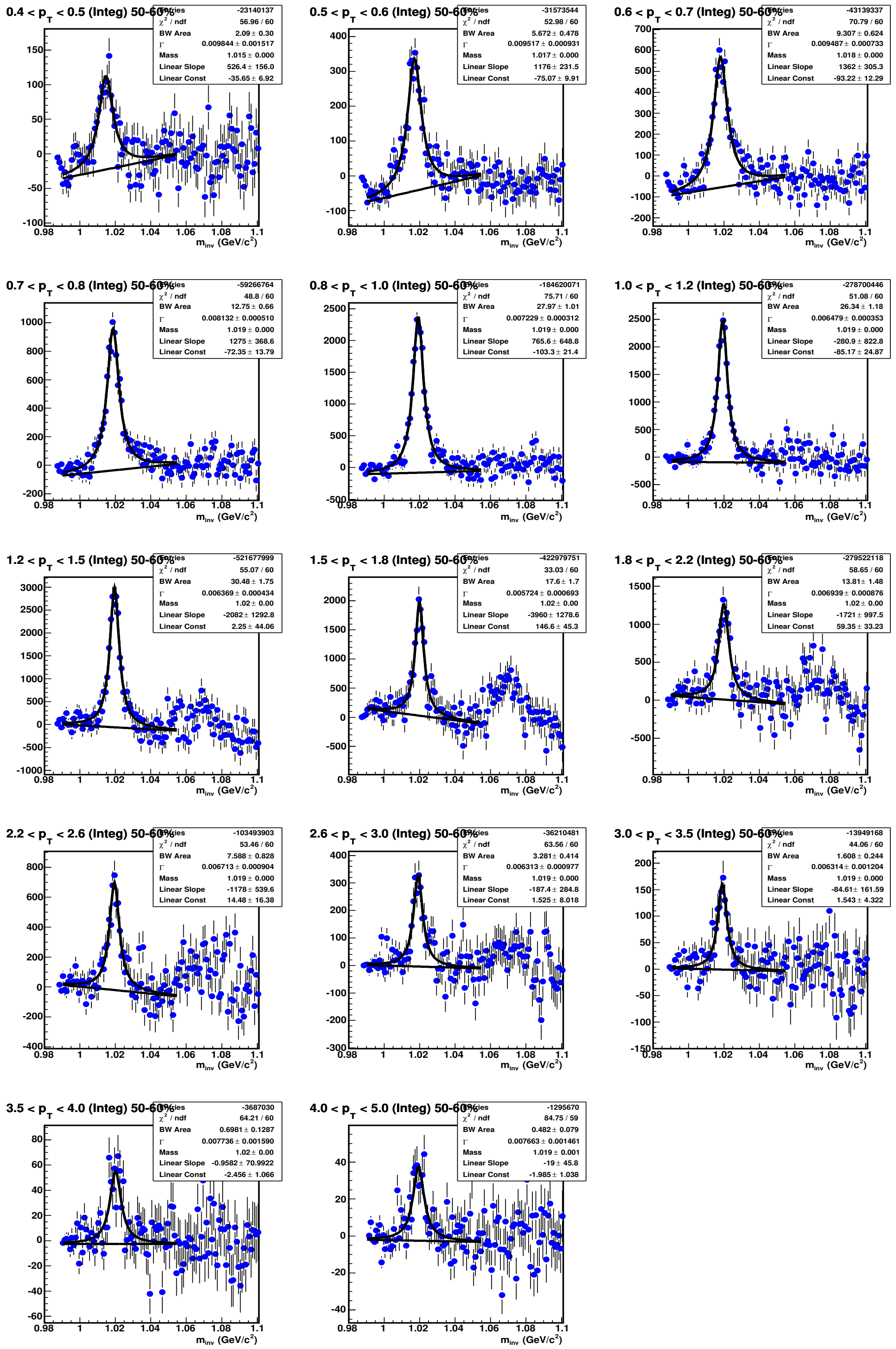


**Figure C.12**: $m_{inv}$ distribution after subtraction of scaled mixed-event background for Au+Au collisions at $\sqrt{s_{NN}}$ = 200 GeV for 50-60% centrality.

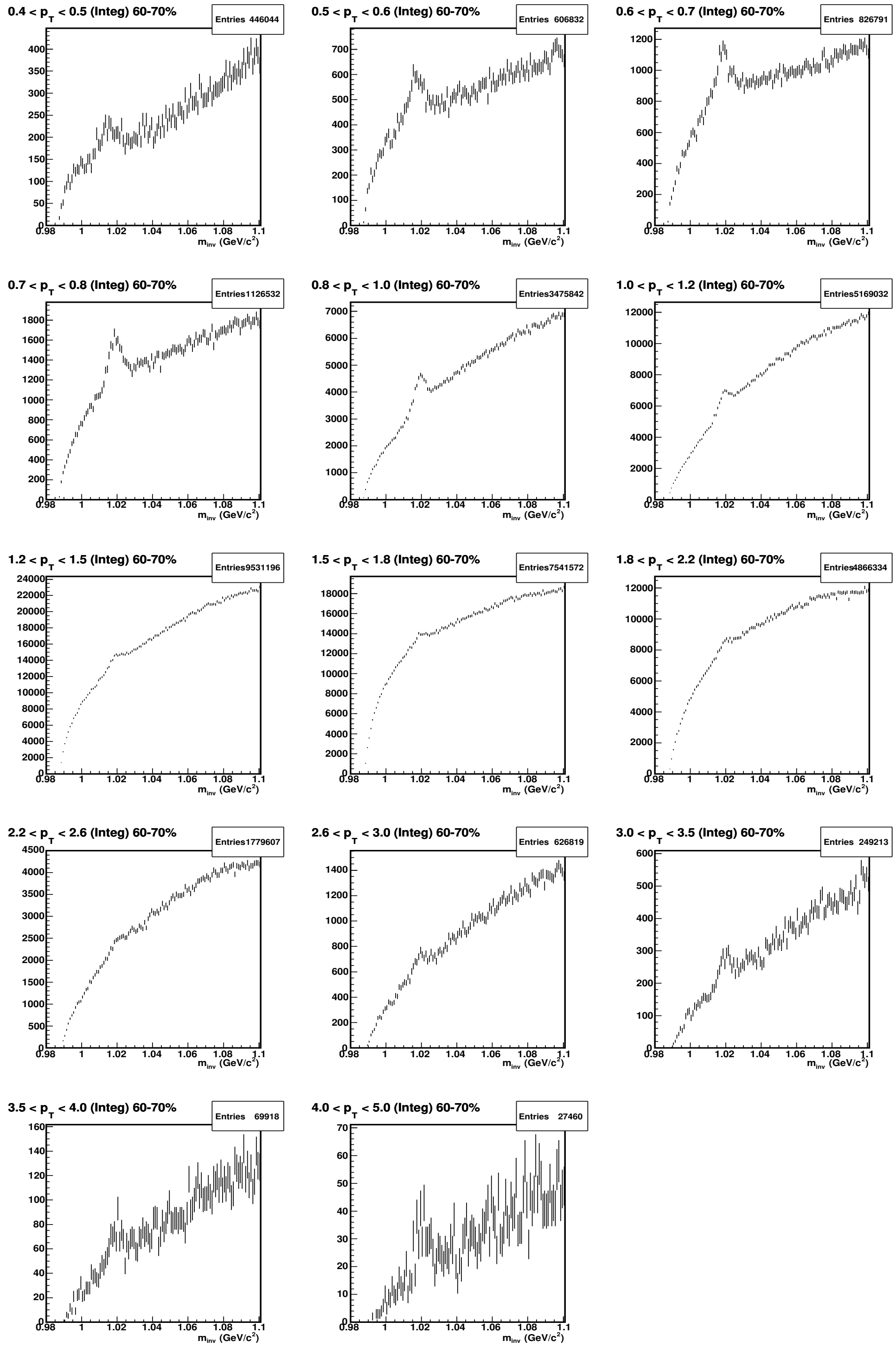


**Figure C.13**: Same-event $m_{inv}$ distribution for Au+Au collisions at $\sqrt{s_{NN}} = 200$ GeV for 60-70% centrality.

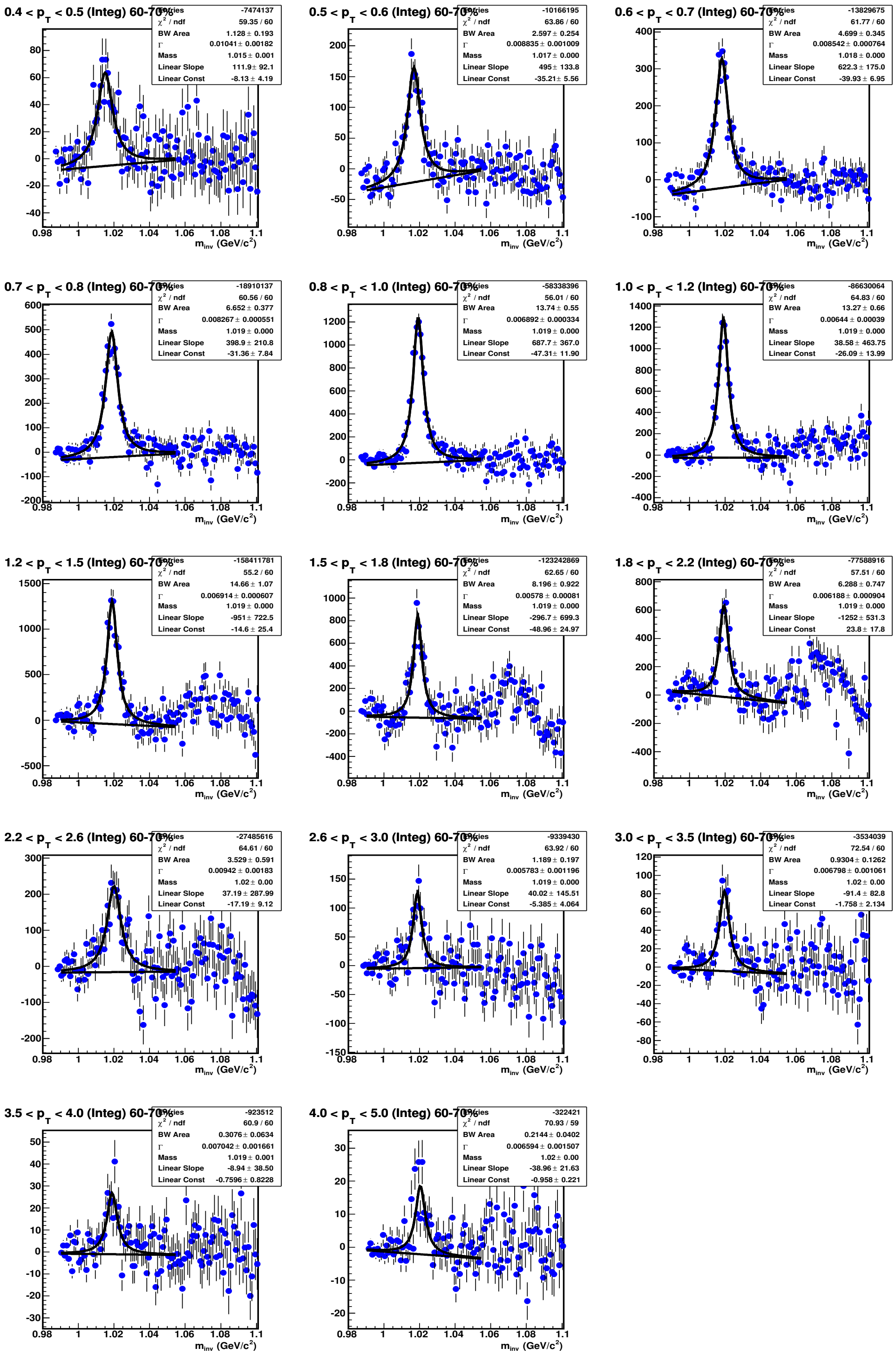

**Figure C.14**: $m_{inv}$ distribution after subtraction of scaled mixed-event background for Au+Au collisions at $\sqrt{s_{NN}} = 200$ GeV for 60-70% centrality.

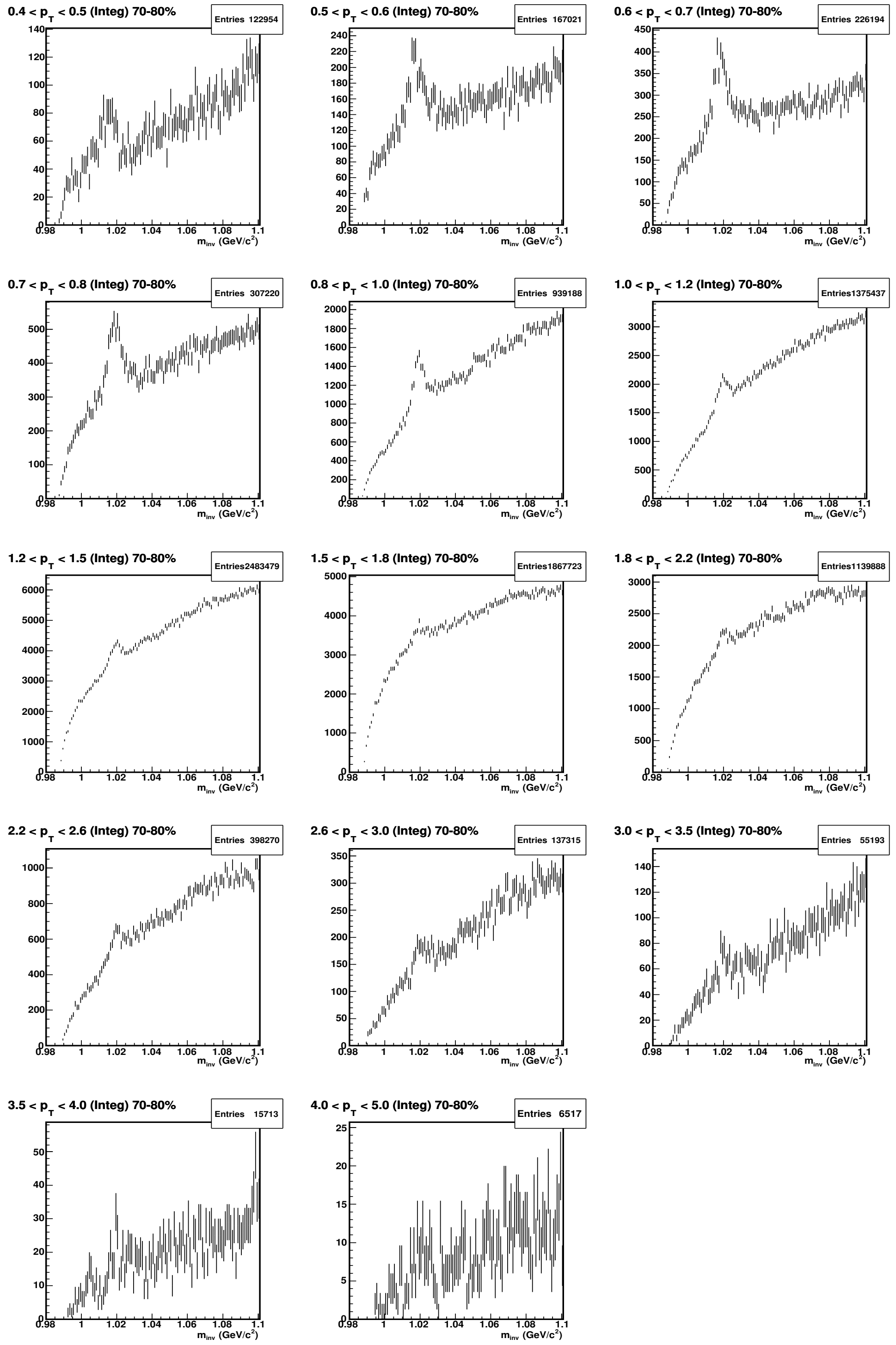


**Figure C.15**: Same-event $m_{inv}$ distribution for Au+Au collisions at $\sqrt{s_{NN}} = 200$ GeV for 70-80% centrality.

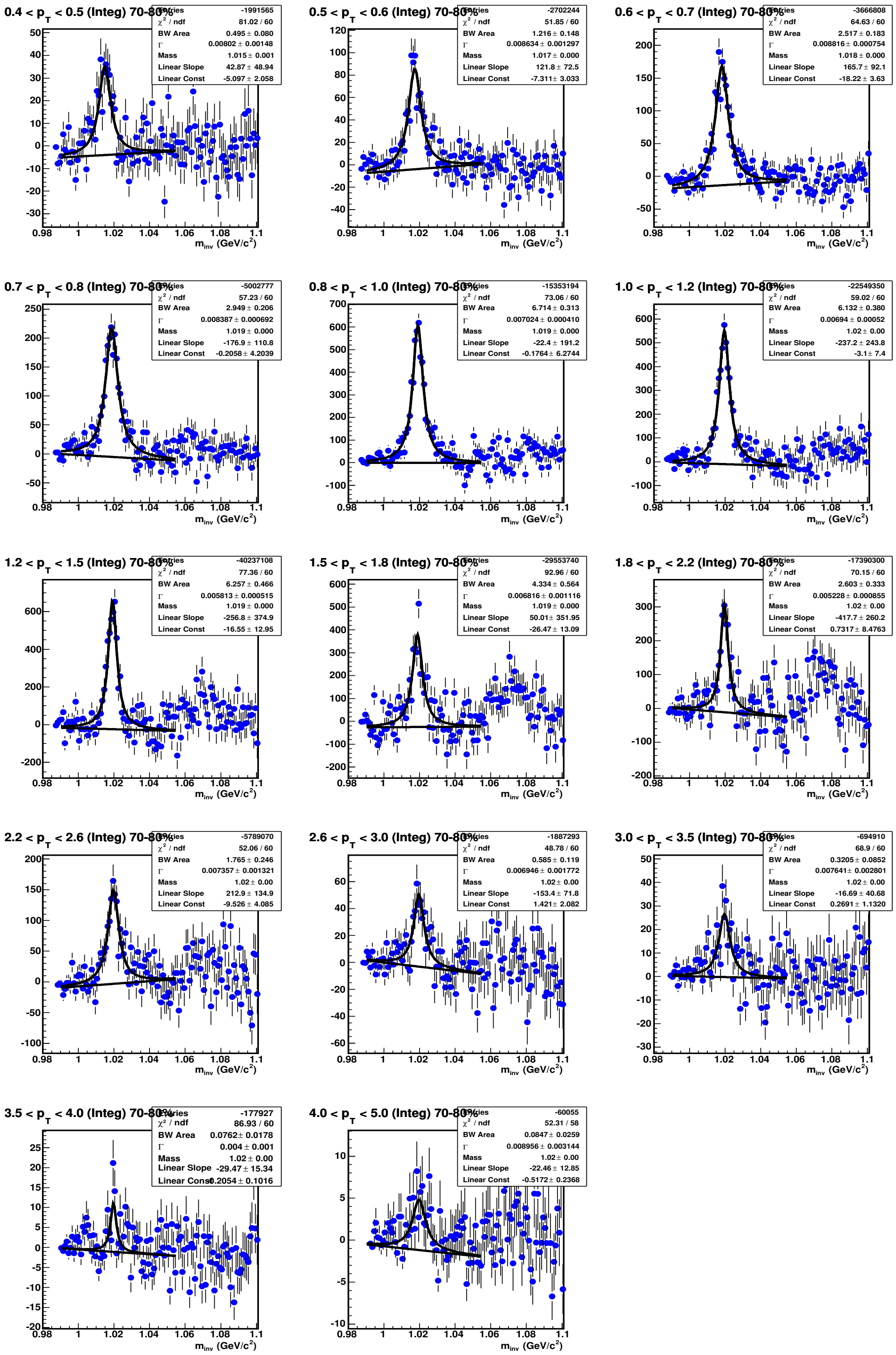


**Figure C.16**: $m_{inv}$ distribution after subtraction of scaled mixed-event background for Au+Au collisions at $\sqrt{s_{NN}}$ = 200 GeV for 70-80% centrality.

# Bibliography


[1] H. Fritzsch, M. Gell-Mann, and H. Leutwyler, "Advantages of the Color Octet Gluon Picture," *Phys. Lett.* **B47** (1973) 365–368.

[2] D. J. Gross and F. Wilczek, "Ultraviolet Behavior of Non-Abelian Gauge Theories," *Phys. Rev. Lett.* **30** (1973) 1343–1346.

[3] H. D. Politzer, "Reliable Perturbative Results for Strong Interactions?," *Phys. Rev. Lett.* **30** (1973) 1346–1349.

[4] D. J. Gross and F. Wilczek, "Asymptotically free gauge theories. 1," *Phys. Rev.* **D8** (1973) 3633–3652.

[5] S. Bethke, "alpha(s) 2002," *Nucl. Phys. Proc. Suppl.* **121** (2003) 74–81, `hep-ex/0211012`.

[6] J. C. Collins and M. J. Perry, "Superdense Matter: Neutrons or Asymptotically Free Quarks?," *Phys. Rev. Lett.* **34** (1975) 1353.

[7] F. Karsch, "Lattice results on QCD thermodynamics," *Nucl. Phys.* **A698** (2002) 199–208, `hep-ph/0103314`.

[8] K. Rajagopal and F. Wilczek, "The condensed matter physics of QCD," `hep-ph/0011333`.

[9] Z. Fodor, "Lattice QCD results at finite temperature and density," *Nucl. Phys.* **A715** (2003) 319–328, `hep-lat/0209101`.

[10] G. F. Chapline, M. H. Johnson, E. Teller, and M. S. Weiss, "Highly excited nuclear matter," *Phys. Rev.* **D8** (1973) 4302–4308.

[11] R. J. Glauber and G. Matthiae, "High-energy scattering of protons by nuclei," *Nucl. Phys.* **B21** (1970) 135–157.

[12] A. Bialas, M. Bleszynski, and W. Czyz, "Multiplicity Distributions in Nucleus-Nucleus Collisions at High-Energies," *Nucl. Phys.* **B111** (1976) 461.

[13] P. Shukla, "The Glauber model and the heavy ion reaction cross section," *Phys. Rev.* **C67** (2003) 054607, `nucl-th/0302030`.

[14] J. W. Harris and B. Müller, "The search for the quark-gluon plasma," *Ann. Rev. Nucl. Part. Sci.* **46** (1996) 71–107, `hep-ph/9602235`.

[15] S. A. Bass, M. Gyulassy, H. Stöcker, and W. Greiner, "Signatures of quark-gluon-plasma formation in high energy heavy-ion collisions: A critical review," *J. Phys.* **G25** (1999) R1–R57, `hep-ph/9810281`.

[16] T. Matsui and H. Satz, "$J/\psi$ Suppression By Quark-Gluon Plasma Formation," *Phys. Lett.* **B178** (1986) 416.

[17] J. Rafelski, "Formation and Observables of the Quark-Gluon Plasma," *Phys. Rept.* **88** (1982) 331.

[18] R. D. Pisarski, "Phenomenology of the Chiral Phase Transition," *Phys. Lett.* **B110** (1982) 155.

[19] J. Cleymans and K. Redlich, "Chemical and thermal freeze-out parameters from 1-A-GeV to 200-A-GeV," *Phys. Rev.* **C60** (1999) 054908, `nucl-th/9903063`.

[20] P. Braun-Munzinger, D. Magestro, K. Redlich, and J. Stachel, "Hadron production in Au Au collisions at RHIC," *Phys. Lett.* **B518** (2001) 41–46, `hep-ph/0105229`.

[21] N. Xu and M. Kaneta, "Hadron freeze-out conditions in high energy nuclear collisions," *Nucl. Phys.* **A698** (2002) 306–313, `nucl-ex/0104021`.

[22] **STAR** Collaboration, J. Adams *et al.*, "Experimental and theoretical challenges in the search for the quark gluon plasma: The STAR collaboration's critical assessment of the evidence from RHIC collisions," *Nucl. Phys.* **A757** (2005) 102–183, `nucl-ex/0501009`.

[23] **STAR** Collaboration, O. Y. Barannikova, "Probing collision dynamics at RHIC," `nucl-ex/0403014`.

[24] J. Cleymans, B. Kämpfer, M. Kaneta, S. Wheaton, and N. Xu, "Centrality dependence of thermal parameters deduced from hadron multiplicities in Au + Au collisions at $\sqrt{s_{NN}} = 130$-GeV," *Phys. Rev.* **C71** (2005) 054901, `hep-ph/0409071`.

[25] P. Braun-Munzinger, K. Redlich, and J. Stachel, "Particle production in heavy ion collisions," `nucl-th/0304013`.

[26] **PHENIX** Collaboration, K. Adcox *et al.*, "Formation of dense partonic matter in relativistic nucleus nucleus collisions at RHIC: Experimental evaluation by the PHENIX collaboration," *Nucl. Phys.* **A757** (2005) 184–283, `nucl-ex/0410003`.

[27] E. Schnedermann, J. Sollfrank, and U. W. Heinz, "Thermal phenomenology of hadrons from 200-A/GeV S+S collisions," *Phys. Rev.* **C48** (1993) 2462–2475, `nucl-th/9307020`.

[28] B. B. Back *et al.*, "The PHOBOS perspective on discoveries at RHIC," *Nucl. Phys.* **A757** (2005) 28–101, `nucl-ex/0410022`.

[29] **BRAHMS** Collaboration, I. Arsene *et al.*, "Quark gluon plasma and color glass condensate at RHIC? The perspective from the BRAHMS experiment," *Nucl. Phys.* **A757** (2005) 1–27, `nucl-ex/0410020`.

[30] **STAR** Collaboration, J. Adams *et al.*, "Transverse momentum and collision energy dependence of high p(T) hadron suppression in Au + Au collisions at ultrarelativistic energies," *Phys. Rev. Lett.* **91** (2003) 172302, `nucl-ex/0305015`.

[31] X.-N. Wang and M. Gyulassy, "Gluon shadowing and jet quenching in A + A collisions at $\sqrt{s_{NN}} = 200$-GeV," *Phys. Rev. Lett.* **68** (1992) 1480–1483.

[32] X.-N. Wang, "A pQCD-based approach to parton production and equilibration in high-energy nuclear collisions," *Phys. Rept.* **280** (1997) 287–371, `hep-ph/9605214`.

[33] **STAR** Collaboration, J. Adams *et al.*, "Particle-type dependence of azimuthal anisotropy and nuclear modification of particle production in Au+Au collisions at $\sqrt{s_{NN}} = 200$ GeV," *Phys. Rev. Lett.* **92** (2004) 052302, `nucl-ex/0306007`.

[34] R. J. Fries, B. Müller, C. Nonaka, and S. A. Bass, "Hadron production in heavy ion collisions: Fragmentation and recombination from a dense parton phase," *Phys. Rev.* **C68** (2003) 044902, `nucl-th/0306027`.

[35] **STAR** Collaboration, J. Adams *et al.*, "Measurements of identified particles at intermediate transverse momentum in the STAR experiment from Au + Au collisions at $\sqrt{s_{NN}} = 200$-GeV," `nucl-ex/0601042`.

[36] **STAR** Collaboration, B. Abelev *et al.*, "Identified baryon and meson distributions at large transverse momenta from Au+Au collisions at sqrt(sNN) = 200 GeV," *Phys. Rev. Lett.* **97** (2006) 152301, `nucl-ex/0606003`.

[37] **PHENIX** Collaboration, S. S. Adler *et al.*, "Scaling properties of proton and anti-proton production in $\sqrt{s_{NN}} = 200$-GeV Au + Au collisions," *Phys. Rev. Lett.* **91** (2003) 172301, `nucl-ex/0305036`.

[38] S. A. Voloshin, "Anisotropic flow," *Nucl. Phys.* **A715** (2003) 379–388, `nucl-ex/0210014`.

[39] D. Molnar and S. A. Voloshin, "Elliptic flow at large transverse momenta from quark coalescence," *Phys. Rev. Lett.* **91** (2003) 092301, `nucl-th/0302014`.

[40] V. Greco, C. M. Ko, and P. Levai, "Parton coalescence at RHIC," *Phys. Rev.* **C68** (2003) 034904, `nucl-th/0305024`.

[41] R. J. Fries, "Recombination models," *J. Phys.* **G30** (2004) S853–S860, `nucl-th/0403036`.

[42] A. M. Poskanzer and S. A. Voloshin, "Methods for analyzing anisotropic flow in relativistic nuclear collisions," *Phys. Rev.* **C58** (1998) 1671–1678, `nucl-ex/9805001`.

[43] **STAR** Collaboration, J. Adams *et al.*, "Azimuthal anisotropy in Au + Au collisions at $\sqrt{s_{NN}}$ = 200-GeV," *Phys. Rev.* **C72** (2005) 014904, `nucl-ex/0409033`.

[44] **PHENIX** Collaboration, S. S. Adler *et al.*, "Elliptic flow of identified hadrons in Au + Au collisions at $\sqrt{s_{NN}}$ = 200-GeV," *Phys. Rev. Lett.* **91** (2003) 182301, `nucl-ex/0305013`.

[45] **STAR** Collaboration, M. D. Oldenburg, "Scaling of anisotropic flow in the picture of quark coalescence," *J. Phys.* **G31** (2005) S437–S442, `nucl-ex/0412001`.

[46] **PHOBOS** Collaboration, B. B. Back *et al.*, "Pseudorapidity and centrality dependence of the collective flow of charged particles in Au + Au collisions at $\sqrt{s_{NN}}$ = 130-GeV," *Phys. Rev. Lett.* **89** (2002) 222301, `nucl-ex/0205021`.

[47] X. Dong, S. Esumi, P. Sorensen, N. Xu, and Z. Xu, "Resonance decay effects on anisotropy parameters," *Phys. Lett.* **B597** (2004) 328–332, `nucl-th/0403030`.

[48] R. C. Hwa and C. B. Yang, "Scaling distributions of quarks, mesons and proton for all p(T), energy and centrality," *Phys. Rev.* **C67** (2003) 064902, `nucl-th/0302006`.

[49] H. Sorge, "Flavor Production in Pb(160AGeV) on Pb Collisions: Effect of Color Ropes and Hadronic Rescattering," *Phys. Rev.* **C52** (1995) 3291–3314, `nucl-th/9509007`.

[50] M. Bleicher *et al.*, "Relativistic hadron hadron collisions in the ultra-relativistic quantum molecular dynamics model," *J. Phys.* **G25** (1999) 1859–1896, `hep-ph/9909407`.

[51] M. Bleicher and H. Stöcker, "Anisotropic flow in ultra-relativistic heavy ion collisions," *Phys. Lett.* **B526** (2002) 309–314, `hep-ph/0006147`.

[52] Y. Lu *et al.*, "Anisotropic flow at RHIC: How unique is the number-of- constituent-quark scaling?," *J. Phys.* **G32** (2006) 1121–1130, `nucl-th/0602009`.

[53] W.-M. Yao *et al.*, "The Review of Particle Physics," *J. Phys. G* **33** (2006) 1.

[54] A. Shor, "Phi Meson Production As a Probe of the Quark Gluon Plasma," *Phys. Rev. Lett.* **54** (1985) 1122–1125.

[55] T. Ishikawa *et al.*, "Phi photo-production from Li, C, Al, and Cu nuclei at E(gamma) = 1.5-GeV - 2.4-GeV," *Phys. Lett.* **B608** (2005) 215–222, `nucl-ex/0411016`.

[56] A. Sibirtsev, H. W. Hammer, U. G. Meissner, and A. W. Thomas, "Phi-meson photoproduction from nuclei," *Eur. Phys. J.* **A29** (2006) 209–220, `nucl-th/0606044`.

[57] **STAR** Collaboration, J. Adams *et al.*, "Phi meson production in Au + Au and p + p collisions at $\sqrt{s_{NN}}$ = 200-GeV," *Phys. Lett.* **B612** (2005) 181–189, `nucl-ex/0406003`.

[58] R. C. Hwa and C. B. Yang, "Production of strange particles at intermediate p(T) at RHIC," `nucl-th/0602024`.

[59] **STAR** Collaboration, J. Adams *et al.*, "Multi-strange baryon elliptic flow in Au + Au collisions at $\sqrt{s_{NN}}$ = 200-GeV," *Phys. Rev. Lett.* **95** (2005) 122301, `nucl-ex/0504022`.

[60] **STAR** Collaboration, C. Adler *et al.*, "Midrapidity phi production in Au+Au collisions at sNN =130 GeV," *Phys. Rev.* **C65** (2002) 041901.

[61] M. Harrison, T. Ludlam, and S. Ozaki, "RHIC project overview," *Nucl. Instrum. Meth.* **A499** (2003) 235–244.

[62] `http://www.agsrhichome.bnl.gov/RHIC/Runs/`. RHIC Collider Accelerator Department.

[63] H. Hahn *et al.*, "The RHIC design overview," *Nucl. Instrum. Meth.* **A499** (2003) 245–263.

[64] **STAR** Collaboration, R. Bellwied *et al.*, "The STAR silicon vertex tracker: A large area silicon drift detector," *Nucl. Instrum. Meth.* **A499** (2003) 640–651.

[65] L. Arnold *et al.*, "The STAR silicon strip detector (SSD)," *Nucl. Instrum. Meth.* **A499** (2003) 652–658, `physics/0211083`.

[66] M. Anderson *et al.*, "The STAR time projection chamber: A unique tool for studying high multiplicity events at RHIC," *Nucl. Instrum. Meth.* **A499** (2003) 659–678, `nucl-ex/0301015`.

[67] K. H. Ackermann *et al.*, "The forward time projection chamber (FTPC) in STAR," *Nucl. Instrum. Meth.* **A499** (2003) 713–719, `nucl-ex/0211014`.

[68] L.-j. Ruan, *Pion, kaon, proton and antiproton spectra in d + Au and p + p collisions at* $\sqrt{s_{NN}}$ *= 200-GeV at the Relativistic Heavy Ion Collider*. PhD thesis, USTC, 2005. `nucl-ex/0503018`.

[69] **STAR** Collaboration, M. Beddo *et al.*, "The STAR barrel electromagnetic calorimeter," *Nucl. Instrum. Meth.* **A499** (2003) 725–739.

[70] **STAR** Collaboration, C. E. Allgower *et al.*, "The STAR endcap electromagnetic calorimeter," *Nucl. Instrum. Meth.* **A499** (2003) 740–750.

[71] **STAR** Collaboration, F. Bergsma *et al.*, "The STAR detector magnet subsystem," *Nucl. Instrum. Meth.* **A499** (2003) 633–639.

[72] C. Adler *et al.*, "The RHIC zero degree calorimeters," *Nucl. Instrum. Meth.* **A470** (2001) 488–499, `nucl-ex/0008005`.

[73] **STAR** Collaboration, F. S. Bieser *et al.*, "The STAR trigger," *Nucl. Instrum. Meth.* **A499** (2003) 766–777.

[74] **STAR** Collaboration, K. H. Ackermann *et al.*, "STAR detector overview," *Nucl. Instrum. Meth.* **A499** (2003) 624–632.

[75] **STAR** Collaboration, C. Adler *et al.*, "The STAR level-3 trigger system," *Nucl. Instrum. Meth.* **A499** (2003) 778–791.

[76] D. Liko, "Track Fitting in the STAR Detector using the Kalman Filter Method," *STAR Note* **00087** (1992) 1–15.

[77] H. Bichsel, "A method to improve tracking and particle identification in TPCs and silicon detectors," *Nucl. Instrum. Meth.* **A562** (2006) 154–197.

[78] "Future Science at the Relativistic Heavy Ion Collider," (2006) `http://www.agsrhichome.bnl.gov/RHIC/Runs/`.

[79] E. Yamamoto, *Phi meson Production in Au+Au Collisions at the Relativistic Heavy Ion Collider*. PhD thesis, UCLA, 2001.

[80] D. L'Hote, "About Resonance signal extraction from multiparticle data: combinatorics and event mixing methods," *Nucl. Instrum. Meth.* **A337** (1994) 544–556.

[81] N. Borghini and J. Y. Ollitrault, "Azimuthally sensitive correlations in nucleus nucleus collisions," *Phys. Rev.* **C70** (2004) 064905, `nucl-th/0407041`.

[82] **STAR** Collaboration, C. Adler *et al.*, "Elliptic flow from two- and four-particle correlations in Au + Au collisions at $\sqrt{s_{NN}}$ = 130-GeV," *Phys. Rev.* **C66** (2002) 034904, `nucl-ex/0206001`.

[83] **STAR** Collaboration, J. Adams *et al.*, "K*(892) resonance production in Au + Au and p + p collisions at $\sqrt{s_{NN}}$ = 200-GeV at STAR," *Phys. Rev.* **C71** (2005) 064902, `nucl-ex/0412019`.

[84] **STAR** Collaboration, J. Adams *et al.*, "Identified particle distributions in p p and Au + Au collisions at $\sqrt{s_{NN}}$ = 200-GeV," *Phys. Rev. Lett.* **92** (2004) 112301, `nucl-ex/0310004`.

[85] **STAR** Collaboration, J. Adams *et al.*, "Measurements of transverse energy distributions in Au + Au collisions at s(NN)**(1/2) = 200-GeV," *Phys. Rev.* **C70** (2004) 054907, `nucl-ex/0407003`.

[86] **STAR** Collaboration, S. Salur, "System and energy dependence of strangeness production with STAR," *Nucl. Phys.* **A774** (2006) 657–660, `nucl-ex/0509036`.

[87] K. Redlich and A. Tounsi, "Strangeness enhancement and energy dependence in heavy ion collisions," *Eur. Phys. J.* **C24** (2002) 589–594, `hep-ph/0111261`.

[88] **STAR** Collaboration, B. I. Abelev, "Mass, quark-number, and $\sqrt{s_{NN}}$ dependence of the second and fourth flow harmonics in ultra-relativistic nucleus nucleus collisions," `nucl-ex/0701010`.

[89] Y. Lu *Private communication.*

[90] P. Sorensen *Private communication.*

[91] **PHOBOS** Collaboration, S. Manly *et al.*, "System size, energy and pseudorapidity dependence of directed and elliptic flow at RHIC," *Nucl. Phys.* **A774** (2006) 523–526, `nucl-ex/0510031`.

[92] S. A. Voloshin, "Toward the energy and the system size dependece of elliptic flow: working on flow fluctuations," `nucl-th/0606022`.

[93] P. Huovinen, "Anisotropy of flow and the order of phase transition in relativistic heavy ion collisions," *Nucl. Phys.* **A761** (2005) 296–312, `nucl-th/0505036`.

[94] R. C. Hwa and C. B. Yang, "Scaling behavior at high p(T) and the p/pi ratio," *Phys. Rev.* **C67** (2003) 034902, `nucl-th/0211010`.

[95] V. Greco, C. M. Ko, and P. Levai, "Parton coalescence and antiproton/pion anomaly at RHIC," *Phys. Rev. Lett.* **90** (2003) 202302, `nucl-th/0301093`.

[96] **STAR** Collaboration, J. Adams *et al.*, "nucl-ex/0606014," `nucl-ex/0606014`.

[97] M. Estienne, *Propriétés chimiques et dynamiques des collisions d'ions lourds aux énergies du RHIC par la mesure de la production des baryons doublement étranges dans l'expérience STAR.* PhD thesis, SUBATECH, 2005.

[98] L.-W. Chen and C. M. Ko, "Phi and Omega production from relativistic heavy ion collisions in a dynamical quark coalescence model," *Phys. Rev.* **C73** (2006) 044903, `nucl-th/0602025`.

[99] J. Gonzalez *Private communication.*

[100] Z.-W. Lin, C. M. Ko, B.-A. Li, B. Zhang, and S. Pal, "A multi-phase transport model for relativistic heavy ion collisions," *Phys. Rev.* **C72** (2005) 064901, `nucl-th/0411110`.

[101] X.-N. Wang and M. Gyulassy, "HIJING: A Monte Carlo model for multiple jet production in p p, p A and A A collisions," *Phys. Rev.* **D44** (1991) 3501–3516.

[102] B. Zhang, "ZPC 1.0.1: A parton cascade for ultrarelativistic heavy ion collisions," *Comput. Phys. Commun.* **109** (1998) 193–206, `nucl-th/9709009`.

[103] T. Sjostrand, "High-energy physics event generation with PYTHIA 5.7 and JETSET 7.4," *Comput. Phys. Commun.* **82** (1994) 74–90.

[104] B. Li, A. T. Sustich, B. Zhang, and C. M. Ko, "Studies of superdense hadronic matter in a relativistic transport model," *Int. J. Mod. Phys.* **E10** (2001) 267–352.

[105] R. C. Hwa and C. B. Yang, "Recombination of shower partons at high p(T) in heavy-ion collisions," *Phys. Rev.* **C70** (2004) 024905, `nucl-th/0401001`.

[106] **PHENIX** Collaboration, S. S. Adler *et al.*, "Production of Phi mesons at mid-rapidity in $\sqrt{s_{NN}}$ = 200-GeV Au + Au collisions at RHIC," *Phys. Rev.* **C72** (2005) 014903, `nucl-ex/0410012`.

[107] S. Pal, C. M. Ko, and Z.-w. Lin, "Phi meson production in relativistic heavy ion collisions," *Nucl. Phys.* **A707** (2002) 525–539, `nucl-th/0202086`.

[108] **PHENIX** Collaboration, A. Kozlov, "$\phi$ production as seen in $e^+e^-$ and $K^+K^-$ decay channels in Au+Au collisions by PHENIX at $\sqrt{s_{NN}}$=200 GeV," *Nucl. Phys.* **A774** (2006) 739–742.

[109] **STAR** Collaboration, J. Bielcikova, "Azimuthal and pseudo-rapidity correlations with strange particles at intermediate-$p_T$ at RHIC," (2007) `nucl-ex/0701047`.

[110] B. Müller, "Hadronic signals of deconfinement at RHIC," `nucl-th/0404015`.

[111] **STAR** Collaboration, K. Schweda, "A heavy-flavor tracker for STAR," *Nucl. Phys.* **A774** (2006) 907–910, `nucl-ex/0510003`.

# Acknowledgements

Thank you to Professor Jean Cleymans, Grazyna Odyniec and Hans Georg Ritter for the important and exciting opportunity to work on the STAR experiment and to spend time in the RNC Group at LBNL. It was a privilege to do research there.

Thank you to Nu Xu for your guidance and excitement about physics.

My thanks also go to the past and present members of the RNC group at LBL, "the tough crowd", with whom I had the good fortune to work, and my STAR collaborators for your valuable input, help and good discussions.

Thank you Marco and Paul for always having time to answer my questions and the patience to keep repeating the answers! Markus, I owe you many beers for proofreading.

Thank you to my family for your support and for always believing in me.

Mark, I couldn't have done this without you.